



UNIVERSITÀ DEGLI STUDI DI CATANIA
DIPARTIMENTO DI FISICA E ASTRONOMIA
XXX CICLO DI DOTTORATO

TOF-BASED DIAGNOSTICS SYSTEM DEVELOPMENT AND GEANT4
SIMULATION OF THE ELIMED TRANSPORT AND DOSIMETRY BEAM LINE
FOR HIGH ENERGY LASER-DRIVEN ION BEAM APPLICATIONS
@ ELI BEAMLINES

PHD THESIS

GIULIANA GIUSEPPINA MILLUZZO

PHD COORDINATOR

PROF. VINCENZO BELLINI

TUTOR

PROF. STEFANO ROMANO

SUPERVISORS

DOTT. FRANCESCO ROMANO

DOTT.SSA VALENTINA SCUDERI

To my family

To those who have always believed in me

To you

Abstract

The acceleration processes based on the coherent interaction of high-power laser with matter is by now one of the most interesting topics in the field of particle acceleration, becoming a real alternative to conventional approaches. Some of the peculiarities of laser-accelerated ion beams, if well controlled, are very promising for fundamental research as well as for multidisciplinary applications, including the medical field.

In this framework, a complete transport and dosimetry beam line, named ELIMED, has been realized at INFN-LNS and will be installed at ELI-Beamlines by the end of 2017. It will be a section of the user-oriented ELIMAIA (ELI Multidisciplinary Applications of laser-Ion Acceleration) beam line at ELI-Beamlines, dedicated to the high-energy ion acceleration as well as high-intense X-rays generation and their possible multidisciplinary applications.

The present thesis describes the Monte Carlo Geant4-based application, simulating the complete ELIMED beam line, in terms of geometry as well as magnetic and electric fields. Realistic top-to-bottom simulations have been performed to predict beam parameters and optimize dose distributions at the irradiation point in terms of homogeneity and dose delivered per shot in view of medical applications. In particular, the simulation performed clearly indicates the possibility to obtain a Spread Out Bragg Peak (SOBP) of clinical relevance with the selected proton beams. A specific on-line diagnostics system based on the Time Of Flight (TOF) technique coupled with diamond and/or silicon carbide detectors, has been developed and will be used for shot-to-shot energy distribution and flux measurement. Considering the high-energy laser-driven ion beams that will be delivered at ELIMAIA, a new analysis procedure, optimized for high-energy laser-driven proton beams, to extract the energy distribution for a given in species from the TOF signal has been developed and validated. The experiments carried out in the multi-TW laser facilities, Rutherford Appleton Laboratory (RAL, UK), Ludwig Maximilians Universitat Munchen (LMU, GE) and the Prague Asterix Laser System (PALS,CZ), will be described in details

together with the results achieved using the TOF method for beam diagnostics. The results confirmed the reliability of the TOF technique and of the procedure developed for high-energy laser-driven ion beams, pointing out that TOF technique can be particularly suitable for the on-line diagnosis of the high-energy ion beam characteristics, giving real time information useful to optimize transport as well as to investigate specific nuclear reactions occurring in the laser-target interaction.

Contents

Abstract	2
Introduction	5
1 High power laser-matter interaction and state of the art	9
1.1 Plasma physics: Debye length and plasma frequency	11
1.2 Laser-plasma interaction	13
1.2.1 Ponderomotive force	15
1.2.2 Laser interaction with solid target and laser absorption mechanisms	16
1.3 Particle acceleration regimes	17
1.3.1 The Target Normal Sheath Acceleration (TNSA) regime	17
1.3.2 Scaling law for laser-driven proton beams	19
1.3.3 Radiation Pressure Acceleration regime	21
1.4 Power lasers: state of the art, perspectives and possible applications	23
2 The ELIMAIA transport,diagnostics and dosimetry beam line at ELI	
Beamlines	28
2.1 The Extreme Light Infrastructure (ELI)	28
2.1.1 ELI Beamlines facility	31
2.2 ELIMAIA beam line	32
2.2.1 The ELIMED section	33
2.2.2 Ion beam collection and focusing system	36

2.2.3	Diagnostics system	38
2.2.4	In vacuum ion beam energy selection	39
2.2.5	Dosimetry and sample irradiation system	43
3	Geant4 simulation of the ELIMED beam line	49
3.1	Monte Carlo method and Geant4 simulation toolkit	49
3.1.1	The Geant4 toolkit	50
3.2	The ELIMED Geant4 application	52
3.2.1	Source implementation	54
3.2.2	Geometry components	57
3.3	Top-to-bottom simulations	68
3.3.1	In vacuum transport and energy selection	68
3.3.2	Dose delivery: transversal and longitudinal beam profile	75
3.3.3	Optimization in air of the transversal 60 MeV proton beam profile	79
3.4	Energy modulation with the ESS for longitudinal dose distribution of clinical interest	85
4	The TOF based diagnostics system for the ELIMAIA beam line	92
4.1	Diagnostics of high-energy laser-driven ion beams: state of the arts and solutions for ELIMAIA	92
4.2	Diamond detectors for ELIMAIA beam line	96
4.3	Time Of Flight method: new approach with high-energy laser-driven ion beams	103
4.3.1	Time distribution reconstruction: deconvolution procedure	106
4.3.2	New procedure for high-energy proton spectrum reconstruction	108
5	Experimental campaigns with TOF-based diagnostics	116
5.1	TOF analysis procedure validation with high energy laser-driven ion beams	116
5.1.1	Experimental Setup	116

5.1.2	Analysis procedure and results of TOF signals acquired in backward direction	119
5.1.3	Analysis and results of TOF signals acquired in forward direction .	138
5.2	Test with laser-driven proton beams along a compact transport beam line .	142
5.2.1	Results	144
5.3	TOF diagnostics for laser-induced aneutronic fusion reaction studies	151
5.3.1	Experimental setup	153
5.3.2	Methods	156
5.3.3	Results	158
	Conclusions and future perspectives	164
	Bibliography	168

Introduction

Over the last decades, the scientific interest towards innovative particle acceleration techniques, alternative to conventional ones, has led to a growing effort in the study of laser-plasma interaction [1]. In particular, one of the most attractive topics in plasma-based particle acceleration, is the generation of high-intensity, high-pulsed gammas and charged particles, such as electrons, protons and ions, from the interaction of high power, ultra-short laser pulses with solid matter [2, 3]. Contrary to the conventional particle acceleration techniques, based on the use of huge and expensive machines such as cyclotrons or synchrotrons, the laser-matter acceleration technique is mainly based on the innovative concept, introduced by Veksler in 1957, of *coherent acceleration*, according to which the accelerating field on each particle is proportional to the number of particles being accelerated [2].

The large quantity of energy transferred from laser to the solid surface in laser-matter interaction, causes the creation of a plasma state: a strong electric field is generated from the displacement of a great amount of hot electrons, leading to the acceleration of Multi-MeV protons and ions on the rear or on the front side of the target [4].

Many experimental evidences [5, 6, 7] as well as theoretical arguments have confirmed the possibility to accelerate Multi-MeV proton beams (up to 70 MeV [8]) through the interaction of high intensity laser (from 10^{18} to 10^{20} W/cm²) on thin solid target. In particular, according to the laser specifications, such as energy, pulse time duration, power, and to target thickness, different acceleration regimes may occur: the Target Normal Sheath Acceleration (TNSA) [9, 10] regime, being the most experimentally and theoretically in-

investigated mechanism so far, which dominates for a laser intensity $< 10^{22}$ W/cm² and the Radiation Pressure Acceleration (RPA) regime which dominates at higher laser intensities leading to multi-GeV ion acceleration [11].

The peculiarities of such high-pulsed laser-accelerated beams, such as high fluxes per shot (up to 10^{12} p/bunch), extremely high dose-rate (order of 10^9 Gy/min [12]), broad energy spectrum and large divergence [13], if well controlled, are very attractive in fundamental nuclear as well as in the applied physics, as for instance in the medical one. In particular, the use of laser-matter interaction as a source of high-energy particle beams for medical applications could provide a promising alternative tool for dose delivery during radiobiological irradiation as well as, in a future perspective, clinical treatments with protons and ions (hadrontherapy) [14, 15]. The growing interest towards possible applications of laser-accelerated ion beams, has led to the establishment of several international collaborations among research centers [16, 17, 18, 19, 20] aiming to demonstrate the feasibility of laser-accelerated ion beam application in multidisciplinary fields. In this framework, a collaboration between the INFN-LNS (National Institute for Nuclear Physics – Laboratori Nazionali del Sud, Catania, Italy) and the ASCR-FZU (Institute of Physics of the Czech Academy of Science), in charge for the user ELI Beamlines facility realization, has been established in 2011 [20]. In 2014, a three-years contract has been signed between the two Institutions for the development and realization at INFN-LNS of a transport and dosimetry beam line, called ELIMED. It has been specifically designed for high-energy laser-accelerated ion beams (up to 60 MeV/u) and will be installed by the end of 2017 at ELI Beamlines (Prague, Czech Republic) [21]. In particular, the ELIMED beam line, will be a section of the user-oriented ELIMAIA (ELI Multidisciplinary Applications of laser-Ion Acceleration) beam line, sited in one of the experimental halls at ELI Beamlines and dedicated to the high-energy ion acceleration as well as high-intense X-rays generation and their possible applications. The ELIMED section, dedicated to the beam transport and dose delivery, will allow transporting laser-driven ion beams up to an energy of 60 MeV/n, delivering controlled, focused and selected in energy beams, suitable for multidis-

ciplinary applications [22]. The present thesis has been carried out in the framework of the ELIMED beam line development and realization at INFN-LNS.

The thesis work is mainly focused on two fundamental aspects regarding the realization:

- Predicting beam characteristics along the beam line, in terms of particle flux, energy, angular distribution and dose delivered per shot downstream the beam line. This purpose has been fulfilled by developing a Monte Carlo Geant4 simulation [23, 24, 25] of the whole ELIMED beam line: each element composing the transport beam line, as well as the dosimetric devices, has been simulated, implementing the complete geometrical components as well as the magnetic or electric parameters, to provide top-to-bottom simulation and demonstrate the possibility of using the transported laser-driven particle beams for applications [26, 27]. A complete Geant4 application has been developed and it will be available for future ELIMAIA's users interested in the simulation of their specific experimental setups.
- Measurement of the particle energy spectrum and flux of the accelerated particles along the ELIMED beam line. Beam diagnostics has indeed a twofold purpose: optimize the beam transport and deliver a stable beam at the end of the beam line. In order to fulfill this purpose a real-time diagnostics system, based on diamond and silicon carbide detector using the Time Of Flight (TOF) technique, has been developed [31, 32]. The TOF technique has been, indeed, widely used as beam diagnostics method in low-energy laser-accelerated beam experiments, being one of the most diffused diagnostics method in this field [28, 29, 30]. Nevertheless, the high-energy ion beams expected at ELIMAIA requires a more thorough investigation on the signal treatment in order to reconstruct the energy spectrum from the high-energy ion TOF signals [33]. A complete analysis procedure, enabling to convert TOF signals, generated from high-energy laser-driven beams, in energy spectrum for specific ion species, has been developed and successfully tested in several experimental campaigns with Multi-TW and PW laser systems.

The main goal of both topics discussed above is to demonstrate the capability of the ELIMED beam line to provide reproducible and monitored optically accelerated ion beams suitable for multidisciplinary applications.

This thesis is organized in 5 chapters:

- Chapter 1 contains the description of high power laser-plasma, laser-matter interaction and particle acceleration mechanisms. A survey of the state of the art laser characteristics all over the world in terms of energy, pulse duration and maximum proton energy reached is also given.
- Chapter 2 describes the ELI-Beamline user facility, in particular the ELIMAIA beam line. A description of the ELIMED beam line, realized at INFN-LNS in Catania, including the details on transport and dosimetry elements, is also provided.
- Chapter 3 describes the developed Geant4-based Monte Carlo code reproducing the ELIMED beam line. Validation of the magnetic and electric elements, by comparing the Geant4 results with other reference analytic codes, such as SIMION [34] and COMSOL [35], are reported. Simulations from the source down to the irradiation point are also shown, for 5 MeV and 60 MeV proton energy selection, which respectively represent the minimum and maximum transported energy. Optimization of the transversal profile for the 60 MeV proton case, in terms of beam homogeneity, crucial for applications, will be shown. Furthermore, the possibility to optimize the simulated transport element configurations in order to obtain an active modulation of the beam and deliver longitudinal flat dose distributions of clinical relevance is also discussed. Preliminary investigation results will be also presented.
- Chapter 4 describes the ELIMED beam line TOF based diagnostics. Detectors, time response and energy resolution achievable will be discussed. The TOF analysis procedure, developed and optimized for high energy laser-driven proton beams, will be described in details.

- Chapter 5 describes three experimental campaigns carried out with TOF detectors in three laser facilities. In particular, an experiment carried out with diamond detectors with the Petawatt VULCAN laser system at RAL laser facility (UK), where protons up to about 60 MeV are typically accelerated [36], will be presented. The main purpose of the experiment was to validate the developed TOF procedure by comparing the results with other well-established diagnostics such as Thomson Parabola, Radiochromic films and CR-39s.

The second experiment was performed with the table-top, and high repetition rate (\sim Hz) ATLAS laser system at Ludwig Maximilians Universitat Munchen (LMU) [37] in Munich, along a compact beam line, consisting of focusing magnet and a selection system optimized for laser-driven proton beam transport of energy up to about 10 MeV. Considering the forthcoming ELIMAIA beam line implementation, the main aim of this test was to demonstrate that TOF diagnostics using diamond detectors represents a powerful tool for real-time measurement of the time evolution distribution as well as energy spectrum.

The third experiment, accepted and funded by LASERLAB, investigates a particular nuclear reaction occurring between protons and boron ions, producing MeV α particles [38, 39, 40, 41]. The experiment has been performed using the pico-second Asterix laser system at PALS (Prague Asterix Laser System) (CZ). The main diagnostics system consists in an array of diamond and SiC detectors, surrounding the target, in order to measure proton and alpha particle yield and angular distribution. This particular detector array setup allowed to test the possibility to use TOF detectors not only for online beam diagnostics but also as powerful detection system for several applications including nuclear reaction induced with laser-driven ion beam, giving the possibility to measure on line not only yield and energy spectrum but also angular distribution in a wide solid angle coverage.

Chapter 1

High power laser-matter interaction and state of the art

New approach studies on particle acceleration field have led to develop alternative acceleration mechanisms based on the interaction of high-pulsed power laser with solid target. More than half a century ago, Veksler (1957) introduced the concept of *coherent acceleration* of particles as a mechanism in which the accelerating field on each particle is proportional to the number of particles being accelerated, in contrast with conventional acceleration techniques [2]. This represents the starting point for the study of laser-matter interaction and particle acceleration mechanisms, both from the theoretical and experimental point of view.

The interaction process is mainly based on the impact of high power laser which, transferring its energy on solid target surface, generates a state of quasi-neutral plasma and a high electric field, responsible for the particle acceleration. The light charged particles, i.e. electrons, are pushed on the rear side of the target followed by positive charged particles, i.e. protons and ions, affected by Coulombian attractive force exerted by the electrons. According to the specific characteristics of laser, as energy on target, time duration, power and characteristic frequency, different particle acceleration regimes can occur. They will be presented in details in section 1.3.

Before the 2000s, ions having energies up to several MeV had been observed in several high-

intensity laser-matter interaction experiments and for different targets, including thick solid foils ([42, 43, 44]), gas jets ([49, 50]) and submicrometric clusters ([51]). Nevertheless, the rather isotropic ion emission as well as the low brilliance, make these configurations unattractive as ion accelerators for any kind of applications. On the other hand, in 2000, three independent experiments, (Clark et al.[5], Maksimchuk et al.[6]; Snavely et al.[7]), have been performed, observing for the first time high-intensity and rather collimated laser-driven proton beams accelerated from high-intensity high-pulsed laser interaction with metallic or plastic target of the order of several micron thickness. Details of laser intensity, number of protons and maximum proton energy for each experiment are listed in table 1.1.

Experiment	Laser intensity [W/cm ²]	Number of protons	Max. proton energy
Clark et al.	$5 \cdot 10^{19}$	10^{12}	18 MeV
Maksimchuk et al.	$3 \cdot 10^{18}$	$>10^9$	1.5 MeV
Snavely et al.	$3 \cdot 10^{20}$	$2 \cdot 10^{13}$	58 MeV

Table 1.1: Details of the experiments carried out in the *annus mirabilis* of laser-driven ion acceleration (2000) [2]

All three experiments observed rather collimated protons along the target normal direction on the rear side of target, i.e. opposite to the laser irradiated surface. Hydrogen is in fact present on the metallic structure of the target as contaminant: thin layer of water and/or hydrocarbon are usually deposited on the target surface. Moreover, other experiments [42, 44, 5], performed with nanosecond as well as with sub-picosecond high-intensity lasers, have shown a higher acceleration of protons and heavy ions in backward direction, i.e. on the front surface of the target, characterized by a wide energy and angular distribution.

The impressive results of particle acceleration in forward direction, together with the possibility to have multiple particle species, such as gammas, electrons, protons and different kind of ions in one shot, generated an enormous interest of scientific community towards

the possibility of using them for several applications, including the medical ones. As it is well known, charged particles, as protons and ions, thanks to the localized energy deposition in matter, contrary to broad energy deposition of x-rays and gammas, show interesting and important advantages for cancer therapy with respect to the traditional radiotherapy. These advantages led to the development of the *protontherapy* and *ion therapy* which respectively use protons and heavy ions for tumor treatment [45, 46, 47]. Ions are typically accelerated from rather huge and expensive cyclotrons or synchrotrons and the complexity of the accelerating machines, as well as of the transport elements to deliver the beam to the patient, often limit spreading worldwide hadrontherapy. This has recently pushed to consider alternative acceleration techniques, among which the one based on laser-matter interaction [48] seems to be very promising. In this framework, several laser facilities have been built, having as main purpose the investigation of laser-matter interaction for fundamental physics as well as for applications, i.e. medical physics. An overview of the existing laser facilities wide world will be presented.

1.1 Plasma physics: Debye length and plasma frequency

Solids are usually characterized by stable atomic structures, organized in crystalline solid lattices. If the thermal conditions of the system are altered with respect to the equilibrium state, i.e. increasing temperature and exceeding atom and molecules binding energy, the regular solid structure decomposes: molecules and atoms split into their constituents. In particular, if the temperature is so high to exceed the ionization energy of atoms, a state of quasi-free positive charges (ions +) and negative charges (electrons) will be generated [52]. The totality of positive and negative charges is called *plasma* and it can be interpreted like a fourth state of matter, which shows different interaction mechanisms between the charges. From this state and the related interactions originates the so-called laser-driven beams. Plasma characteristics can be described using the two following parameters:

- Debye length.

In a quasi-neutrality condition, in which electron density and temperature are equal to ion density and temperature [53], if a test charged particle, q_t , is inserted in the plasma structure, a perturbation occurs provoking a reorganization of spatial charge distribution. Indeed, particles with opposite sign with respect to the test particle, will be attracted whereas particles with opposite sign will be repelled. This effect causes a variation of electrostatic potential Φ which can be expressed by the superposition of the test particle's own potential and the potential of the plasma particles that have moved slightly in response to the test particle. If the test particle has positive charge, the electrons will be attracted by it forming a negative charged cloud around q_T , that will act as screening of the charge q_T . This effect is called *electronic screening* and will partially cancel (i.e., shield or screen) the test particle potential. The *screening* can be calculated by *Poisson* equation [52]:

$$\nabla^2\Phi = -\frac{1}{\epsilon_0}[q_T\delta(\mathbf{r}) + \sum_{\sigma} n_{\sigma}(\mathbf{r})q_{\sigma}] \quad (1.1)$$

where $q_T\delta(r)$ is the test particle charge density, the term $\sum_{\sigma} n_{\sigma}(r)q_{\sigma}$ is the charge density of all plasma particles which generates the *screening*, with σ indicating each involved species and n_{σ} the corresponding density. If the perturbation due to the insert of the test particle is very slow, the density n_{σ} of the species in the plasma can be expressed by the *Boltzmann relation*:

$$n_{\sigma} = n_{\sigma 0} \exp(-q_{\sigma}\Phi/k_B T_{\sigma}) \quad (1.2)$$

where $n_{\sigma 0}$ is a constant, k_B is the Boltzmann constant and T_{σ} the single species temperature. Moreover, considering that the perturbation introduced by a single test particle is infinitesimal, it can be safely assumed $|q_{\sigma}\Phi| \ll k_B T_{\sigma}$ and the expression 1.2 becomes simply $n_{\sigma} \sim n_{\sigma 0}(1 - q_{\sigma}\Phi/k_B T_{\sigma})$. Thanks to the assumed initial quasi-neutrality condition, i.e. $\sum_{\sigma=i,e} n_{\sigma 0}(r)q_{\sigma} = 0$, the expression 1.1 can be reduced in:

$$\nabla^2\Phi - \frac{1}{\Lambda_D^2}\Phi = -\frac{q_T}{\epsilon_0}\delta(r) \quad (1.3)$$

where Λ_D is defined as the *total Debye length*:

$$\frac{1}{\Lambda_D^2} = \sum_{\sigma} \frac{1}{\lambda_{\sigma}^2} \quad \lambda_{\sigma}^2 = \frac{\epsilon K_B T_{\sigma}}{n_{\sigma 0} q_{\sigma}^2} \quad (1.4)$$

Solving equation 1.3, the expression of the electrostatic potential modified by screening effect can be expressed by [52]:

$$\Phi(r) = \frac{q_T}{4\pi\epsilon_0 r} e^{-r/\lambda_D} \quad (1.5)$$

In equation 1.5, for $r \ll \lambda_D$, the potential becomes the typical electrostatic potential of a point-like test particle, instead for $r \gg \lambda_D$ the test particle is completely screened by the surrounding charges and the potential goes to zero very quickly.

Then, the *Debye length* λ_D represents the radius of negative charged cloud around q_T and then the effective range of the electrostatic potential Φ . In order for shielding to be a relevant issue, for $r \gg \lambda_D$, the Debye length must be small with respect to the overall plasma dimension.

- Plasma frequency.

It arises from the coupling of positive and negative charges, which tend to neutralize each others because of the Coulombian force. In this context, the interaction between negative and positive charges can be conceived as an *oscillation* around an equilibrium point, as result of a spatial separation. The plasma, and hence the charges, oscillates with a typical frequency ω_p [53]:

$$\omega_p = \frac{ne^2}{\epsilon_0 m} \quad (1.6)$$

The oscillation frequency is connected to the plasma period τ_p ($\tau_p = 1/\omega_p$), which stands for the minimum elapsed time in order to observe plasma oscillations. Note that plasma oscillations will only be observed if the plasma system is studied over time periods τ longer than the plasma period τ_p , and if external actions change the system at a rate no faster than ω_p . Likewise, observations over length-scales L

shorter than the distance $v_t\tau_p$ traveled by a typical plasma particle during a plasma period will also not detect plasma behaviour. This distance, which is the spatial equivalent to τ_p is the already described Debye length λ_D , connected to the plasma frequency through:

$$\lambda_D^2 = \frac{k_B T}{m\omega_p^2} = \frac{k_B T}{m} \tau_p^2 \quad (1.7)$$

where m and T are respectively the mass and the temperature of the species considered.

As it is clear, the studied system can be definitively considered to be a plasma provided that:

$$\lambda_D/L \ll 1 \quad \text{and} \quad \tau_p/\tau \ll 1 \quad (1.8)$$

where, τ and L represent the typical time-scale and length-scale of the process under investigation.

1.2 Laser-plasma interaction

High-power lasers when focused on matter lead to extremely rapid ionization by direct phot-offect or, depending on wavelength and material, by multiphoton processes. The target ionization occurs in fact if the laser intensity is sufficient to overcome the binding energy of a given electron to its atom. As a consequence, a laser radiation with intensities, ranging from 10^{10} W/cm² to approximately 10^{23} W/cm², can deliver energy to a target over times from nanoseconds down to few femtoseconds [54, 55] generating an electric field much stronger than the Coulomb field which is responsible for binding electrons and atomic nuclei. Therefore, depending on both laser and target parameters, rapid ionization occurs near the target surface and matter is transformed in a dense plasma. Nevertheless, nowadays high power lasers operate in the near infrared domain and a direct interaction of the laser beam with matter is possible only under certain conditions depending on the

definition of the so-called *critical density* [2] for laser density:

$$n_c = \frac{m_e \omega_L^2}{4\pi} = 1.1 \cdot 10^{21} \text{ cm}^{-3} \left(\frac{\lambda}{\mu\text{m}} \right)^{-2} \quad (1.9)$$

where ω_L and λ are respectively the frequency and the wavelength of the laser. Different behaviors occur according to the value of n_c in relation with the electron plasma density n_e , which, as explained in expression 1.6, depends on the plasma frequency.

Since the linear refractive index of the plasma, from which depends the propagation of the wave within the plasma, is defined by:

$$\eta = \left(1 - \frac{\omega_p^2}{\omega_L^2} \right)^{1/2} = \left(1 - \frac{n_e}{n_c} \right)^{1/2} \quad (1.10)$$

three different situations can occur [2, 54]:

- $n_e < n_c$: underdense plasma. The refractive index has real values and the laser interacts with the plasma, propagating through it.
- $n_c = n_e$: critical condition. This condition is equivalent to $\omega_p = \omega_L$ and at the boundary between so-called underdense (the waves can propagate) and overdense (waves cannot propagate) plasma. It corresponds to the condition in which the wave is completely reflected from the plasma.
- $n_e > n_c$: overdense plasma. The refractive index has imaginary values, thus the wave is exponentially dumped and it vanishes and no interaction occurs with the plasma.

As it is clear, all the laser-plasma interactions occur either in the *underdense* region or for $n_c \sim n_e$. Relativistic effects make the refractive index nonlinear and the propagation of the plane wave with vector potential $\mathbf{A}=\mathbf{A}(\mathbf{x},\mathbf{t})$ is described from linear expression replacing the electron mass with the quantity $m_e\gamma$, where γ is the relativistic factor expressed by [2]

$$\gamma = \sqrt{1 + \langle a \rangle^2} = \sqrt{1 + a_0^2/2} \quad (1.11)$$

where $a = \frac{eA}{m_e c^2}$, and the angular brackets denote an average over the oscillation period. The parameter a_0 is the commonly used *dimensionless* amplitude related to the laser intensity I by:

$$a_0 = 0.85 \left(\frac{I \lambda^2}{10^{18} \text{W cm}^{-2}} \right)^{1/2} \quad (1.12)$$

The relativistic effect shows an increase of the critical density, known as the self-induced transparency. However, laser interaction and propagation through the plasma is not trivial and can be described via the ponderomotive effect which will be described in next section ([56, 57, 58]).

1.2.1 Ponderomotive force

The ponderomotive force plays a central role in ion acceleration generated by the laser interaction with the matter. Such peculiar force is non-linear and concerns the electric field created by the electromagnetic wave propagation inside the plasma. Indeed, the high intense and short laser pulse creates radial and longitudinal field gradients causing the electron ejection from the regions where the field is higher.

In a non-relativistic case, a charged particle q inside the electromagnetic field of the laser pulse, feels the *Lorentz force* which can be expressed by:

$$F = q[\mathbf{E}(r, t) + v \times \mathbf{B}(r, t)] \quad (1.13)$$

where $\mathbf{E}(r, t)$ is the electric field and $\mathbf{B}(r, t)$, the magnetic field.

Using the Maxwell equation, which connects them to each others, $\nabla \times E = -\frac{\partial B}{\partial t}$, and expressing the electric field as $E(r, t) = \hat{E}(r, t)e^{i\omega t}$, the magnetic field can be described by:

$$\mathbf{B}(\mathbf{r}, t) = \frac{i}{\omega} \nabla \times E(r, t) \quad (1.14)$$

where ω is the laser frequency. The derivation of the ponderomotive force relies on the possibility to separate the relevant time scales: the fast motion on the time scale of the laser period $2\pi/\omega$ and a secular one due to the ponderomotive force.

In lowest order, the particles just oscillate around its current position r_0 due to the electric field and the motion equation can be expressed by [4]:

$$m\ddot{r}_1 = q\hat{E}(r_0)e^{i\omega t} \quad (1.15)$$

The corresponding position and velocity are respectively:

$$r_1 = -\frac{q}{m\omega^2}\hat{E}(r_0)e^i, \quad \dot{r}_1 = -\frac{iq}{m\omega}\hat{E}(r_0)e^i \quad (1.16)$$

In the next higher order:

$$m\ddot{r}_2 = q[(r_1 \cdot \nabla)E(r_0, t) + \dot{r}_1 \times B(r_0, t)] \quad (1.17)$$

where the electric field has been expanded around r_0 . Now the calculation becomes nonlinear and also the imaginary part has to be taken into account. The details of the mathematical demonstration can be found in [4]. Considering this, the ponderomotive force can be expressed by:

$$F_p = m\ddot{r}_2 = -\frac{q^2}{4m\omega^2}\nabla|\hat{E}(r, t)|^2 \quad (1.18)$$

where in $\hat{E}(r)$ the position r is now referred to the so-called *oscillation center*. The force is independent from the sign of the charged particles, it is always repulsive, meaning that all charged particles are expelled from the region with high laser intensity. On the other hand, the ponderomotive force depends on the mass m present on the denominator of expression 1.18 and results much higher for electrons than for ions. Moreover, the ponderomotive is inverse proportional to the square of laser frequency, meaning that it increases with increasing the laser wavelength. When ultra-short laser pulse begins to propagate in a underdense plasma, the ponderomotive force, pushes electrons while ions remain nearly unperturbed because of their heavier mass, creating a longitudinal charge separation that, in turn, results in a longitudinal electric field able to pull back the electrons again. This perturbation induces a plasma wave that travels in the field at the group velocity of the pulse itself.

1.2.2 Laser interaction with solid target and laser absorption mechanisms

The interaction of high power laser with a solid target is radically different with respect to laser-plasma interaction, occurring only in underdense plasma condition ($n_e \leq n_c$). When laser hits a solid target, the electromagnetic wave promptly ionizes the target forming an overdense plasma with $n_e > n_c$. In such case, the laser pulse can then only propagate in the surface layer of the target, whose the thickness depends on the ratio n_e/n_c and the laser wavelength [54, 55]. Due to the the overdense plasma creation, the laser pulse cannot penetrate within the plasma and releases all the energy mostly to energetic electrons present on the target surface. In turn, the hot electrons are able to transport the absorbed energy into high density regions. There are many absorption mechanisms depending on a laser intensity and incidence angle, laser wavelength and its polarization, laser pulse shape, duration and contrast. The main absorption mechanisms are:

- *Inverse bremsstrahlung.* From a classical viewpoint, the electron oscillates in the electric field generated from laser electromagnetic wave and during the possible collision with the ions composing the plasma, it is knocked out of phase with the electric field. As a consequence the oscillatory energy of the electron is converted to random thermal energy. From a quantum viewpoint, the electron can gain energy only in units of $h\omega$, where ω is the frequency of the laser radiation.
- *Resonance absorption.* It is one of the dominant collisionless absorption mechanisms. It occurs when p-polarized laser pulse strikes the target and the electromagnetic field excites a large amplitude plasma wave, which is then damped, transferring energy to the plasma. In particular, for $\omega_L = \omega_P$, corresponding to the critical density at critical surface the electromagnetic frequency resonantly excites a plasma wave, which then transfers energy to the plasma.

Ones hitting pulse transfers the energy to hot electrons on the surface, they become relativistic and the energy can be expressed using the parameter a_0 described in 1.12 [2]:

$$\epsilon = m_e c^2 (\gamma - 1) = m_e c^2 (\sqrt{1 + a_0^2/2} - 1) \quad (1.19)$$

ϵ is also called *ponderomotive energy* [59], underlining that hot electrons drive proton and heavy ion acceleration, as observed in many experiments [9].

1.3 Particle acceleration regimes

Depending on laser intensity, target thickness and material, different particle acceleration mechanisms may occur in laser interaction with solid target, leading to obtain laser-driven particle beam with peculiar features described with different theoretical models. In this paragraph a short overview of the main acceleration regimes, most studied and investigated, will be given.

1.3.1 The Target Normal Sheath Acceleration (TNSA) regime

As mentioned before, during laser-matter interaction, hot electrons are created on the front side of target and eventually are able to reach the rear side of the target. The ones able to escape from the rear side in vacuum, due to charge unbalance, generate a sheath electric field E_s , normal to the rear surface. Since E_s must backhold electrons with a typical temperature T_h , the typical spatial extension of the sheath L_s is related to E_s by:

$$eE_s \sim \frac{T_h}{L_s} \quad (1.20)$$

where L_s is the Debye length of hot electrons. The sheath electric field, caused by hot electrons escaping from rear side of target, is responsible for the positive-negative charge separation in target and for particle acceleration. A cloud of relativistic electrons extends out of the target rear side for several Debye lengths originating an extremely intense electric field, which attracts positive charges, protons and heavy ions, resulting in an acceleration perpendicular to the target surface. The process is illustrated in Fig.1.1.

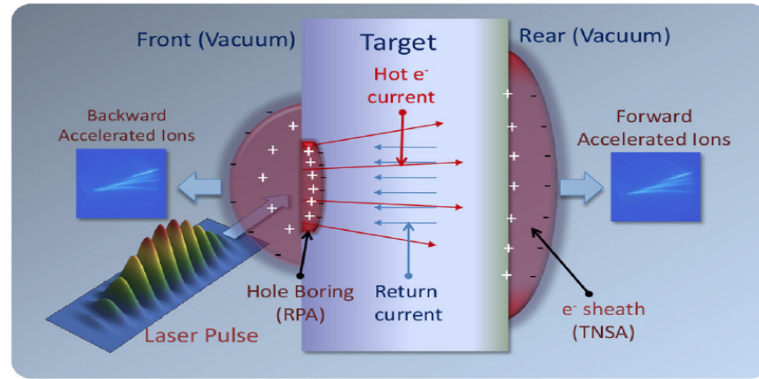


Figure 1.1: Scheme of some possible acceleration mechanisms in the laser interaction with thick solid target, including the TNSA regime.

This process, which dominates for laser intensity up to 10^{20} W/cm², is the so-called *Target Normal Sheath Acceleration* (TNSA) and is the most studied and investigated particle acceleration mechanisms, from both theoretical [60] as well as experimental point of view [13], due to the available laser systems, so far. It is particularly efficient for proton acceleration, always present as contaminant in solid target, and resulting strongly dependent on plasma scale length [70], on target composition and thickness as discussed in [62]. Several experiments [10, 68, 67] have investigated laser-accelerated beam properties typical of this regime. Since the particles are accelerated from different target depths, they can reach different maximum energies, leading to the generation of a wide range energy spectrum with a cut-off energy given by the driving electron temperature. As a consequence, typical proton energy spectrum in TNSA regime is characterized by a decreasing exponential energy distribution with a sharp cut-off at a maximum energy which scales with the laser parameters (figure 1.2 left). A broad angular distribution is also observed, being dependent on particle energy. The opening angle of the protons increases as the proton energy decreases, following the so-called *cone* angular structure as it is shown in the scheme in the right side of figure 1.2.

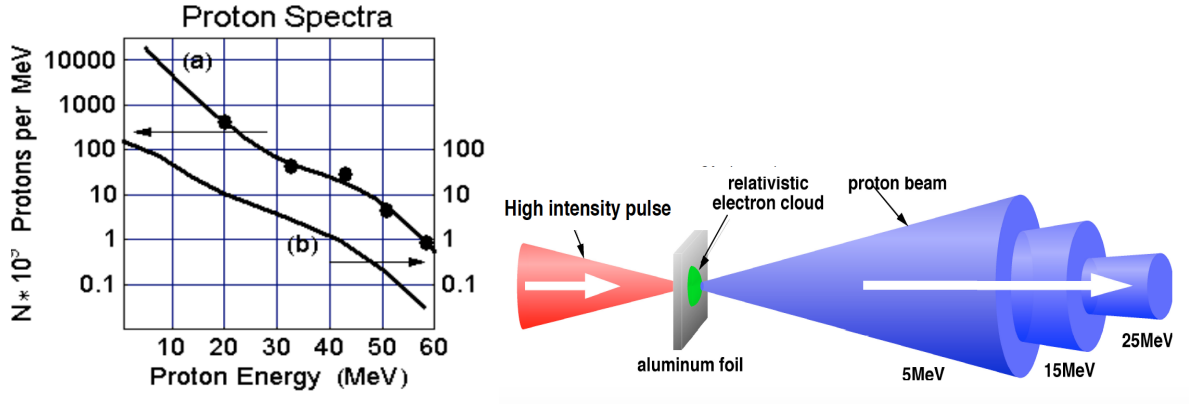


Figure 1.2: Left: Proton energy spectrum from the rear side of a $100 \mu\text{m}$ solid target irradiated by a 423 J, 0.5 ps pulse at normal incidence as reported in [7]. Right: Angular divergence related with particle energy for a typical laser-driven beam [65].

To summarize, the main features of laser-driven proton beams accelerated in TNSA regime are listed in table 1.2:

Properties	
Extreme laminarity:	Emittance $< 0.001 \pi$ mm-mrad
Short pulse duration:	\sim ps
High brightness:	$10^{11} - 10^{13}$ protons/bunch
High current:	kA range
Broad exponential energy spectrum	
High energy-dependent divergency	

Table 1.2: Laser-driven proton beam features in TNSA regime.

1.3.2 Scaling law for laser-driven proton beams

A great effort has been addressed to the study of the proper correlation between the maximum energy value and the laser and target parameters. It is, in fact, common to express the maximum proton energy E_{max} as a function of these parameters, and several experiments have investigated such a correlation to provide sufficiently reliable scaling laws, which may give directions for further developments.

Figure 1.3 [67] shows a collection of experimental data of E_{max} considering different pulse duration (left) and as a function of target thickness and composition (right).

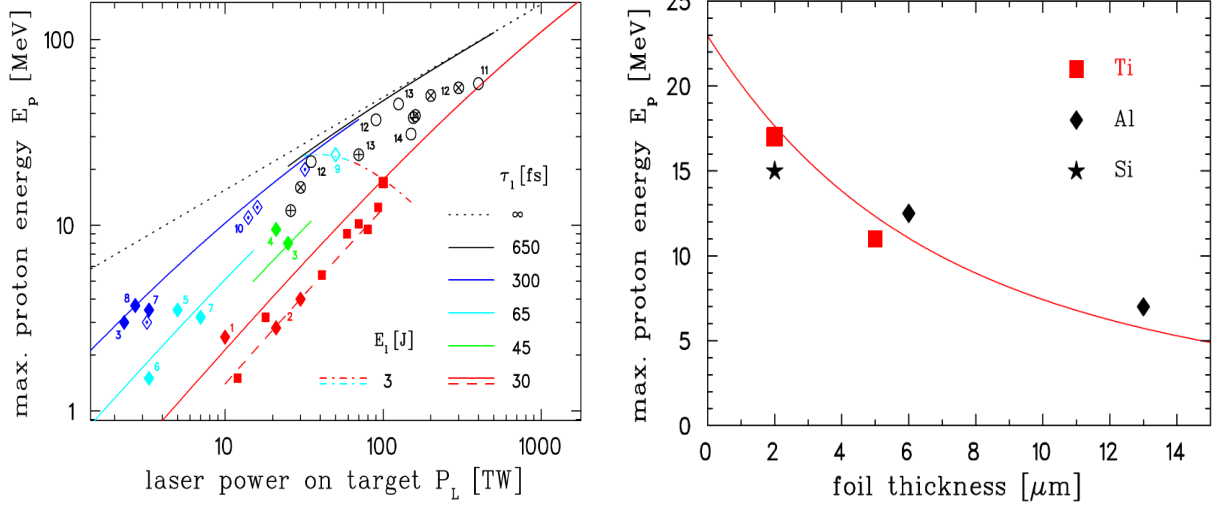


Figure 1.3: (Left). Scaling of the maximum proton energy with laser power. Full red squares represent experimental results obtained with 150 TW Draco laser at the research center Dresden–Rossendorf by varying the laser energy between 0.3 and 3 J. Full diamonds stand for experiments performed with Ti:sapphire lasers at about 1 J energy, open diamonds represents 5 J experiment at Janusp [70] and dotted diamonds show the results of an energy scan up to 10 J on target at LULI [68]. The color code of the experimental points corresponds to the different pulse duration regimes given in the legend. (Right). Maximum proton energy as a function of the thickness for a given target material and 100 TW power laser [67].

As it can be observed from figure 1.3, the maximum achievable proton energy strongly depends on laser pulse duration, laser energy on target and their ratio, i.e. the laser power. A scaling-law can be extracted from figure 1.3, using different theoretical approaches. In [67], the E_{max} dependence from laser characteristics is described assuming that a relativistic laser pulse of pulse duration τ_l accelerates N_e electrons from the target front side to an average energy E_e . The total number of electrons is determined by the efficiency η of the conversion of laser energy E_l into electron energy $N_e E_e = E_l \eta$. Integrating the equation

of motion up to the laser pulse duration, E_{max} can be expressed by the following relation:

$$\begin{aligned}
 E_{max} &= E_{\infty} \tanh^2\left(\frac{\tau_l}{2\tau_0}\right) \\
 E_{\infty}\left(\frac{\tau_l}{2\tau_0}\right)^2 &\propto \eta P_l \quad \text{for } \tau_l \ll 2\tau_0 \\
 E_{\infty} &\propto \sqrt{\eta P_l} \quad \text{for } \tau_l \gg 2\tau_0
 \end{aligned}
 \tag{1.21}$$

where τ_0 is the so called reference time, i.e. the time the proton remains in the vicinity of the accelerating surface charge, P_l the laser power. Eq. 1.21 has been used to fit the experimental data shown in figure 1.3.

A different approach is the one reported in [68], where an isothermal, time-limited fluid model is used. In the model, a single free parameter is defined: the acceleration time τ_{acc} . Following this approach, the proton energy cut-off is expressed by:

$$E_{max} = 2T_h [\ln(t_p + \sqrt{t_p^2 + 1})]^2
 \tag{1.22}$$

where $t_p = \omega_p \tau_{acc} / \sqrt{2exp}$ is the normalized acceleration time, ω_p the plasma frequency and T_h is the temperature of hot electrons.

1.3.3 Radiation Pressure Acceleration regime

For laser intensities higher than 10^{22} W/cm², the TNSA regime starts to lose its efficiency, for the benefit of different acceleration mechanisms. Another possible acceleration regime, is the so-called Radiation Pressure Acceleration (RPA), which is expected to lead to the acceleration of ions up to relativistic energies. Several simulations and theoretical models have confirmed that the RPA starts to dominate with respect to the TNSA regime at higher laser pulse intensity. Indeed simulations have also shown that if a thin target is irradiated with an intense laser $\sim 10^{23}$ W/cm² the produced ions can reach energies in the GeV/n range. To explain the interaction mechanism, the electromagnetic wave hitting the target surface transferring its total momentum to target atoms: the radiation generates a strong pressure which can be expressed by [2]:

$$P_{rad} = (1 + R - T) \frac{I}{c} = (2R + A) \frac{I}{c}
 \tag{1.23}$$

where I is the laser intensity and R , T and A are respectively the reflection, transmission and absorption coefficients, depending on the laser frequency ω , as resulted in Fresnel formulation. Radiation pressure is related to the total steady ponderomotive force on the medium, responsible of electron and ion acceleration. According to the target dimension, i.e. the thickness, different RPA regimes may occur, as for instance the *hole boring* process [71] and the *light sail* regimes describing, respectively, the acceleration with thick and thin target.

Hole Boring regime

In the interaction with thick target, thicker than the skin layer in which ion acceleration by the space-charge field occurs, the radiation pressure action drives a parabolic deformation of the plasma surface allowing the laser pulse to penetrate deeply into the target; this process is commonly named hole boring or *sweeping acceleration* [72] or *laser piston* [73], and it is associated with ion acceleration at the front side of the target. It has been observed that at the instantaneous frame, when the surface is at rest, incoming ions are bouncing back at the surface. The radiation pressure, must therefore balance the momentum flow. The fastest ions are those bouncing back from the surface in the moving frame, resulting in a maximum energy per nucleon in the laboratory frame given by [74]:

$$\begin{aligned}
 E_{max} &= 2m_p c^2 \frac{\Pi}{1 + 2\Pi^{1/2}} & v_{HB} &= \frac{\Pi^{1/2}}{1 + \Pi^{1/2}} \\
 \Pi &= \frac{Zn_c m_e a_0^2}{An_e m_p}
 \end{aligned}
 \tag{1.24}$$

where v_{HB} is defined as the recession velocity of the plasma surface. Such model and related Particle In Cell (PIC) simulations show that the ions pile up at the end of the skin layer producing a sharp density spike and causing hydrodynamical breaking and collapse of the electron equilibrium. This process leads to the production of narrow high-energy bunch of fast ions.

Light Sail regime

The situation described before changes when a target is thin enough so that all the ions are accelerated before the end of the laser pulse, i.e. a complete hole boring occurs. In such a case, the laser pulse is able to further accelerate ions to higher energies since the ions are not screened by a background plasma anymore [75]. The analytical solution and scaling laws provided by such basic model (Simmons and McInnes, 1993 [76]) are useful to illustrate the most appealing features of RPA (Light Sail), such as high conversion efficiency in the relativistic limit and the possibility to achieve very high energies with foreseeable laser and target technology (Fig. 1.4).

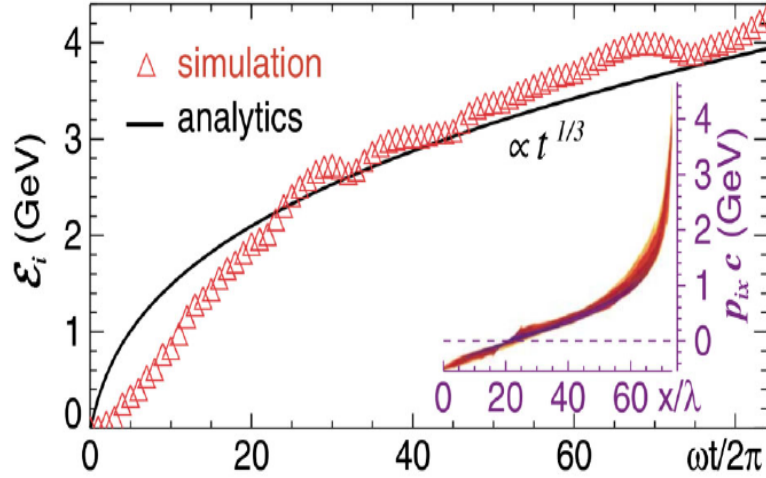


Figure 1.4: The maximum ion kinetic energy as a function of time and the ion phase-space projection (x ; p_x). The solid line corresponds to the analytical calculation according to the Light Sail model [11].

1.4 Power lasers: state of the art, perspectives and possible applications

Currently, the high power laser systems available all over the world are mainly situated in North America (US and Canada), Europe (including Russia), and the Asian-Pacific region

(including India). Figure 1.5 shows the situation of the maximum achieved proton energy as a function of laser irradiance expressed in $\text{W}/\text{cm}^2\mu\text{m}^2$ as a result of many experiments carried out in the main laser facilities. The results are referred to three different pulse durations, to highlight the two different trends, the shallower one corresponding to a $\sim I^{1/2}$ dependence, and the steeper one to a scaling proportional to I [66].

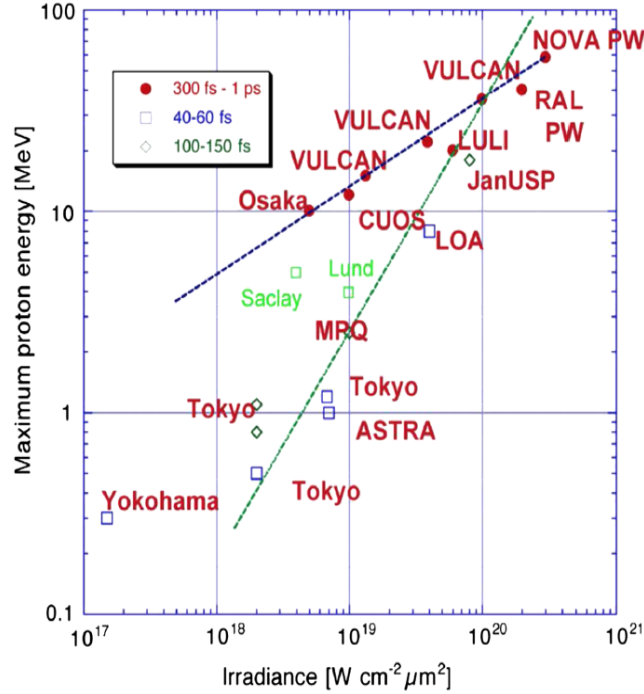


Figure 1.5: Survey of TNSA proton cut-off energies measured in experiments so far versus irradiance for three pulse duration ranges [66].

Moreover, in table 1.3, energy, pulse duration, wavelength, intensity and power of the main available laser systems all over the world are reported to give an overview of the current status.

As it is shown in figure 1.5, the maximum accelerated energy for protons so far is of 58 MeV, observed in the experiment carried out at the NOVA Petawatt laser at LLNL and reported in [7]. Furthermore, a recent experiment carried out with the high-contrast Trident laser at Los Alamos National Laboratory, has observed a maximum proton energy cut-off of 67.5 MeV as discussed in [8].

Name	Lab	Country	Type	λ [μm]	Energy [J]	τ_L [fs]	P [TW]	I_L [W/cm^2]
Petawatt	LLNL	USA	Nd:glass	1053	700	500	1300	$> 10^{20}$
VULCAN	RAL	UK	Nd:glass	1053	423	410	1030	$1.05 \cdot 10^{21}$
PW Mod.	ILE	JP	Nd:glass	1054	420	470	1000	10^{20}
PHELIX	GSI	D	Nd:glass	1064	500	500	1000	-
LULI PW	LULI	F	Ti:Sa	800	30	300	100	-
APR PW	APR	JP	Ti:Sa	800	2	20	100	$2 \cdot 10^{19}$
-	FOCUS	USA	Ti:Sa	800	1.2	27	45	$8 \cdot 10^{21}$
ALFA 2	FOCUS	USA	Ti:Sa	800	4.5	30	150	10^{22}
S. Jaune	LOA	F	Ti:Sa	800	0.8	25	35	10^{19}
Lund TW	LLC	SW	Ti:Sa	800	1	30	30	$> 10^{19}$
MBI Ti:Sa	MBI	D	Ti:Sa	800	0.7	35	20	$> 10^{19}$
Jena TW	IOQ	D	Ti:Sa	800	1	80	12	$5 \cdot 10^{19}$
ASTRA	RAL	UK	Ti:Sa	800	0.5	40	12	10^{19}
USP	LLNL	USA	Ti:Sa	800	1-10	100-30	10-100	$5 \cdot 10^{19}$
UHI 10	CEA	F	Ti:Sa	800	0.7	65	10	$5 \cdot 10^{19}$

Table 1.3: Multi-Terawatt laser systems and laboratories worldwide [77].

In this contest, a growing interest of the scientific community towards the possible applications of laser-accelerated particles beams is leading to develop high power laser technology, in the range between 1 PW and 10 PW. The main challenge is, infact, to increase the maximum energy and intensity of accelerated protons and ions in order to make them more feasible for the applications.

Figure 1.6 shows the European state projects (already under development) towards the PW regime.

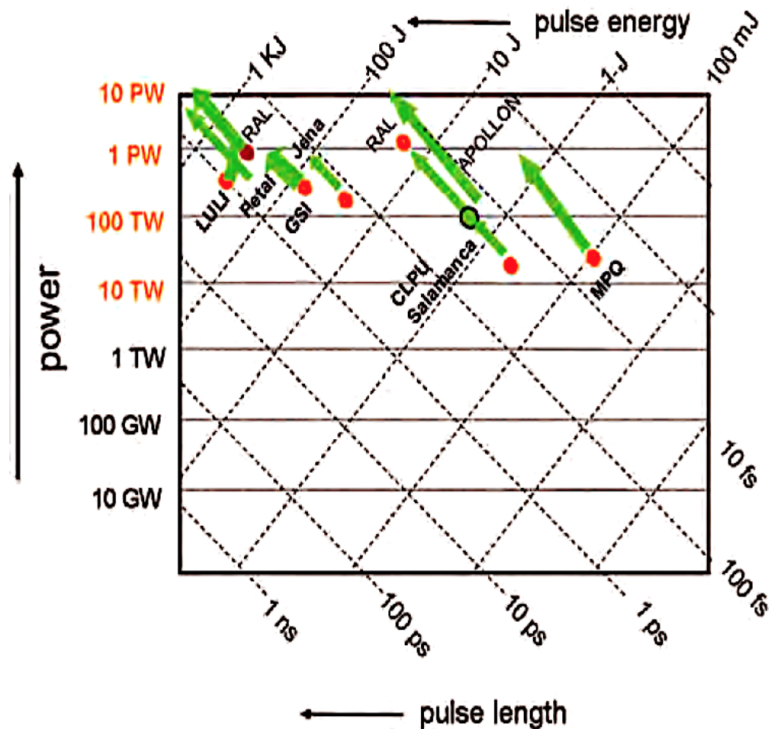


Figure 1.6: Diagram (laser energy, versus pulse duration and laser power) of the current status and future perspectives for the main European projects.

In particular, laser-driven ion beams show peculiarities very attractive for medical applications, as the hadrontherapy, representing, in a future perspective, a potential alternative acceleration method for such kind of application. The high particle fluxes per shot and dose-rate of laser-driven beams observed in [12], if well controlled, could provide an alternative and powerful tool for dose delivery, offering new opportunities for the therapeutic

purposes of charged particles. Nevertheless, despite the great recent progresses in this field, before clinical applications of laser-accelerated particles several tasks need to be fulfilled. New solutions for the laser-driven ion beam transport and energy selection as well as for beam dose and flux detection have to be investigated in order to obtain reproducible beams and use them for clinical applications. Several international collaborations have been established in the last years aiming to explore the feasibility of laser-driven sources for potential medical applications and many research centers have been involved in the investigation of laser driven therapy and applications. As for instance: the LIBRA (Laser Induced Beams of Radiation and their Applications) project [16] at the Queen's University of Belfast (UK), the onCOOPTics [17] (High-Intensity Lasers for Radiooncology) cooperation between the centers of innovation OncoRay in Dresden and the Helmholtz-Zentrum Dresden-Rossendorf (HZDR), the MAP network [18] at Munich-Centre for Advanced Photonics in Munich, the ion Acceleration Program at BNL ATF and UCLA [19] and the european project ELI (Extreme Light Infrastructure).

Chapter 2

The ELIMAIA transport, diagnostics and dosimetry beam line at ELI Beamlines

2.1 The Extreme Light Infrastructure (ELI)

In the last ten years, a new type of large scale laser infrastructure specifically designed to produce the highest peak power and focused intensity was heralded by the European Community: the Extreme Light Infrastructure, ELI. ELI was designed to investigate new generation of compact laser systems, characterized by high intensity, with a power higher than PW, energy of the order of kJ, time duration over 10 fs and laser spot of tens of micrometer [78]. These laser characteristics give to ELI the possibility to investigate new high-energy regimes for electrons, gamma and charged particle generation, being of particular interest for several physics field such as nuclear physics, high energy physics and applied physics. ELI will be indeed the first infrastructure dedicated to the study of fundamental laser-matter interaction and possible multidisciplinary applications in the ultra-relativistic regime, $I > 10^{24} \text{ W/cm}^2$ able to deliver high-pulsed and high energy radiation of femtosecond and attosecond duration. Figure 2.1 shows the laser focused intensity evolution over the years. These intensities represent a formidable leap of 3 or 4 orders of magnitude over today's performance. They are called ultra relativistic intensities because

of their capability to accelerate not only electrons but also ions to the speed of light.

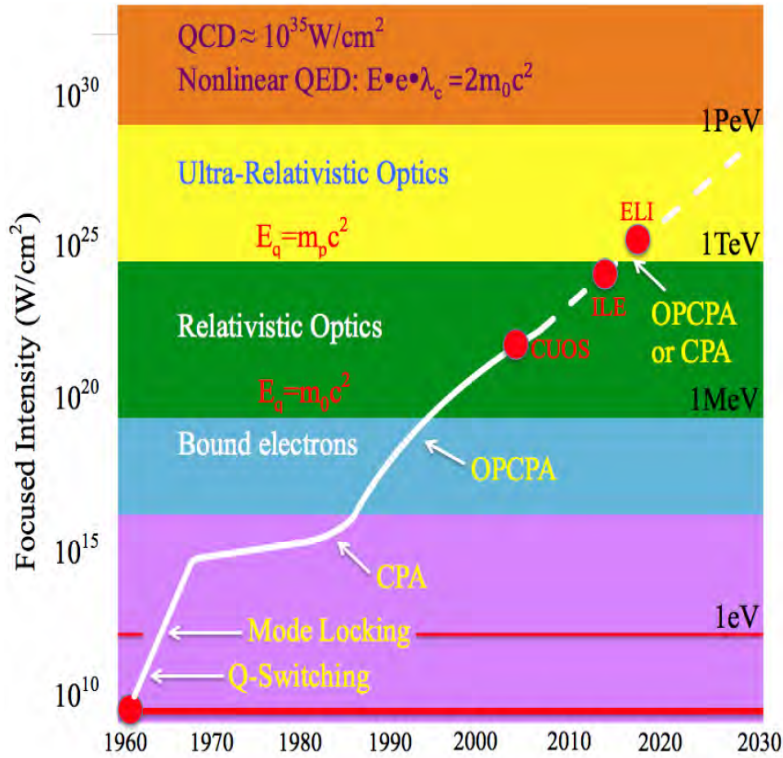


Figure 2.1: Scheme of the laser intensity over the years [78]. .

For this reason, the research will be of particular scientific interest also for applications such as medical ones including hadrontherapy and radiotherapy.

The scheme in figure 2.2 summarizes the ELI infrastructure project development. ELI is being built within the ESFRI (European Strategy Forum for Research Infrastructure) process and it will be the first large infrastructure born from a coordinated effort and collaboration of multinational scientific communities in Europe.

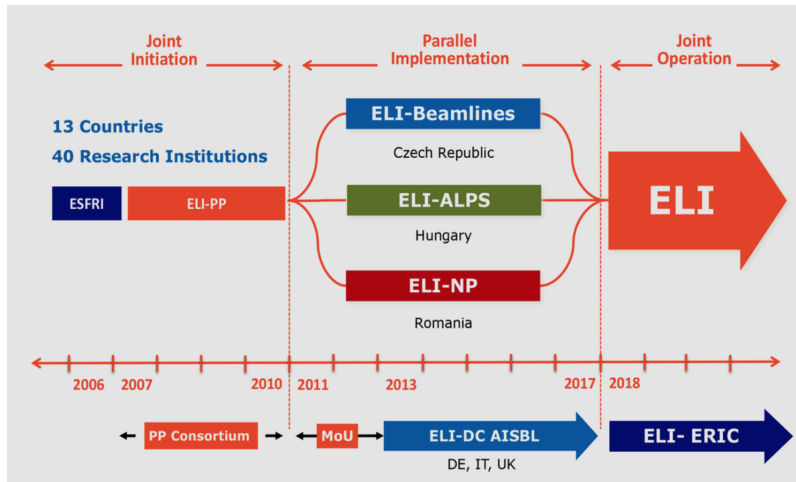


Figure 2.2: Schetch of the ELI organization [79]

The project includes the construction of four European pillars, consisting in different facilities placed in developing European countries. Three of them are in construction and by the end of 2018 will be opened for user’s applications.

The ELI’s pillars are:

- ELI Beamlines (ELI-BL) in Czech Republic in Dolní Břežany (Prague), it is focused on short pulse X rays generation and charged particle acceleration and their muldisciplinary applications.
- ELI-Nuclear Physics (ELI-NP) in Romania, it is addressed to ultra intense gamma rays pulses production for fundamental physics investigation.
- ELI-Attosecond Light Pulse Source (ELI-Alps) in Hungary and it is devoted to the generation and applications of ultra-short pulses with a very high repetition rate.
- The fourth site for Ultra-High-Field Science centred on direct physics of the unprecedented laser field strength is yet to be decided.

Figure 2.2 shows the time evolution of the ELI project, starting from the *preparatory phase* (PP) from 2007 to 2010 with the involvement of 13 countries and 40 international

institutions, followed by the parallel *implementation phase* of the three facilities expected to finish at the end of 2018 and finally the *operation phase*, in 2019, after which the three pillars will operate as an international laser facility open to the access international user community.

2.1.1 ELI Beamlines facility

The ELI Beamlines facility, located in Dolní Břežany (Prague) is dedicated to the study of gamma and charged particle (electrons and ions) production and in the development of new technologies for any kind of their possible multidisciplinary applications. To achieve such purpose high repetition rate and high power laser system, respectively up to 1 kHz and 10 PW, will be employed. The laser building is composed of three floors as shown in figure 2.3. The first floor is dedicated to the auxiliary system, as the cryogenic pumps and the power supplies, the ground floor will host the laser systems and the basement the experimental halls.

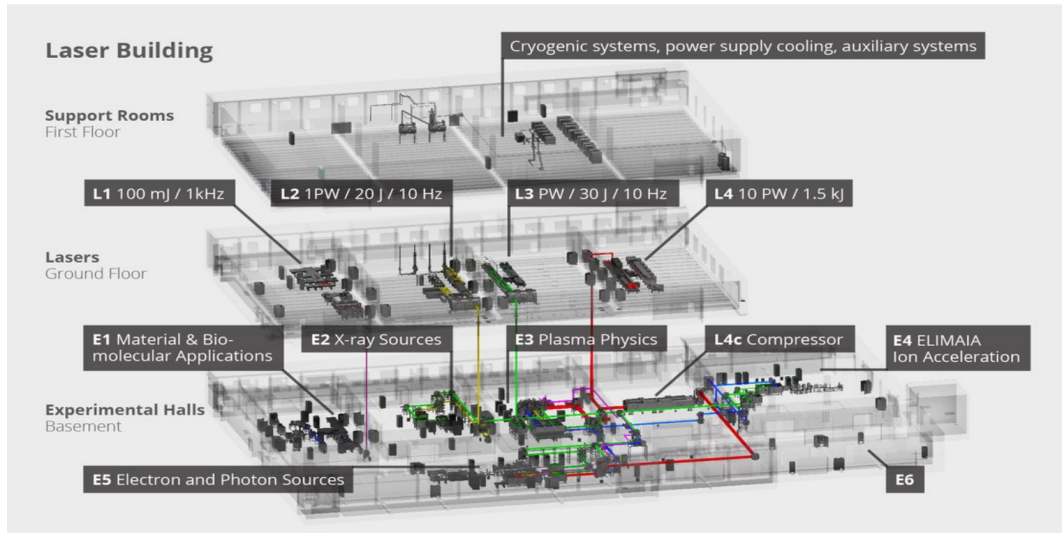


Figure 2.3: Laser building showing available laser systems and experimental hall.

As shown in figure 2.3, four laser systems will be installed at ELI Beamlines, each one with different characteristics according to the physics field of interest [79]:

- L1: 100 mJ, <20 fs, 100kHz. The laser is based entirely on amplification of frequency chirped picosecond pulses in an optical parametric chirped pulse amplification (OPCPA) chain consisting of a total of seven amplifiers.
- L2: 1 PW, 20 J, 20 fs, 10 Hz. The main amplifiers are based entirely on optical parametric chirped pulse amplification (OPCPA), allowing for extremely short pulses with durations below 15 fs to be generated.
- L3: 1 PW, 30 J, 30 fs, 10 Hz. The laser system is called HALPS (The High-Repetition-Rate Advanced Petawatt Laser System) and was developed at the Lawrence Livermore National Laboratory, with ELI Beamlines cooperating on the development of the PW pulse compressor, the short-pulse diagnostics, and the short-pulse part control and timing.
- L4: 10 PW, 1 kJ, 130 fs, 0.01 Hz. It is the laser devoted to the reaching of unprecedented power peak of the laser.

Five different experimental rooms will be available at ELI Beamlines, each one of them dedicated to specific physics researches:

- E1 will house laser-driven secondary sources and experimental end-stations for applications in molecular, bio-medical, and materials sciences. It will use the L1 laser.
- E2 will be dedicated to the generation of ultrafast and bright hard X-ray beams for user experiments. The X-ray beam lines rely on focusing the L3 laser into a gas jet or a gas cell. For an appropriate choice of experimental parameters (laser intensity, laser spot size and duration and electron density in the gas), electrons are accelerated to relativistic energies by plasma wakefield acceleration and wiggled by the plasma itself (Betatron source) or by a second laser pulse (Compton source).
- E3 is the plasma physics platform as well as a multi-functional experimental infrastructure designed to perform laser-plasma and laser-matter interaction research

mainly on the following topics: High energy density physics (HEDP), Warm dense matter (WDM), Plasma optics (PO), Laboratory astrophysics (LA), Ultra-high intensity interaction (UHI).

- E4 is a user-oriented beam line addressed to multidisciplinary application of laser-driven ions and secondary source. The experimental hall is also called *ELI Multidisciplinary Applications of laser-Ion Acceleration (ELIMAIA)* and will be described in details in the next section.
- E5 will be dedicated to the electron acceleration and to X-ray user experiments. The High-energy Electron by Laser Light (HELL) experimental platform and the Laser Undulator X-rays (LUX) are located in the experimental hall E5.

2.2 ELIMAIA beam line

The ELIMAIA experimental hall is the room dedicated to the ion acceleration and their possible multidisciplinary applications. The design of the beam line followed the main idea to get a user-friendly approach in monitoring reliable beams providing different dosimetric end-points as well as in-air irradiation points available for users. The 3D design of the ELIMAIA beam line is shown figure 2.4. Both laser systems L3 and L4 can be delivered to E4 according to the specific purpose of the user's experiments.

ELIMAIA is composed of two main sections: the section devoted to the ion acceleration and targetry, consisting of two interaction chambers, the plasma mirrors and laser diagnostics and addressed to the optimization of the laser-matter interaction for ion acceleration, and the ELIMED section, dedicated to the in-vacuum accelerated ion beam transport and in-air dose measurement and irradiation.

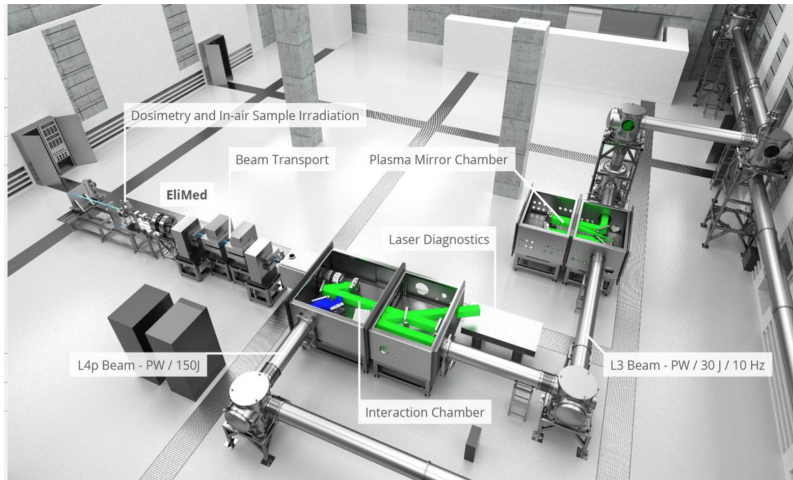


Figure 2.4: 3D design of the ELIMAIA beam line.

2.2.1 The ELIMED section

Within the context of the growing interest of the scientific community towards possible applications of high-energy laser-driven ion beams, in 2011, a collaboration between the ASCR-FZU (Institute of Physics of the Czech Academy of Science) [20], in charge for the ELI Beamlines facility implementation, and INFN-LNS (Italy) was established. The goal was to demonstrate the real possibility to make suitable high pulsed laser-driven beams for multidisciplinary applications, developing specific transport, diagnostics and dosimetry elements for this purpose. Thanks to this collaboration, named ELIMED, in 2014 a three-years contract was signed between the two institutions, giving to INFN-LNS the responsibility to develop and realize a whole beam line aimed to transport, handle laser-driven ion beams and make them suitable for multidisciplinary applications using innovative detectors for the beam diagnostics and dose measurement down to the irradiation point [21, 22]. The ELIMED beam line will be installed in E4 experimental hall at ELI Beamlines at the end of the 2017. The main challenge of the project is, indeed, to realize a transport beam line able to deliver reproducible and controlled ion beams up to 60 MeV/n in terms of energy spread and angular divergence and delivered dose to users interested in multidisciplinary applications of optically accelerated ion beams. The

expected characteristics of the laser-driven ion beams after the transport and the energy selection, at the irradiation point are listed in table 2.1. As one can see, the main goal is to obtain controllable beams, focused and selected in energy with a reduced angular and energy spread, assuring at the same time a particle transmission and dose delivered per shot.

Ion beam features (PW)	Enabling Experiments	Flagship Experiments
Energy range	3-60 MeV/u	3-300 MeV/u
Ion No./laser shot	$<10^9$ in 10% BW	$>10^{10}$ in 10% BW
Bunch duration	1-10 ns	0.1-10 ns
Energy spread	$\pm 5\%$	$\pm 2.5\%$
Divergence	$\pm 0.5\%$	$\pm 0.2\%$
Ion spot size	0.1-10 mm	0.1-10 mm
Repetition rate	0.01-1 Hz	0.01-10 Hz

Table 2.1: Expected beam characteristics for enabling and flagship experiments.

The expected high repetition rate of the laser shot makes the ELIMAIA beam line particularly suitable for applications, giving the possibility to deliver extremely high particle flux at the irradiation point, accumulate a given dose, and perform the irradiation according to the user requirements.

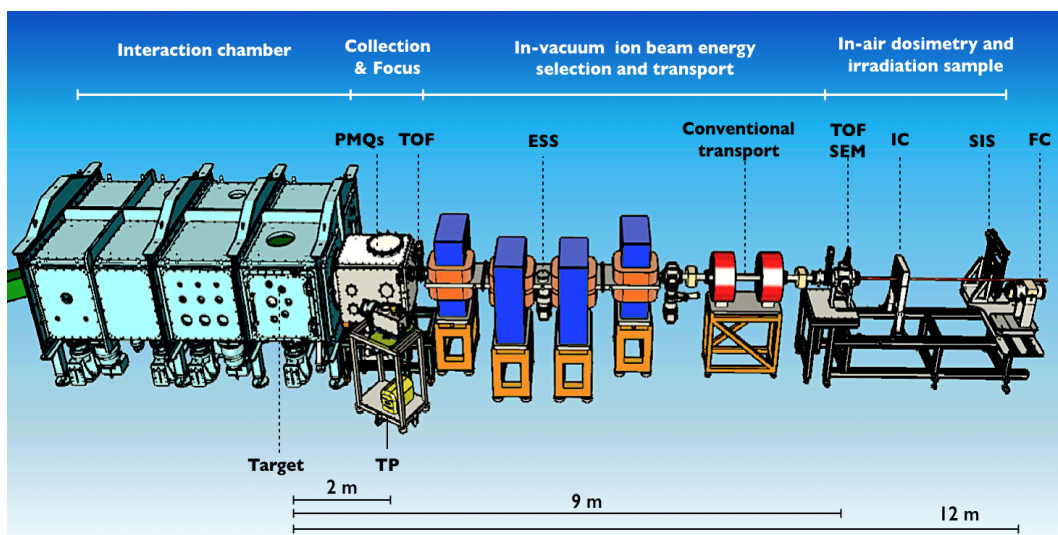


Figure 2.5: Layout of the ELIMED beam line showing all the components: the Permanent Magnet Quadrupole system (PMQs), the Time Of Flight diagnostics (TOF), the Energy Selector System (ESS), the standard transport elements, the Secondary Emission Monitor (SEM), the Ionization Chamber (IC), the Faraday Cup (FC) and the Sample Irradiation System (SIS).

Figure 2.5 shows the design of the ELIMED beam line indicating the main elements. The ELIMED beam line is a modular system, composed by three main components [80]

- Ion beam collection and diagnostics
- In vacuum ion beam energy selection, transport and diagnostics
- Dosimetry and sample irradiation system

The first two sections of the beam line are devoted to the in-vacuum transport of the beam, consisting in collection, focus and energy selection of the beam according to the specific ion species and energy component of interest. Along the beam line the beam energy spectrum and fluence are measured with diamond and silicon carbide detectors used with a TOF technique, to assure shot-to-shot monitoring and deliver a stable beam at the irradiation point. The beam coming out from Energy Selector System (ESS) will have characteristics similar to the conventional beams and, hence, easy to transport and modulate in shape

with conventional magnetic lenses, such as resistive quadrupoles and steerers. The latter will be placed downstream the in-vacuum beam-line as shown in figure 2.5 and will be used to manage the beam shape and focus to inject in the in-air final section. The last section, it is devoted to the in-air transport and measurement of the dose delivered using relative, in transmission, and absolute dosimeters in order to monitor the dose released shot-to-shot to the samples placed at the end of the beam line.

Moreover, a complete Monte Carlo simulation of the whole ELIMED beam line, reproducing the beam transport through each element of the beam line downstream the irradiation point, has been developed in order to provide the users with a useful tool to simulate different experimental setups and configurations to optimize the experiment preparation. Each section of the beam line will be described in details in the next sections 2.2.2-2.2.5.

2.2.2 Ion beam collection and focusing system

Due to the large angular divergence of the accelerated particles which may be as broad as 20-30° half angle, in order to collect the largest number of particles, and ensure a good transmission efficiency and controlled beam size and divergence, the first section of the ELIMED beam line is composed of a set of five permanent magnet quadrupoles (PMQs) designed to focus ions up to an energy of 60 MeV/u. Optics simulations of the PMQs system have been performed using analytic transport codes to define the geometrical size of the collection system and optimize the beam injection in the energy selector system, assuring a good transmission efficiency. The PMQs characteristics are summarized in table 2.2 [81, 82].

N. PMQs	Geometric Length	Field Gradient	Bore Diameter
1	160 mm	101 T/m	30 mm
2	120 mm	99 T/m	30 mm
2	80 mm	94 T/m	30 mm

Table 2.2: Geometric and magnetic specifications for the designed PMQs.

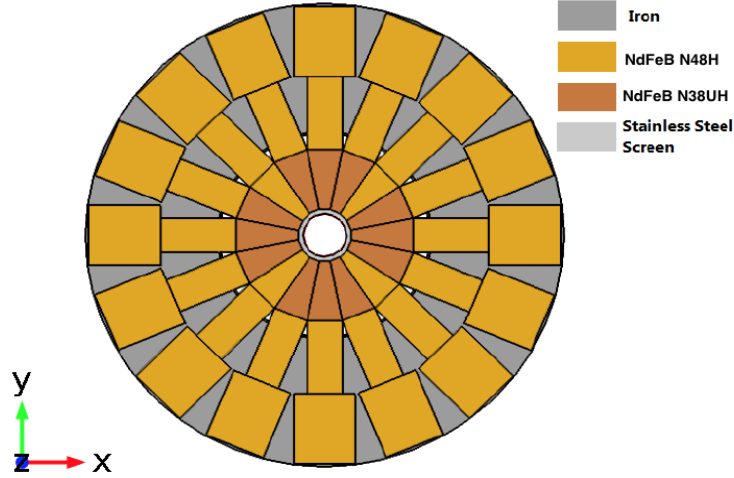


Figure 2.6: PMQ layout. The different colors are referred to the different material used [81].

PMQs are based on a standard trapezoidal Halbach array [83] surrounded by two external hybrid arrays made of rectangular magnetic blocks and iron. The inner array, 122 mm in diameter mainly guarantees the field quality of the quadrupole, the two external arrays, respectively 223 mm and 322 mm diameter, are necessary to increase the volume of the permanent magnet material to reach the required field gradient. A scheme of the PMQs layout is shown in figure 2.6

As one can see in Fig.2.6, the two external arrays are placed within an iron frame acting as a supporting structure as well as magnetic flux guide. The inner array consists of two different permanent magnet alloys (NdFeB N48H and NdFeB N38UH) with different characteristics. This choice has been done to solve local demagnetization phenomena which might occur due to the high magnetic field value inside the bore, reaching a maximum value of about 1.8 T. This issue can be solved mixing materials with different coercitivity in some key places of the array [81, 82].

In order to assure a good transport for ions with energies ranging from 3 MeV/n up to 60 MeV/n, the quadrupole system is mounted on translation stage such that the distance between the laser-target interaction point and the quadrupoles can be varied using a

remote control system. Moreover, the number of the PMQs can be changed, according to the specific ion species and energy component to focus and inject in the Energy Selector System. Optics simulations of the ion collection system have been performed in order to define the PMQs system geometrical configurations in terms of number of quadrupoles, distances in between them and ensure the best transmission efficiency for any specific requirements. Figure 2.7 shows a scheme of five quadrupoles and a picture of the PMQs manufactured by the SigmaPhi company following the INFN-LNS design.

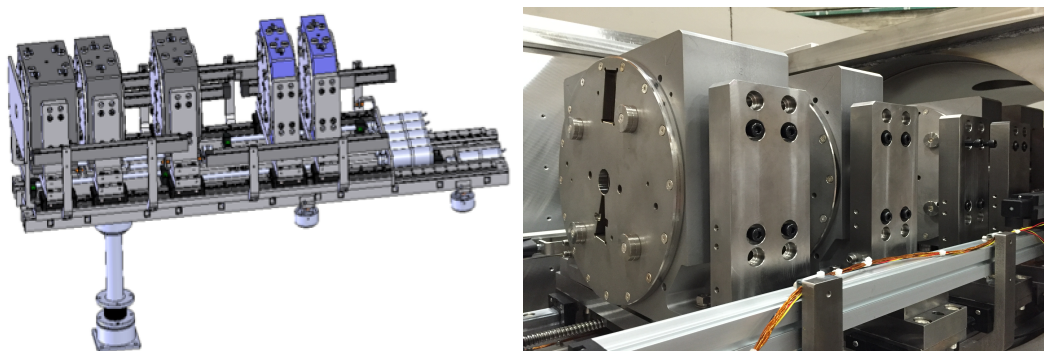


Figure 2.7: Layout and picture of the realized PMQs system mounted in its translational and movement system.

2.2.3 Diagnostics system

In order to monitor the particle transport and injection from the PMQs system to the ESS, two diagnostic devices are placed downstream the PMQs to measure emittance, energy spectrum and flux. The diagnostics system will consists of two elements:

- A detector, based on the well-known pepper-pot method, specifically designed and optimized for single shot emittance measurement of laser-driven proton beam placed just right after the PMQs system.
- A detector, namely a Silicon Carbide (SiC) or a Diamond detector, used in Time Of Flight (TOF) configuration, providing fluence/current and energy spectrum measurements.

Due to the broad angular distribution of the particles accelerated from the source characterized by different velocity directions, the beam emittance measurement just after the PMQs system and before the ESS is a crucial step to optimize the beam injection in the ESS. Indeed, the emittance measurement provides a "figure of merit" in the phase-space for describing the quality of the beam in terms of the ability to be transported over long distances and to be focused into a small space with a minimum of divergence [84]. The most common approach to estimate it is to use a pepper pot based system which converts the beam flux density as a function of position into a measurable signal. The detector, designed by the INFN-LNS for beam emittance measurements, is based on the pepper-pot method, consisting in collimating the beam into single smaller beam-lets using apertures of known size: the divergence of these beamlets can be detected and measured after they propagate a sufficient distance. The realized device shown in figure 2.8 is composed of a metallic mask, provided with a set of regular holes, a scintillator screen placed at a sufficient distance from the mask, a mirror placed at 45° to deflect the image and a CCD camera to detect it.

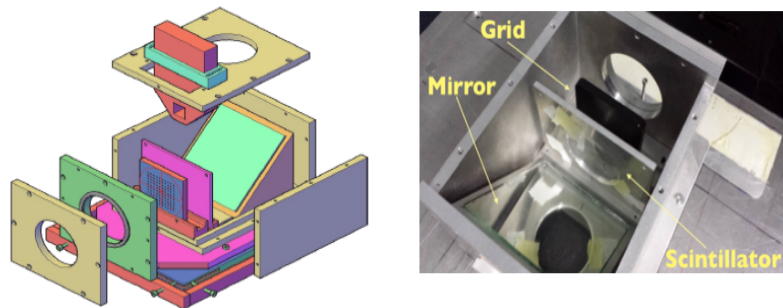


Figure 2.8: 3D solid draw of the device

On the other hand, the energy spectrum of particles leaving the focusing system will be measured with a diamond detector measuring the Time of Flight of the particles and reconstructing the corresponding energy. A second diamond detector will be placed downstream the in vacuum section, after the standard transport section as reported in figure

2.5, to provide fluence and energy bandwidth after the energy selection . The details of the diagnostics system, the TOF method and the analysis procedure developed for high-energy laser-driven ion beams will be presented in chapter 4, being one of the goal of this work.

2.2.4 In vacuum ion beam energy selection

The Energy Selector System (ESS) can be considered as the core element of the ELIMED beam line, being responsible to convert the wide energy spread beam coming out the laser-target interaction into a quasi mono-energetic beam suitable for applications.

A sketch of the ESS is shown in Figure 2.9. The layout is based on four resistive dipoles with alternating magnetic field, similar to a bunch compressor scheme. The main trajectory parameters are also reported in the figure, according to the treatment proposed in [85].

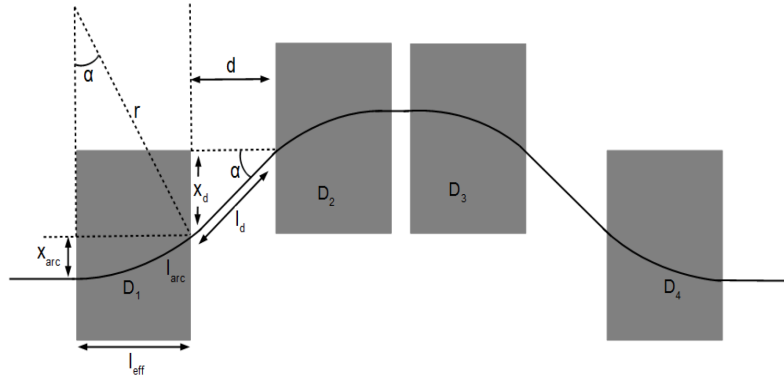


Figure 2.9: Dipole magnets reference trajectory [86].

Using the parameters defining the reference trajectory, it is, indeed, possible to determine analytically the ESS characteristics, in terms of radial and longitudinal dimensions of each dipole, field strength and selection slit size, necessary to have the required energy resolution.

The parameters shown in figure 2.9 are defined as:

- Bending radius: $r = \frac{p}{Be}$ where p is the particle momentum, B the magnetic field value and e the electron charge

- Bending angle: $\alpha = \arcsin \frac{l_{eff}}{r}$ where l_{eff} is the magnet effective length
- Path length in the dipole: $l_{arc} = l_{eff} \frac{\alpha}{\sin \alpha} = r \cdot \alpha$
- Path length between the dipole D1 and D2: $l_d = \frac{d}{\cos \alpha}$ where d is the distance between D1 and D2.
- Total path length in the selector: $L_{path} = 4 \cdot l_{arc} + 3 \cdot l_d$, if all the dipoles are the same in terms of field strength and effective length and are separated by equal drift spaces.
- Horizontal displacement of the trajectory inside a dipole: $x_{arc} = r(1 - \cos \alpha)$
- Horizontal displacement in the drift between two dipoles: $x_d = d \tan \alpha$
- Selection point i.e. the horizontal displacement with respect to the original beam axis introduced in the middle of the chicane: $\Delta x = 2x_{arc} + x_d = 2l_{eff} \frac{1 - \cos \alpha}{\sin \alpha} + d \tan \alpha$

Knowing the definition of all parameters it is then possible to retrieve the relation of the particle energy as a function of the horizontal displacement:

$$\sqrt{\left[\frac{qc(\Delta x - d \tan \alpha)}{2\left(\frac{1 - \cos \alpha}{B}\right)} \right]^2 + M_0^2 c^4} - E_0 \quad (2.1)$$

which represents the calibration equation of the ESS, being q , M_0 and E_0 the parameters of the ion to be selected. The derivative of the previous equation times the slit aperture size s , i.e $\frac{dE}{dx} \cdot s$, gives the energy resolution of the energy selector:

$$E_{res} = \frac{qcB}{2(1 - \cos \alpha)} \cdot \frac{\sqrt{(E_0 + E)^2 - M_0^2 c^4}}{E_0 + E} \cdot s \quad (2.2)$$

Using the previous equations implemented in analytical codes as COMSOL [35] and OPERA [87], different layouts have been investigated for the ESS and the best solution, in terms of compactness and performances, turns out to be the use of a single trajectory based device, as shown in figure 2.10

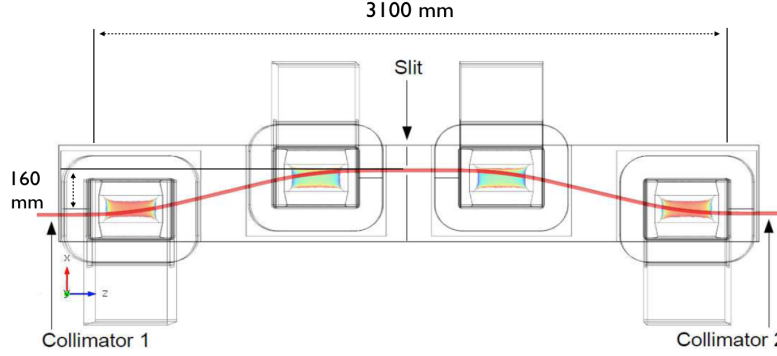


Figure 2.10: Top-view of the ESS dipoles and trajectory. The positions of the slit and the collimators and the total length of the ESS are indicated.

For the designed system each magnet is 400 mm long (effective length 450 mm) and the drift between each magnet is 500 mm long with a total geometrical length of 3100 mm as reported in figure 2.10. The reference trajectory path is 3.168 m. Moreover, the maximum horizontal deflection for the reference trajectory shown in figure is 160 mm at the centre of the ESS, i.e. the slit position. A slit is placed between the two central magnets with a variable aperture from 5 mm to 20 mm to change the energy resolution according to the specific requirement. The use of electromagnetic resistive magnets offers several advantages with respect to a chicane with permanent magnetic field, resulting in an independence of the energy resolution from the selected particle energy. Indeed, in order to have on the reference trajectory particles with a specific q/m and a given energy the magnetic field of the dipoles has to be changed. The magnetic field in ESS designed for ELIMED varies from 0.08 up to 1.2 T to select protons with energy ranging between 3 and 60 MeV and it can reach the value of 1 T to select carbons (C^{6+}) with energies of 70 MeV/u (and protons up to about 300 MeV). The magnetic field value of the electromagnets versus the energy to be selected both for protons and carbon ions C^{6+} analytically calculated is reported in figure 2.11.

Furthermore, an other advantage of resistive dipoles with respect to the permanent magnets is the possibility to reach a high uniform magnetic field inside a large gap, resulting

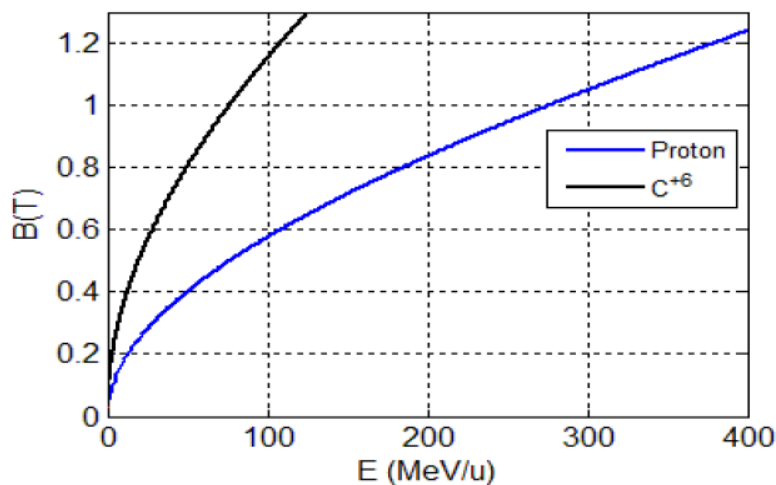


Figure 2.11: Dipole magnetic field versus proton (blue line) and carbon (black line) energy [86].

in a wide acceptance of the magnetic chicane, which assures high transmission efficiency. The dipoles will have a 59 mm gap and will be C-shaped, which allows to reduce the iron mass and to have a more compact device. Two 30 mm aperture collimators will be placed upstream and downstream the ESS at 220 mm from the dipoles respectively. The designed system will allow obtaining controlled particle beams in terms of energy spread, for instance from from 5% up to 20% according to the energy and the transmission needed, angular divergence and transmission efficiency. Figure 2.12 shows a picture of the realized dipoles together with the resistive bobines, during their assembly at SigmaPhi company.



Figure 2.12: Picture of the dipoles during the assembly at SigmaPhi company.

2.2.5 Dosimetry and sample irradiation system

The last section of the ELIMED beam line is dedicated to in-air transport beam, dose measurement and the sampling irradiation. Due to the extreme characteristics of such kind of beams, as the high dose-rate, the short time pulse and the high electromagnetic pulse accompanying the laser-target interaction, the choice of the detectors to be used for dose measurement is very crucial in order to measure a reliable dose value with a sufficient level of accuracy to match the clinical requirements. The applications, such as the medical ones, require, indeed, an accuracy of the measured delivered dose not higher than 5% to assure a controlled dose delivery on the biological cells and to not compromise the effectiveness of a radiation treatment [88]. For conventional clinical beams, a protocol for dose measurement procedure has been established in 2000, indicating the use of specific detectors, as for instance ionization chambers and calorimeters [88]. On the other hands, since no dosimetric protocol is still available for high-pulsed laser-driven ion beams, it is necessary to develop new specific devices for dose evaluation, able to support the high dose-rate and fluence of such accelerated beams.

Several solutions have been investigated to develop relative and absolute dosimeters for the ELIMED beam line as reported in [21, 80, 89].

As shown in figure 2.13, the in-air final section of the ELIMED beam line will be composed

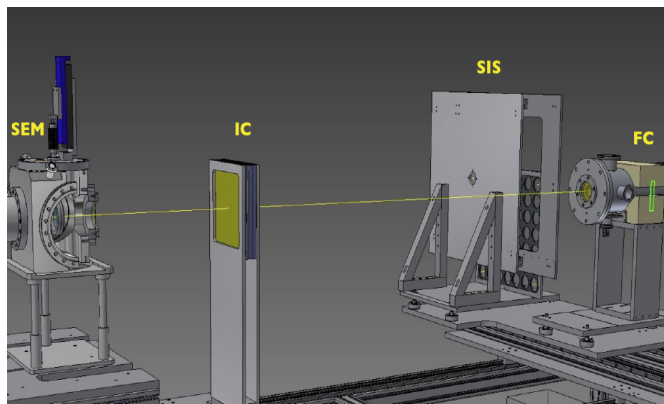


Figure 2.13: Technical drawing showing the dosimetric system composed of a Secondary Emission Monitor (SEM), a in-transmission ionization chamber (IC) and a Faraday Cup (FC) and the sample irradiation system (SIS).

of relative dosimeters, such as a secondary emission monitor (SEM), an in transmission double gap ionization chamber (IC) and a peculiar Faraday cup (FC) as absolute dosimeter. A sample irradiation system (SIS) has been also designed, providing an automatic movement system for efficient irradiation of samples, detectors and cells.

Faraday Cup The expected high-dose rate forces the choice of an absolute dosimeter whose response is completely independent from the delivered beam dose-rate. In such case, one of the most common and studied approaches for clinic absolute dose measurement is the use of Faraday Cup detectors, providing the measure of the collected charge with a dose-rate independent response. For such reason, a Faraday Cup (FC) has been designed and realized for the absolute dose measurement along the ELIMED beam line, as reported in many works [21, 22, 89].

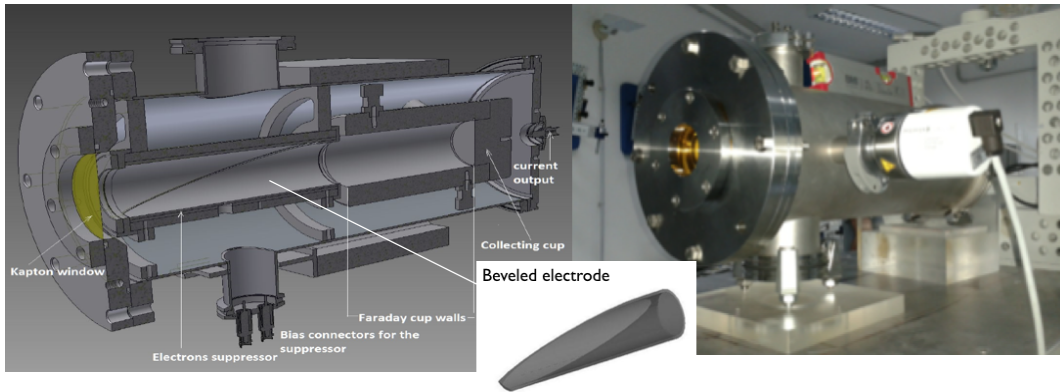


Figure 2.14: Internal structure of the ELIMED Faraday Cup (left) and picture of the FC placed along the CATANA beam line at INFN-LNS(right). In the inset a particular of the beveled inner electrode is also shown.

The ELIMED FC, shown in figure 2.14, consists of a 40 cm aluminium cylinder with an internal radius of 20 mm. The main components are:

- Entrance Window: a 25 or 50 μm kapton window. A thin entrance window is necessary in order to keep the vacuum inside the FC housing and, at the same time, to not perturbate the beam and change the physical properties of the particles.
- Cup: a 50 mm thick aluminium cup. The thickness has been determined in order to stop both the high-energy impinging particles (up to 60 MeV protons) and the secondary ones possibly produced in the interaction with the cup itself.
- Guard ring or suppressor: a 180 mm steel cylindrical suppressor. A certain voltage can be applied to collect the secondary electrons generated in the cup itself and repel those produced in the interaction with the entrance window.

Since the ionization of the residual air could affect the FC measurements, a vacuum of about 10^{-5} mbar is required as working condition. As it is well known, a Faraday Cup is mostly a counter of particle impinging inside the cup allowing to measure the beam charge [90]. Furthermore, thanks to the charge measurement, it is possible to extract the

value of the absolute dose released in water for proton and ion beams using the following expression:

$$D_w = \frac{1}{A_{eff}} \frac{\int S_w(E)N(E)dE}{\int N(E)dE} \frac{Q}{e} 1.60 \cdot 10^{-10} [Gy] \quad (2.3)$$

where A_{eff} [cm^2] is the beam effective area, $S_W(E)$ [$MeV \cdot cm^2 \cdot g^{-1}$] the mass stopping power in water at a given energy E , Q is the measured charge and e is the elementary charge. As it is shown by the equation 2.3, a FC alone cannot provide a measurement of the absolute dose, since the beam effective area and the energy spectrum have to be measured, as well. These three quantities, needed to obtain the dose, can be measured with an high accuracy using the following solutions:

- Charge collection. The developed FC is provided of an additional inner electrode with a special beveled shape to increase the charge collection efficiency and minimize the uncertainties due to the secondary electron production in the entrance kapton window and in the cup itself. The second electrode, which can be added within the standard cylindrical FC suppressor, allows creating an asymmetric electric field, which helps to deflect the unwanted secondary electrons produced in the interaction between the incident beam and the window and to collect the ones created in the interaction with the cup. As it has been reported in [89], simulation studies with the SIMION software and the Geant4 toolkit have been performed to determine the best configuration for the proper applied voltage. The use of this innovative electrode assures to optimize the accuracy on the measure of the charge collected.
- Beam area. Considering the high dose-rate expected, Radiochromic films (RCFs) will be used to measure the area of the beam entering the FC, providing a good spatial resolution (order of tens of μm). RCFs are dose-rate independent relative dosimeters that allow to measure the delivered dose, giving 2D dose distributions, once calibrated against an absolute dosimeter. RCFs consist of a single or double layer of radiation-sensitive organic microcrystal monomers, on a thin polyester base with a transparent coating. Due to polymerization of monomers by ionizing ra-

diation, the active layer colour becomes darker and, quantitatively, it is measured through the optical density (OD) of the film. Different types of RCFs are available on the market and can be chosen for different applications, such as the EBT3 and the HD-V2 types, which can cover all possible requirements related to laser-driven beams measurements. In order to obtain the beam profile or the delivered dose from the RCFs, raw images of the films have to be acquired by scanning them in transmission with a flatbed colour scanner. By means of dedicated analysis software, it is possible to calculate the beam profiles in the transversal plane and, consequently, the beam area. As an example, an image of the EBT3 film irradiated with clinical 62 MeV proton beam together with the obtained correspondent transversal profile is reported in figure 2.15.

- Energy spectrum. RCFs will be also used in a stack configuration, considering that ions with lower energy stop in the first layers whereas the ones with higher energy penetrate deeper layers. Knowing the thickness, composition and density of each RCF, it is possible to retrieve the energy spectrum through an iterative procedure based on deconvolution methods.

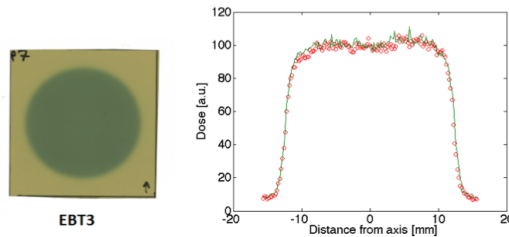


Figure 2.15: EBT3 gafchromic film irradiated with 62 MeV clinical proton beam (left) and the corresponding transversal profiles reconstructed with the software (right).

Ionization chamber In order to monitor the released dose on-line, a double-gap ionization chamber will be used as in-transmission relative dosimeter. After a calibration against the Faraday Cup, the multi-gap in transmission chamber will represent the refer-

ence dosimeter allowing to measure the dose delivered shot-to-shot. Due to the high peak current of laser-driven ion beams, which cause a not-negligible recombination effect inside the chamber gas, no conventional ionization chambers can be employed and innovative solutions have been studied.

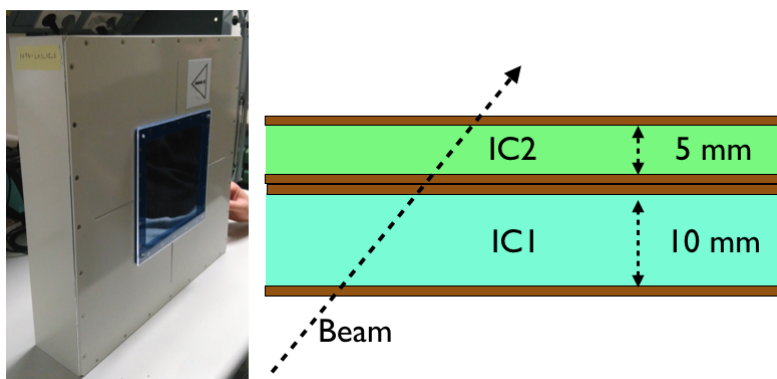


Figure 2.16: Picture and scheme of the internal structure of the multi-gap ionization chamber

The ionization chamber realized for the ELIMED beam line consists of two gaps of different thickness, filled with air or nitrogen, and characterized by different recombination effects and charge collection efficiencies. The high flux of expected beam increases the recombination phenomena causing an inefficient charge collection. The use of two gaps allows to determine the charge collection efficiency of one of them by measuring the ratio between the charge collected in the two chambers. As it is known, the collection efficiency depends on the voltage applied to the gap, V , the electrode distance, d , and the ionization charge density, n_0 : for a fixed voltage and distance between the electrodes, the ratio of the currents in the different gaps depends uniquely on the ionization charge density n_0 . Applying the Boag theory, which predicts the charge recombination, and by fitting the curves of the efficiency as a function of the applied voltage it is possible to determine the n_0 parameter as reported in [91]. The structure of the multi-gap chambers is shown in figure 2.16. It consists of a 10 mm layer followed by a 5 mm layer, i.e. the two gaps, the anodes and cathodes where to apply the electric field and two thin entrance Mylar

windows. The charge is collected connecting the IC to an electronic circuit based on a chip [92], that allows a reading of digitized current collection at the anode of each chamber. The charge measurement principle of the chip is based on counting the number of times that an input capacitance, loaded by the current coming from the detector and discharged by the circuit itself, reaches a threshold value set.

Secondary Emission Monitor (SEM) The SEM [93, 94] is a thin metallic foil detector based on the secondary electron emission (SEE). When a multi-MeV charged particle passes through an interface of a solid material and loses energy, very low energy electrons are emitted from the surface, generating a signal proportional to the incident charged particle current. The SEM is basically an on-line beam current monitor and will be used in trasmission downstream the in-vacuum beam-line section, in front of the kapton window to monitor the particle flux. As shown in figure 3.15 it can be made of different thickness of tantalum foils and it will be provided with an actuator to easily put and remove it from the beam axis direction if needed.

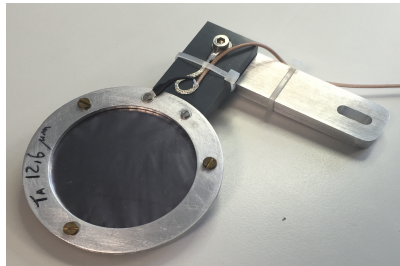


Figure 2.17: Secondary Emission Monitor realized for the ELIMED beam line

Chapter 3

Geant4 simulation of the ELIMED beam line

The ELIMED beam line for the transport of laser-driven ion beams, including the detectors for dosimetry described in the section 2.2.5, have been fully simulated using the Monte Carlo simulation toolkit Geant4.

In order to study the future feasibility of laser-driven ion beams in medical physics, several tasks have to be accomplished like the possibility to predict the biological effects of these high pulsed beams on human body according to the dose absorbed during the irradiation. For this reason, the simulation of the ELIMED beam line, is of crucial importance for ELI Beamlines, because it will be a powerful and reliable tool to predict the beam transport from the source to the irradiation point through the magnetic elements and to study the dosimetric parameters for possible applications. The Geant4-based simulation will be described in details in the next sections, together with the results obtained performing top-to-bottom realistic simulations.

3.1 Monte Carlo method and Geant4 simulation toolkit

One of the most accurate methods widely used for simulation purposes is the *Monte Carlo* one, based on random numbers generation and belonging to the so-called family of statistic

and not parametric methods.

The name *Monte Carlo* has been initially given by the scientists J.Von Neumann e S. Ulam during the II world war and derives from the famous Casinò, placed in Monaco.

It consists of three main steps:

- Generation of a random number sequence and determination of the *input* variable depending on the chosen probability distribution
- Determination of the *output* variable
- Repetition of the previous points and comparison of the results in order to establish the combination which better reproduces the process

The randomness of the generated numbers is a key requirement for the reliability of the final results. Nevertheless, the use of a calculator as random numbers generator does not allow to obtain a perfect random sequence because it needs a deterministic algorithm to perform the calculation. Hence, the number sequence generated by a calculator will be a *pseudo-random* number sequence because a pre-established relation between a sampled number and the previous one exists. The entire sequence depends on the first number of the chain which is called *seed*.

The Monte Carlo method results more efficient than the analytic and deterministic methods especially when the complexity of the problem to solve is very high. The time needed to solve a problem is strictly connected to the complexity and the resolution time increases more slowly with the complexity of the problem using Monte Carlo method as respect the deterministic computations [95].

Several types of simulation codes based on the Monte Carlo method have been developed and used in different fields of application. In particular, many codes for particle tracking have been distributed in recent years in order to accurately reproduce the physical processes and to predict the particle transport in the matter. One of the most used simulation codes in the high energy physics field as well as for applications is the toolkit Geant4, which will be explained in details in the following section.

3.1.1 The Geant4 toolkit

The simulation software Geant4 (GEometry ANd Tracking) [23, 24] is one of the most widely used Monte Carlo codes for particle interaction and transport in the matter. This toolkit is currently used in several fields, from High Energy Physics to medical physics and space science, thanks to its advanced functionalities in the geometrical description and to a wide and well-tested set of physics models.

The first version of the code has been released in 1974 at CERN (Geneva CH) in order to simulate the interaction of high energy elementary particles with detectors. This first version was limited to a few transported particles and simple detector geometry. In 1982 the initial code evolved through Geant3, written in Fortran. It allowed to simulate very big experimental apparatus and the transport of intense and high energy beams. The limit of this language relies on the huge number of lines strictly linked each other, difficult to understand and manage for external users. An important year that has signed a great change in the code evolution is 1998. Indeed, during this year a new original code is developed, named Geant4. It is written in C++ language and it takes advantage from the object oriented software technology, which allows to write a clearer and more partitioned code.

Geant4 is currently developed by an international collaboration constituted approximately by one hundred members from Europe, US and Asia. Twice per year the collaboration updates the code, indeed the beta version is released on July and the final version on December [96].

The released Geant4 code consists of a kernel containing all the tools that the user has to include, according to the specific requirements of his own application. Moreover, the user must derive the concrete classes composing the application from the virtual and native classes included in the kernel. The object-oriented language allows the development of distinct classes according to the different aspects of a typical experiment, as for instance the geometry and material description, the source modelling, the physics processes and so

on. As all Monte Carlo radiation transport codes, Geant4 follows specific procedures of computation:

- definition of the requirements to be satisfied by the system to be modeled: this phase includes the description of the experimental setup in terms of geometry, objects, and the specification of the primary source characteristics, of the physical processes to be activated and of the kind of information to be retrieved from the simulation.
- randomly generate inputs according to the required source characteristics and perform computation: the primary particles are simulated one by one and tracked through the medium. Interactions and final states are randomly sampled according to the related probabilities. The primary particle and the possible secondary particles generated in the interaction are tracked until the kinetic energy goes down to zero.
- aggregate the results of the individual computations into the final results: the final analysis of the obtained data.

Till the Geant4 version 9.6, the code has been designed to work in a sequential mode and the simulation run was managed by one thread at a time. This can slow down the simulation, due to high computation time, especially when high statistics is required. In order to overcome computation time issues, from the Geant4 version 10.0, multi-threading has been implemented in the code and included in the official release. It consists in the event parallelism. i.e. each thread simulates one or more events independently and at the same time [97, 97]. Only the master thread controls the overall data flux, distributes the events to the workers threads, and provides the final results. The thread parallelism significantly accelerates the data processing, still guaranteeing affordable results. However, the possibility to run the simulation in the sequential mode is still maintained.

3.2 The ELIMED Geant4 application

The ELIMED beam line described in section 2.2.1, has been simulated in details using the Geant4 simulation toolkit [99, 100], which has been chosen for this purpose thanks to its robustness, versatility and reliability of the physical processes implemented. A specific application has been developed and it will be available for the users of the ELIMAIA beam line. In particular, the application, which has been delivered to ELI Beamlines in September 2017, was developed following four main requirements:

- Realistically reproduce the individual beam line element, in terms of geometry and magnetic features, maintaining a good flexibility of the code for user experimental setups
- Implement a realistic laser-driven ion source with specific energy and angular distribution
- Give the possibility to retrieve outputs at different positions along the beam line, including the final irradiation point
- Provide a easy-to-use and friendly interface of the code for end users

In order to fulfill all these requirements, the ELIMED application has been conceived as complex and modular code with an internal structure which can be simplified as shown in figure 3.1.

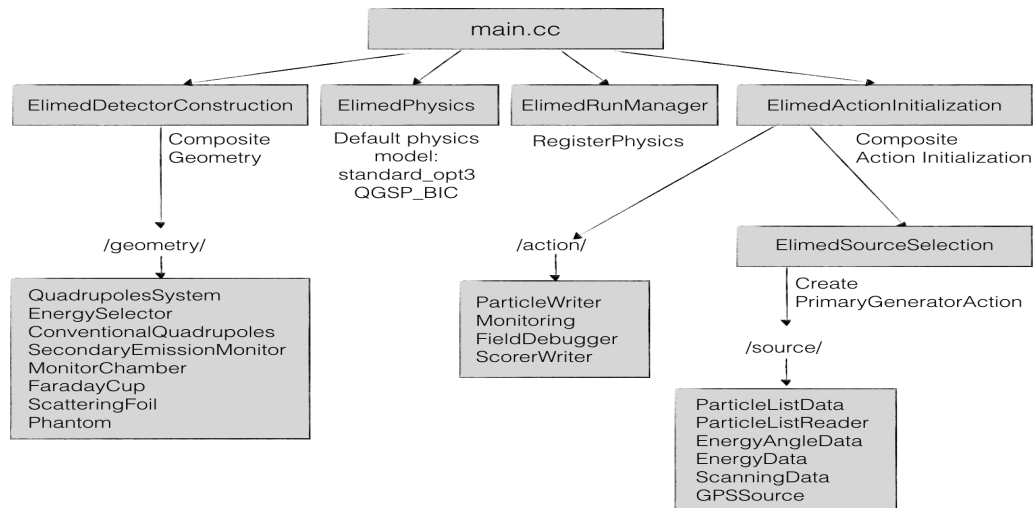


Figure 3.1: Structure of the ELIMED application.

As shown in figure 3.1, the code is organized in different modules:

- *Composite detector construction.* In order to easily switch off and on some elements of the beam line and to make them as much independent as possible, the classes `GeometryComponent` and `CompositeGeometry` have been implemented. They independently call each geometry component of the beam line, i.e. the Quadrupole system, the Energy Selector, the Faraday cup etc. just using macro commands.
- *Composite user actions.* In Geant4, it is not possible to include more than one instance of each optional user action class type. The `CompositeAction`, `ActionComponent` and `CompositeActionInitialization` provide a non-defined number of independent user actions.
- *Mapped fields.* There is no dedicated class in Geant4 able to load electromagnetic fields based on interpolated field maps in regular three-dimensional grids. Starting from the `purgingMagnet` example (included in the public Geant4 distribution) and generalizing it into a tool (`FieldMapManager` class), it has been possible to combine different (potentially overlapping) field maps (`VectorFieldMap` class) in a single field (`SummedField` class) with the possibility to change the strength and position at

runtime. This is a key feature of the application, because it gives the possibility to easily change the parameters of the magnetic elements according to the specific beam energy to be selected and transported. As a concrete loading interface, a reader for COMSOL [35] and OPERA [87] output files has been included in the application.

- *Particle properties.* Depending on the specific requirement, it could be worth retrieving information on kinematic properties of particles either *continuously* along their path through different components or discretely when crossing specific boundaries. For this purpose, the `ParticleWriter` class has been implemented, which gives the possibility to save particle properties, as the position, the energy and the momentum at each step or at any volume boundary, or even *virtual planes* along the beam-line, just using simple macro commands.
- *Phase space loading.* As already mentioned the application must be able to use as an input a realistic laser-driven ion source in order to realistically predict the beam transport for a bunch of accelerated particles. Different approaches have been developed at this aim (shown in next section), as the possibility to use a text file including the initial parameters of the accelerated particles, previously obtained with Particle In Cell (PIC) simulation or, alternatively during experiment. Moreover, this tool allows to reuse the particle properties registered at a specific location as an input for a second stage simulation in the remaining part of the beam line, drastically decreasing the computation time of the simulation. This functionality is implemented in the `PhaseSpaceSource` class.

3.2.1 Source implementation

In order to deliver a versatile tool, suitable for any user's requirement, the possibility to choose between different implementation approaches of the source has been provided according to the specific case study to be simulated:

- *General Particle Source.* Is one of the three native concrete `PrimaryGenerator` classes

included in the Geant4 kernel. It allows to produce a source with specified characteristics such as the spatial and energy distribution, the divergence and so on, just using macro commands. It is also possible to set the time and generate particle randomly on a surface or volume of specified shape.

- *EnergyAngle*. It is suitable when outputs from two-dimensional Particle-In-Cell (PIC) simulations are used as an input of the Geant4 simulation. Particle-In-Cell simulations deal with the interaction of the laser with certain characteristics with a specified target, solving the Vlasov equations of the particle motion in plasma. A typical output file of PIC-2D is composed of several lines, each one representing a simulated *macroparticle*, and two columns expressing the longitudinal and transversal momenta (p_z and p_y). From these parameters it is possible to retrieve the energy and the angular divergence (θ) of each particle and obtain the total energy and angular distribution. The energy spectrum and the energy as a function of the angle θ for protons simulated with PIC 2D code considering a nanosphere target have been provided by ELI Beamlines (figure 3.2).

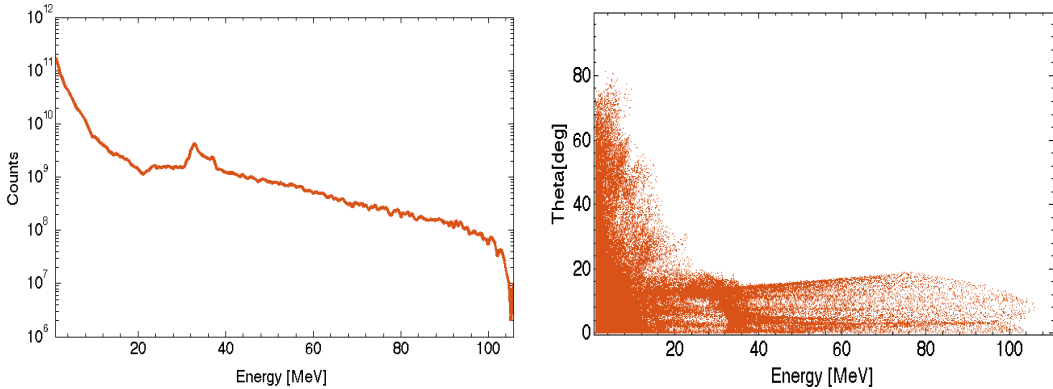


Figure 3.2: Energy distribution (left) and θ vs energy distribution (right) obtained with PIC 2D code simulating the interaction of a PW laser with a nanosphere target.

To correctly implement PIC source, assuring a good statistics, a two-level binning of the phase space file into 500 bins in energy and 50 bins $\cos \theta$ has been performed with

each of these 2D bins capturing the same fraction of the total number of particles. When creating particle for simulation, a random (equally probable) bin and the position inside the bin (uniform distribution) are chosen. The azimuthal angle was uniformly randomized in 2π .

- *ParticleList*. In this modality, a comma separated value (csv) file containing an header with the columns $px, py, pz, x, y, z, \text{ekin}, \text{pdg}$ is taken as input of the simulation. In order to increase the statistics, a different approach has been chosen with respect to PIC-2D source. Gaussian smearing in direction, position and kinetic energy is performed for any single particle contained in the input file. This enables to feed into the simulations as many particles as necessary while filling up the phase space smoothly. To show the achieved final result, figure 3.3 includes a subset of original particles (light blue) together with the ones (dark blue) obtained with Gaussian-smoothed distributions generated from the original particles, using a fixed standard deviation $\sigma=0.01$ mm.

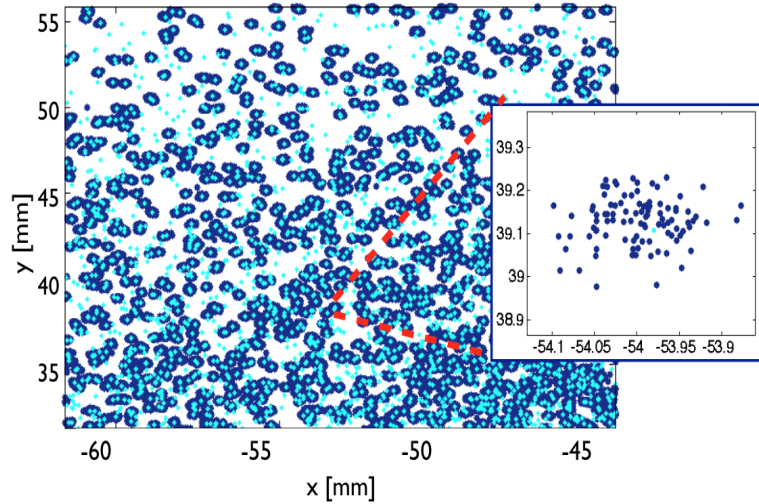


Figure 3.3: Positions in x-y plane (light blue) of original particles and positions generated using a random gaussian smearing on the original particles with $\sigma=0.01$ mm (dark blue).

The mentioned σ value for position, momentum and kinetic energy has been chosen

thanks to qualitative assessments, in order to obtain the best compromise between performing an effective smoothing and keeping the original spatial and kinetic information. In figure 3.4 the phase space obtained with different values of σ in px-py plane is reported, showing how the distribution changes by increasing the σ , almost losing the original information in the most extreme cases.

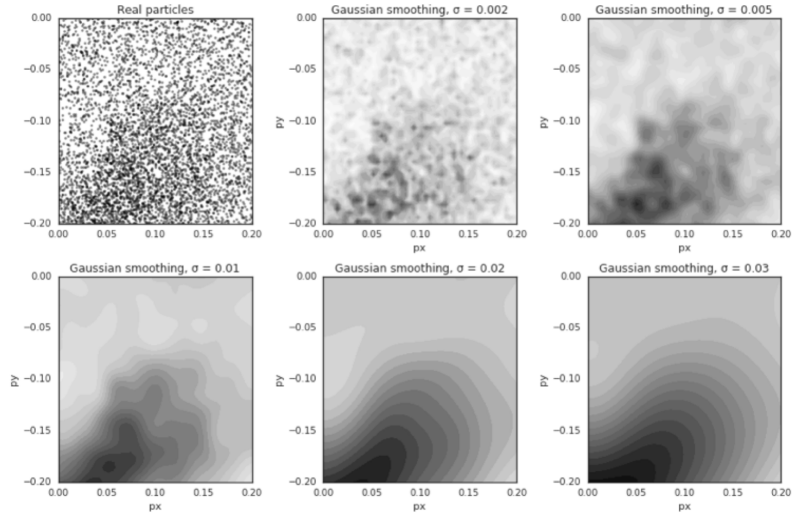


Figure 3.4: Example of the Gaussian smoothing used to enhance the statistically limited sample of source protons, in the px-py plane with different σ .

However, if necessary the parameter σ for position, momentum and kinetic energy random generation can be modified using macro commands. This modality has to be used when three-dimension Particle In Cell simulations (PIC3D) have to be employed as input of the Geant4 simulation.

3.2.2 Geometry components

The complete ELIMED beam line simulated with the Geant4 toolkit is shown in figure 3.5. As displayed, all elements composing the beam line are reproduced from geometric point of view considering their real sizes, materials and positions.

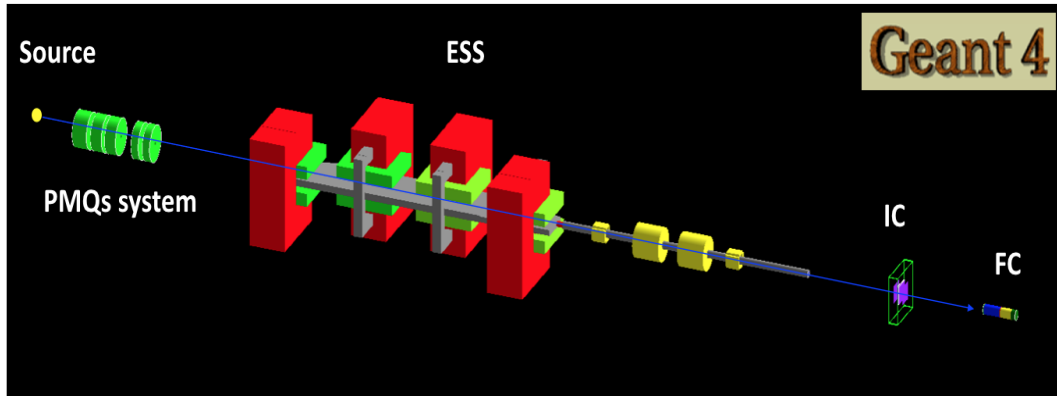


Figure 3.5: ELIMED transport and dosimetry beam line simulated with Geant4 simulation toolkit, from the source down to the irradiation point.

The details of each simulated element will be reported in next sections.

Quadrupole system

The first transport element, i.e. the focusing system, has been fully simulated with Geant4, implementing the final features in terms of geometry, dimension and magnetic field in order to realistically simulate particle transport. As described in section 2.2.2, the focusing system is composed of high-gradient permanent quadrupoles (PMQs), whose configuration is determined according to the particle species and energy to be transported. The application includes two different implementations of the PMQs geometry, which can be selected by user commands, according to the purpose of the simulation:

- a simplified model: the quadrupoles are simulated as simple iron cylinders with a 30 mm diameter bore and a length of 160 mm, 120 mm and 80 mm. The magnetic field maps are assigned to each magnet volume. This solution is more desirable when the purpose of the simulation is the transport optimization of primary beam along the whole beam line. The corresponding user command is: `/elimed/quadrupoles/simple`.
- a detailed model: a stainless shielding layer is added around the bore, the internal structure of the magnet composing of alternating aluminium and neodymium part is

included. This configuration should be used when the user is interested on secondary radiation production during the interaction of primary particles with the traversed materials. The corresponding user command is: `/elimed/quadrupoles/detailed`.

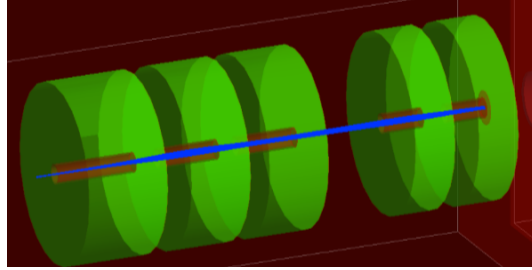


Figure 3.6: Simplified model of the quadrupole system simulated in the ELIMED application

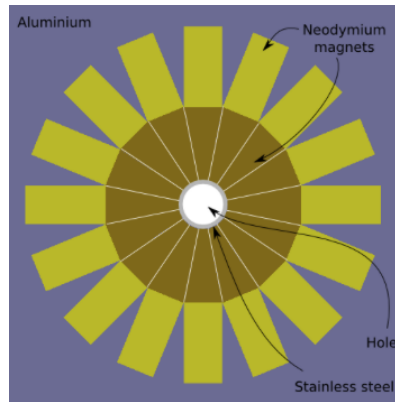


Figure 3.7: Section of the detailed model of the quadrupole simulated in the ELIMED application.

To realistically simulate the focusing effect and accurately implement the high gradients characterizing the field inside the PMQs, magnetic field maps obtained with the COMSOL and OPERA software for each quadrupole have been included in the application. Five 3D maps, with a step of 1 mm, corresponding to individual quadrupoles, were used in order to have a high spatial resolution grid allowing an accurate particle tracking. In order to evaluate the magnetic field values, a class dedicated to read and interpolate the map has

been implemented. Specifically, this class allows to import any field map from a CSV-like text file with magnetic field components, evaluated using trilinear interpolation. The correct implementation of the maps in Geant4 has been preliminarily verified evaluating the magnetic field components inside the quadrupoles at different positions. As an example, figure 3.8 shows all the three components (B_x , B_y and B_z) and the magnitude (B_{mod}) of the magnetic field in the middle plane at the center of the 160-mm quadrupole as a function of the distance along the radial axis (x). As expected, all the components decrease to zero at the quadrupole axis and the main contribution to the magnitude of the magnetic field is given by its transversal component (B_y).

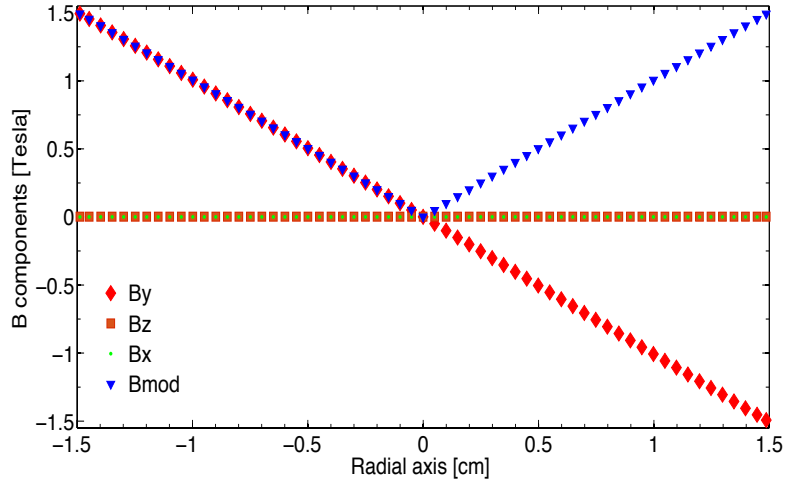


Figure 3.8: Magnetic field components along the x direction at the middle transversal plane of the 160 mm quadrupole

As a consequence, a high field gradient is present inside the quadrupole which makes the focusing of particles possible. The gradient dB_y/dx as a function of the radial direction x has been evaluated in order to calculate the maximum gradient value. It is shown in figure 3.9, together with the magnetic field gradient obtained with the COMSOL [35]. As it is shown, the maximum gradient value is -101 T/m in the case of negative gradient configuration for the 160-mm quadrupole, in agreement with the one obtained with the COMSOL software.

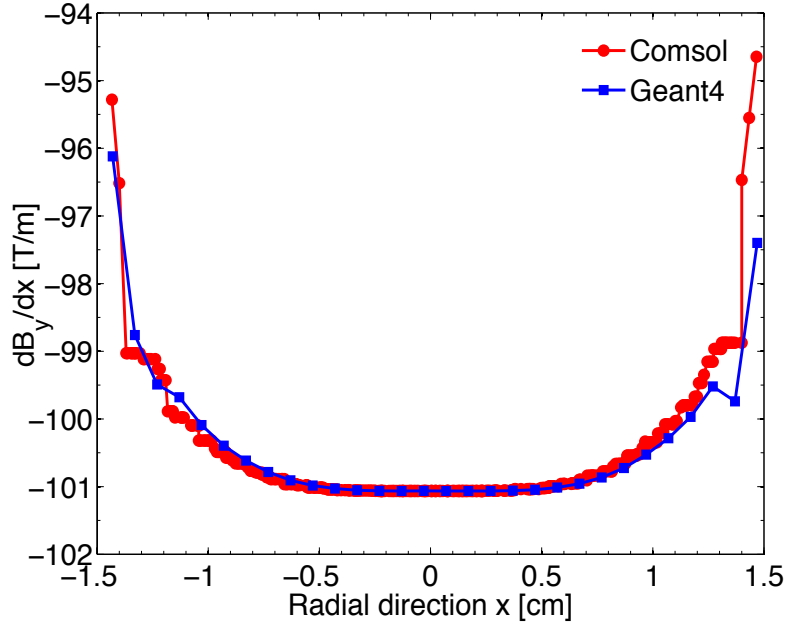


Figure 3.9: Magnetic field gradient at the center of the 160-mm quadrupole.

Moreover, the verification of the correct implementation of the fields with the consequent effect on particle tracking has been carried out, trying to evaluate the particle trajectory along the five magnetic fields and benchmarking the results with the SIMION software simulations. A specific configuration of the quadrupoles has been selected and reproduced in Geant4, based on the calculations done by COMSOL. The parameters related to the mentioned configuration, specifically designed to transport 60 MeV, are reported in table 3.1.

Quadrupole	Length [mm]	Gradient [T/m]	Relative PMQ distance [mm]
1	160	-101.06	49.55
2	120	+99.23	50
3	120	-99.23	178.72
4	80	+94.03	49.65
5	80	-94.03	

Table 3.1: Quadrupole length, gradient and relative distance used in the configuration for track benchmarking.

To verify the field map implementation, the proton tracks along the five quadrupoles were simulated for 4 different starting positions by storing spatial coordinates of all simulation steps. In all the considered cases, the beam was monoenergetic (60 MeV), parallel to the beam line axis; the starting point coordinates were: (3 mm,0,0); (-3 mm,0,0); (0,3 mm,0); and (0,-3 mm,0) respectively. In figure 3.10, a comparison of the trajectories obtained with Geant4 (red) and with the SIMION (blue) software is shown. As expected, there is a optimal matching of the tracks, demonstrating the reliability of the field map implementation in the Geant4 application used to simulate the PMQ system.

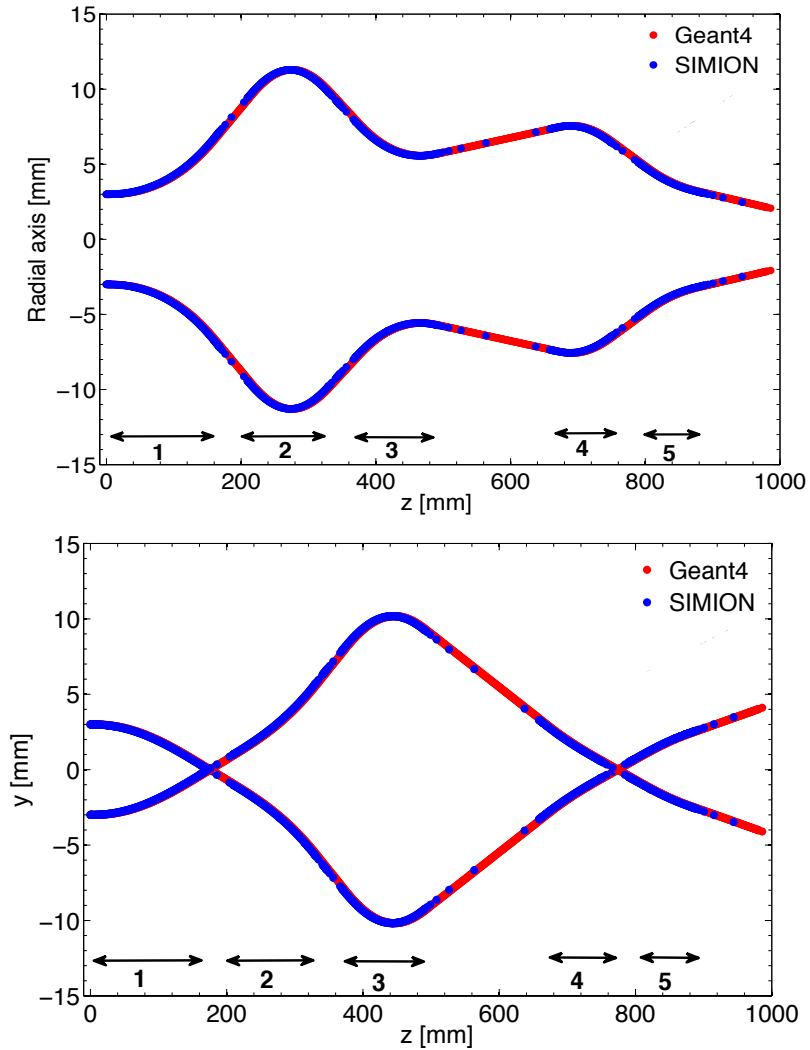


Figure 3.10: Comparison of the proton tracks simulated using SIMION (blue) and Geant4 (red) within the focusing system. The x-(in the upper plot) and y positions (in the lower plot) as a function of the distance along the beam axis are shown for starting positions of $x = \pm 3$ mm and $y = \pm 3$ mm respectively.

Energy selector system (ESS)

As described in section 2.10, the ESS consists of four resistive dipoles with alternating magnetic fields tunable from 0.17 up to 1.2 T, coupled with a central fixed slit, which is responsible for filtering out the particles of undesired energies. The energy selector system, including the in vacuum chamber, the magnets and the slit have been realistically

reproduced in details in Geant4, in terms of geometry, materials and magnetic field map as show in figure 3.11.

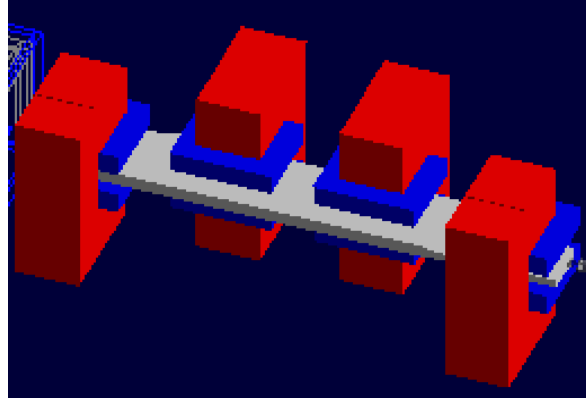


Figure 3.11: Screen shot of the Energy Selector System as implemented in the ELIMED application.

In the application it is possible to change at runtime the field intensity and slit width such to properly select the mean energy and energy spread of choice. Indeed, simply scaling the magnetic field values of the map, specific tracks will be deflected to go through the slit, depending on the particle species and their energy. The magnetic field map grid of any single dipole, provided by COMSOL software, has been imported in the simulation with proper polarity for all 4 dipoles. In order to account for field fringing, necessary to correct particle transportation at the edges, each map has a length of 900 mm along the beam z axis, which means 500 mm longer than the geometrical size of a single dipole, of 52 mm along the y axis and 100 mm along the x one. An overlapping region of about 500 mm length of the maps between the dipoles has been also realistically simulated, considering the sum of the magnetic field components in each point. The variation of the magnetic field By component along the beam direction is reported in figure 3.12 for the case of 60 MeV proton beam selection.

Similarly to PMQs system, in order to verify the correctness of magnetic field map implementation in Geant4, the variation of the magnetic field along the x direction has been evaluated, comparing it to the reference one, simulated with the COMSOL software. As

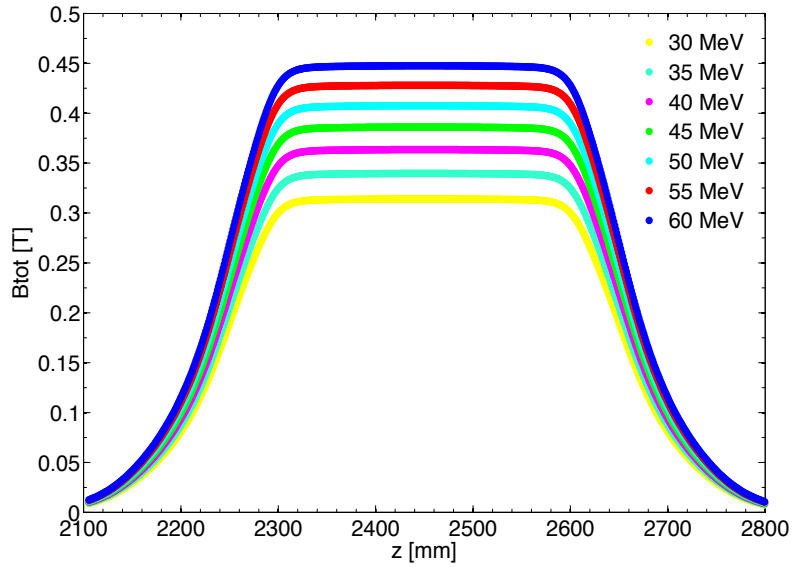


Figure 3.12: Magnetic field module for first dipole calculated with Geant4 along the beam axis for proton energy ranging from 30 MeV to 60 MeV.

it is shown in figure 3.13, there is an optimal agreement, demonstrated by a negligible non-uniformity of the magnetic field within the dipole gap of about 0.06 %.

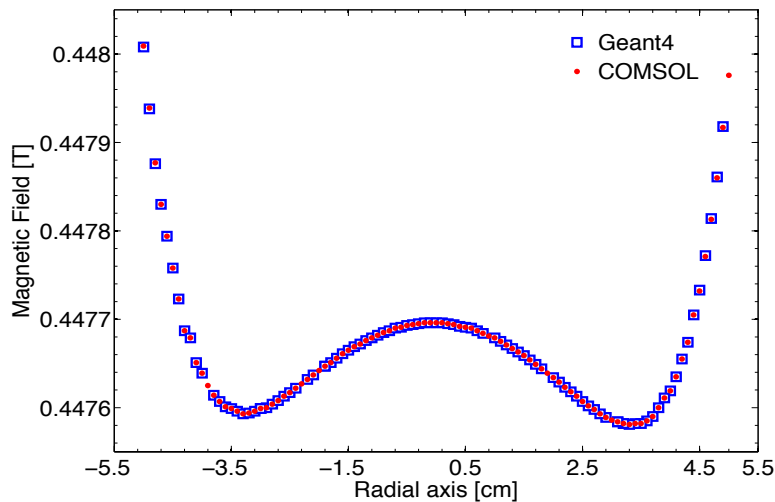


Figure 3.13: Magnetic field intensity along the x axis at the center of the dipole: comparison between Geant4 (blue) and COMSOL (red)

Moreover, the model was validated against the reference SIMION transport code, compar-

ing the trajectories of particles within the whole ESS. As for the quadrupoles, a 60-MeV proton track was simulated and tracked step by step within the ESS. In figure 3.14, the projection of the proton track in the xz plane is shown. Also in this case, the two trajectories overlap very well, demonstrating the correctness of the implementation.

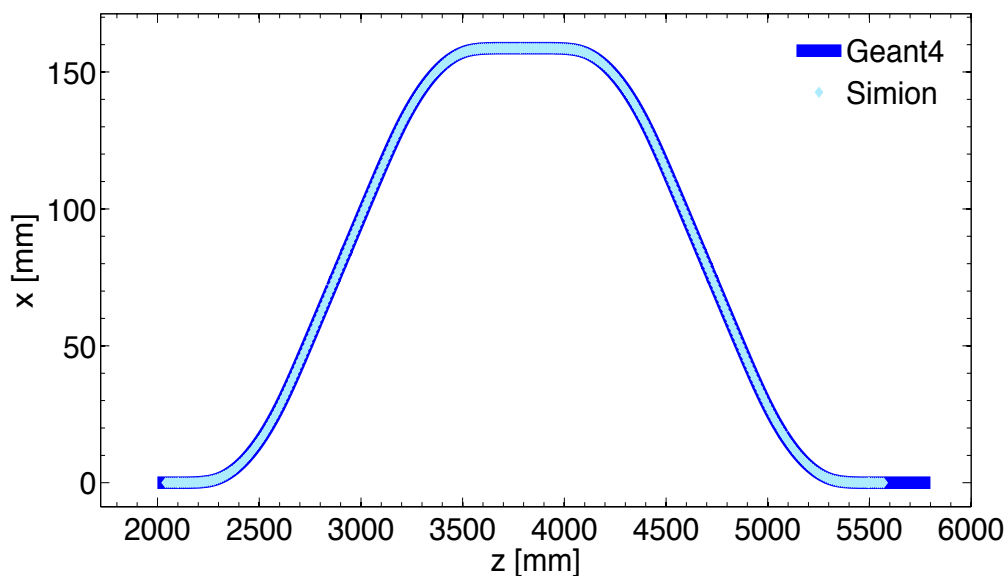


Figure 3.14: Comparison of the 60-MeV proton trajectories simulated by SIMION (light blue line) and Geant4 (blue line) along the ESS

Resistive quadrupoles and steerers

As previously shown, additional resistive quadrupoles and steerers which are located downstream the energy selector system in order to optimize the transport the focused and selected in energy particles down to the in-air final section. These elements have been also included in the ELIMED application, including their magnetic fields, in order to properly simulate the final beam shape and transmission at the end of the in-vacuum transport beam line.

Secondary Emission Monitor

The secondary emission monitor has been simulated as a simple cylindrical layer of tantalum (with its rotational axis along the beam line). The thickness of this layer was set to 20 μm , the radius to 4 cm (as starting values subject to possible future change). Neither support structure, nor the charge readout or actuator were included in the simulation. Due to infrared divergence of the electromagnetic processes, secondary production cuts are implemented in Geant4 to avoid huge computation times, as commonly used in most of particle tracking codes. Therefore, it is not possible to produce low-energy secondary electrons by proton ionization. Moreover, Geant4 also lacks description of free electron transport in metals, being a particle tracking code. Hence, acquired counts and properties of released secondary electrons have to be considered, only with an high-energy approximation. On the other hand, Geant4 simulations still provide realistic description of energy loss and deflection of protons in the volume. The response of the SEM to monoenergetic proton beams parallel to the beam-line axis for different energies from 5 to 60 MeV in 5-MeV steps was evaluated. The secondary production cut was set to the lowest recommended value (990 eV) and a maximum step length of 1 μm in the SEM was forced to provide good spatial resolution. Figure 3.15 shows the dependence of the mean number of electrons (with kinetic energy higher than 990 eV) on incident proton energy.

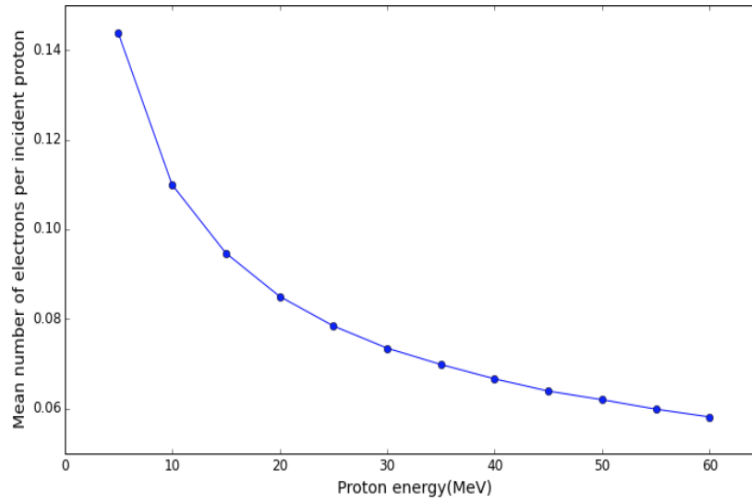


Figure 3.15: Mean number of electrons per incident proton escaping from the Secondary Emission Monitor as a function of the proton beam energy.

Monitor chambers

The monitor chamber has been reproduced as a box volume made of aluminium. It contains two cubic air-filled cavities (5 and 10 mm thick), that are separated from outside by a mylar window (20 μm thick) and a thin aluminium anode layer (1 μm thick). The central window separating the cavities is made of mylar and it is covered by a thin copper cathode on both sides. Support structures and readout are not included. In figure 3.16, a schematic view of the chamber is shown.

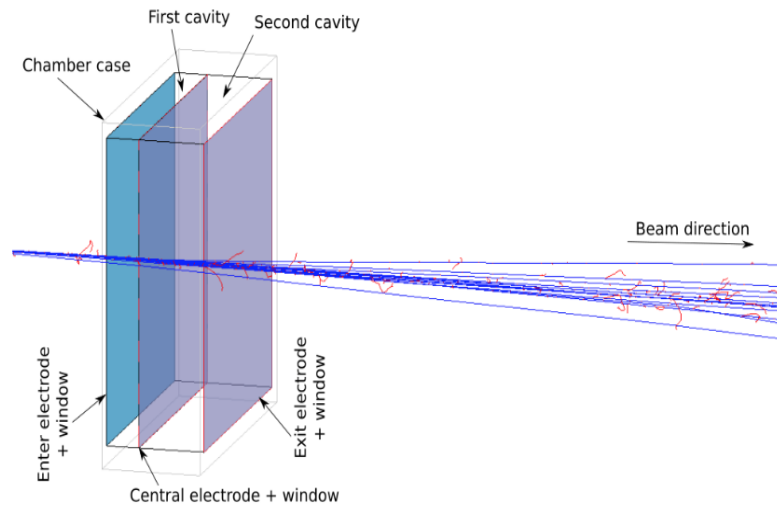


Figure 3.16: The model of monitor chamber with monoenergetic parallel incident beam of protons (blue) and daughter electrons (red)

Faraday Cup

The Faraday Cup for absolute dosimetry has been fully simulated (as shown in figure 3.17), in terms of dimensions, materials and electric field configuration.

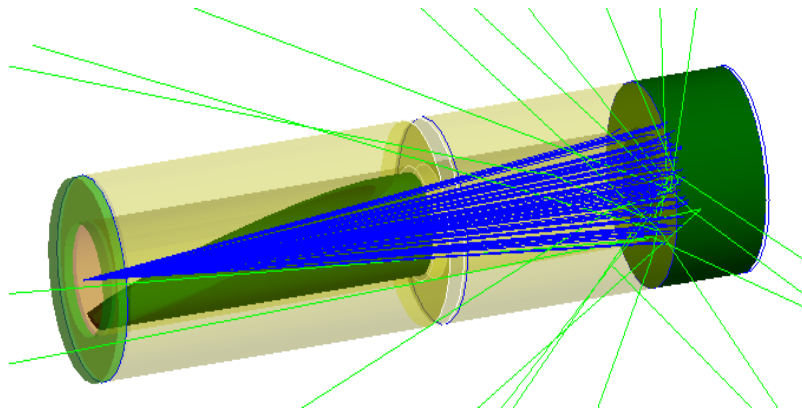


Figure 3.17: Visualization of the Faraday Cup implemented in Geant4 and the tracks of particles: primary protons (blue) and secondary neutral particles produced by the interaction with the cup material (green).

The geometrical model also includes the additional beveled electrode which, as mentioned in 2.2.5, creates an asymmetric electric field which is more efficient for secondary electron

suppression. As for magnetic field, the asymmetric electric field between the two electrodes is simulated using a map grid, with 1 mm of step obtained by COMSOL software, and implemented in the model using a dedicated class. The comparison between the electric field components along the axis sampled from Geant4 and from the reference code (COMSOL) as a function of position along the beam axis is shown in figure 3.18. The good agreement demonstrates, also in this case, the correct implementation in the Geant4 application of the electric field.

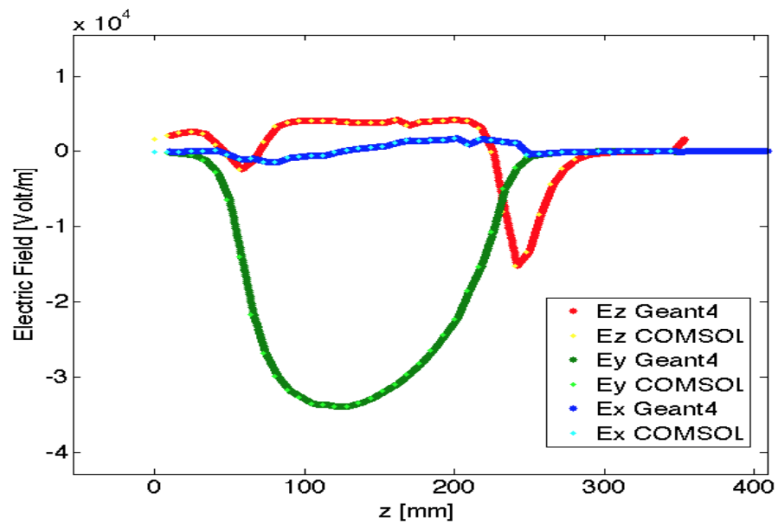


Figure 3.18: Comparison of the electric field components along the z axis (beam axis) obtained with the Geant4 toolkit and the COMSOL software

Moreover, in order to further validate the implementation, the tracking of the secondary electrons produced in the Faraday Cup and transported inside the implemented electric field has been verified: the tracks obtained in the Monte Carlo simulation have been compared with the tracks generated by the reference SIMION code. In figures 3.19 track projection in z - y plane is shown for an electron with an initial energy of 700 eV; the agreement between the two results is evident.

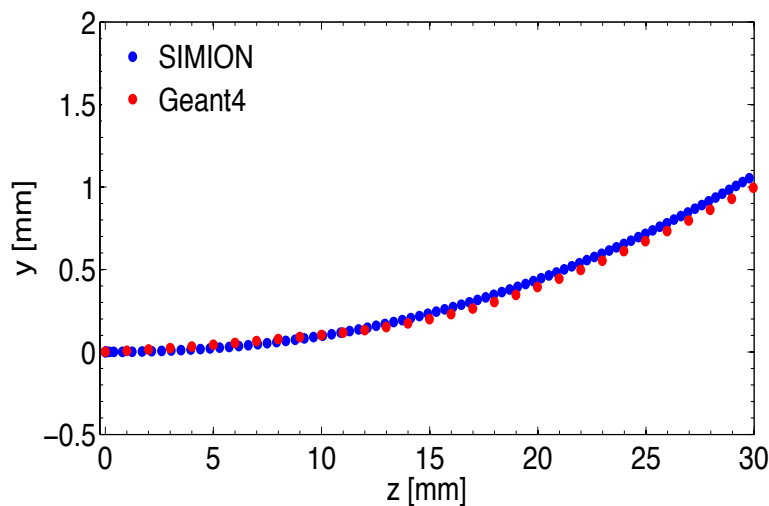


Figure 3.19: Comparison of 700-eV electron track projection in the zy plane, simulated by SIMION (red line) and Geant4 (blue points) within the Faraday cup electric field

3.3 Top-to-bottom simulations

Once the ELIMED application was validated and the whole beam line was successfully implemented, simulations from the source down to the in-air irradiation point have been performed, in order to study expected energy spectra, fluence and dose distributions per shot. These first results aim to demonstrate the reliability of the simulated model, which now can be used to predict the necessary information at the different endpoints in the ELIMAIA beam line. As an example, the results related to few selected configurations (low and high energy cases) will be reported, demonstrating the flexibility of the beam line.

3.3.1 In vacuum transport and energy selection

Since no experimental data are still available for the ELIMAIA beam line until the laser will start to operate, Particle In Cell simulations have been used as input of the Geant4 simulations in order to provide realistic outputs, as it is explained in section 3.2.1. In particular, two dimensional PIC simulations have been performed, reproducing the inter-

action of 1 PW laser and a thin nanosphere target. The energy spectrum and the angle vs energy dependence are reported in figure 3.2 of section 3.2.1. The implementation of the source in the code follows the *EnergyAngle* method as explained in section 3.2.1. In particular, the file used as input of Geant4 simulation includes $4.46 \cdot 10^5$ lines, each one representing a *macroparticle*, i.e. $2 \cdot 10^6$ real generated particles. Considering this, the total number of protons simulated per shot is $8.88 \cdot 10^{11}$. Beam energy spectrum and shapes in different transversal planes have been retrieved for specific energy configurations of both the quadrupole system and the energy selector. In figures 3.20 and 3.21 the proton energy spectrum and beam shape respectively for 5 MeV and 60 MeV quadrupole configuration, obtained just after the quadrupoles are reported.

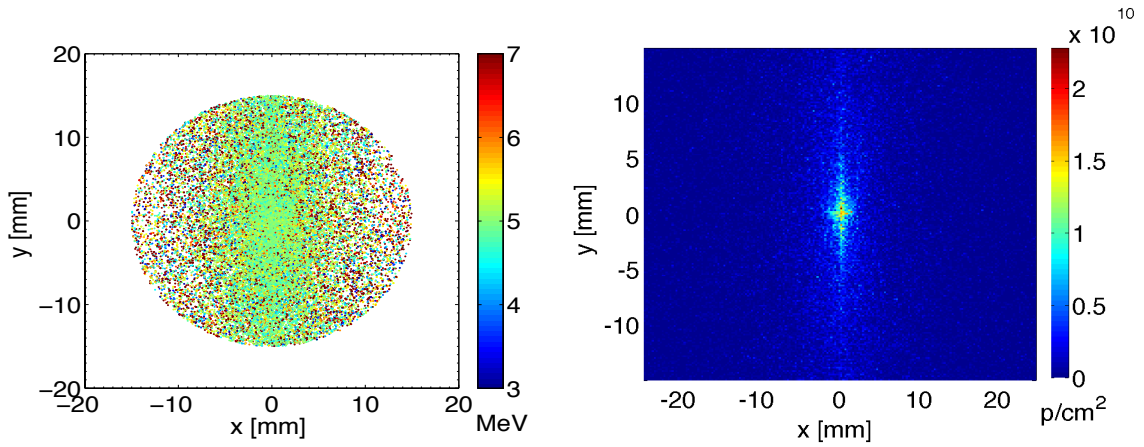


Figure 3.20: Left: Beam energy distribution after the 1st collimator placed between the PMQs and the ESS, with PMQs arranged for 5 MeV proton selection. Color bar is referred to proton energy in MeV. Right: Beam fluence distribution before ESS for the same configuration.

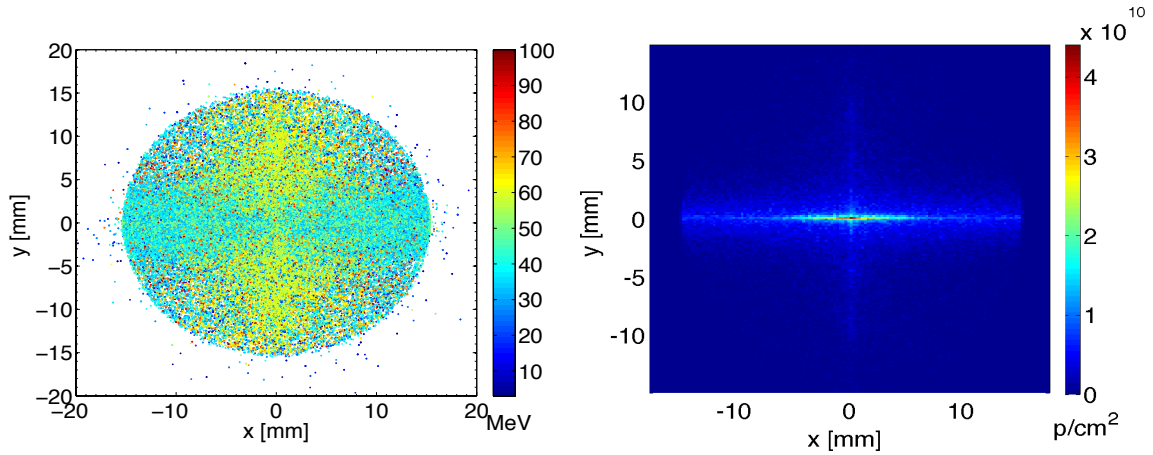


Figure 3.21: Left: Beam energy distribution after the 1st collimator placed between the PMQs and the ESS, with PMQs arranged for 60 MeV proton selection. Color bar is referred to proton energy in MeV. Right: Beam fluence distribution before ESS for the same configuration.

As clearly visible, downstream the PMQs system, for both the two energy configurations, the beam has still other energy components, which will be finally selected with the ESS. The focusing effect of the PMQs results, instead, in a reduction of the angular divergence of protons characterized by the specific energy to be transported. Figure 3.22 shows the angular distribution of protons with an energy of 60 ± 6 MeV after the quadrupoles. The angular spectrum is peaked at 0.1° , demonstrating the focusing effect of quadrupole system to inject the desired energy component in the ESS.

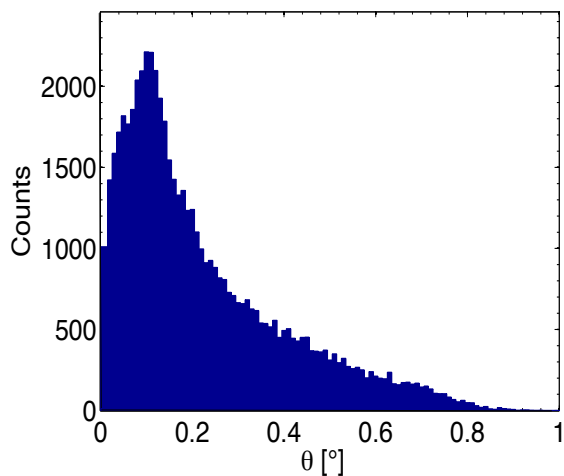


Figure 3.22: Angular distribution (θ) of protons in the energy range 60 ± 6 MeV after the quadrupole system.

As already mentioned, depending on the configuration of quadrupoles and the energy selector system (field strength, slit opening width), different parts of the energy spectra are selected. Figure 3.23 shows the energy spectra obtained just after the ESS for different configurations, fixing the slit aperture to 10 mm.

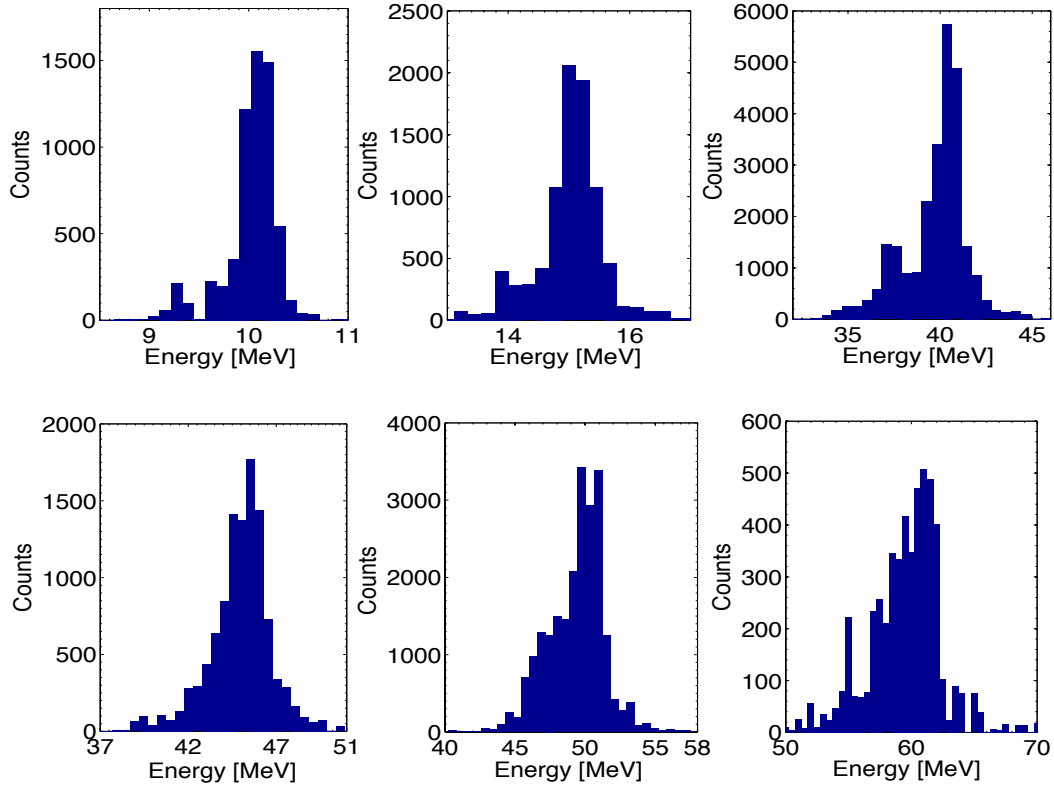


Figure 3.23: Energy spectrum obtained at the ESS exit, using PMQ and ESS configuration to select respectively 10 MeV, 15 MeV, 40 MeV, 45 MeV, 50 MeV and 60 MeV fixing the slit aperture to 10 mm.

Nevertheless, as already shown, the slit width plays an important role on the beam characteristics at the end of the ESS, in terms of energy spread and transmission. For these reasons a dedicated study for the energy spectrum as well as for the transmission efficiency as a function of the slit width has been carried on in order to find the best configuration. In particular, the energy spectra were retrieved after the kapton window at the end of the in-vacuum beam line section (after resistive PMQs and steerer), with all magnetic fields (i.e. in first quadrupoles, in the energy selector and in the final section) configured to transport 5 MeV and 60 MeV protons and considering a slit width of 5 mm, 10 mm and 20 mm (figure 3.24 and 3.25).

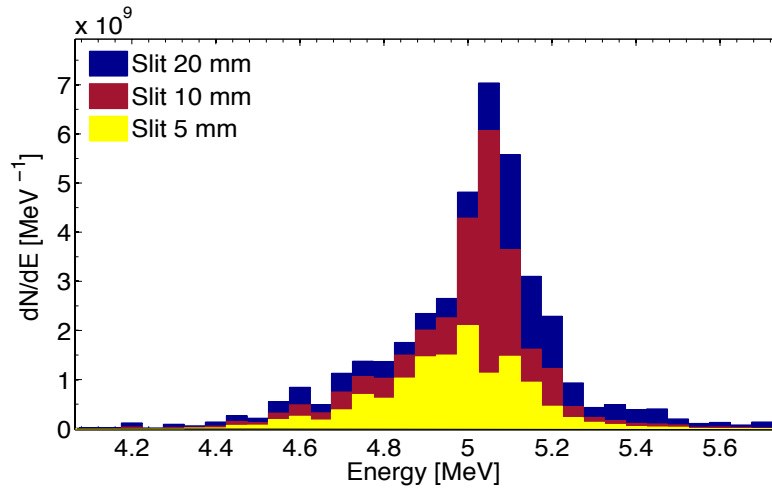


Figure 3.24: Energy spectrum for 5 MeV proton configuration, just after the ESS with a 20 mm (blue), 10 mm (red) and 5 mm (yellow) slit aperture. The counts reported have been normalized on the total number of protons produced at the source point, obtained with the PIC-2D simulation.

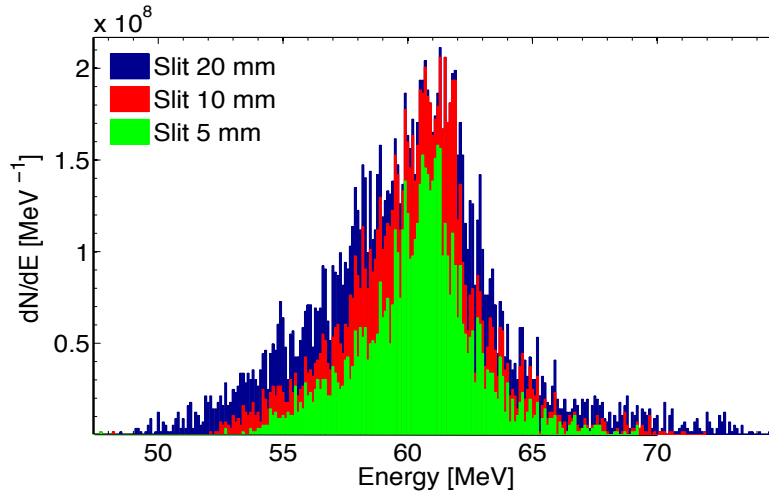


Figure 3.25: Energy spectrum just for 60 MeV proton configuration after the kapton window of the in-vacuum section with a 20 mm (blue), 10 mm (red) and 5 mm (green) slit aperture. The counts reported have been normalized on the total number of protons produced at the source point, obtained with the PIC-2D simulation.

The FWHM and the energy resolution (in %) have been obtained fitting with a Gaussian curve the energy spectra for both energy configurations and the results are reported in

table 3.2 and 3.3.

Slit width [mm]	FWHM [MeV]	Energy spread %
5	0.33	6.6 %
10	0.21	4.3 %
20	0.25	5 %

Table 3.2: FWHM and energy spread for 5 MeV proton beams, considering three different slit widths

Slit width [mm]	FWHM [MeV]	Energy spread %
5	4.14	7 %
10	4.74	8 %
20	6.89	11 %

Table 3.3: FWHM and energy spread for 60 MeV proton beams, considering three different slit widths.

As expected, a smaller slit width results in a smaller energy spread after the ESS, which may be desirable for some applications. Nevertheless, decreasing the slit aperture, also the transmission decreases resulting in a reduced dose delivered per shot. In order to quantify the dependence of particle transmission from the slit aperture for the two energy configurations chosen (5 MeV and 60 MeV) table 3.4 and 3.5 report the calculation of the transmission efficiency considering respectively protons with an energy of 5 ± 0.25 MeV (10 %) and 60 ± 6 MeV (20 %). The second column of both the tables reports the number of protons within the considered energy range at the source point (from PIC 2D), while the third one is the number of protons retrieved at the end of the in vacuum beam line for the same the energy range. Finally the transmission efficiency is calculated as the ratio between these two numbers.

Slit width [mm]	Input [5 ± 0.25 MeV]	Output [60 ± 0.25 MeV]	Transmission %
5	$2.76 \cdot 10^{10}$	$5.68 \cdot 10^8$	2.06 %
10	$2.76 \cdot 10^{10}$	$1.23 \cdot 10^9$	4.47 %
20	$2.76 \cdot 10^{10}$	$1.62 \cdot 10^9$	5.86 %

Table 3.4: Transmission efficiency values obtained for 5 MeV proton beams respectively selected with different slit apertures.

Slit width [mm]	Input [60 ± 6 MeV]	Output [60 ± 6 MeV]	Transmission efficiency %
5	$1.22 \cdot 10^{10}$	$5.99 \cdot 10^8$	4.9 %
10	$1.22 \cdot 10^{10}$	$9.75 \cdot 10^8$	7.99 %
20	$1.22 \cdot 10^{10}$	$1.2 \cdot 10^9$	9.86 %

Table 3.5: Transmission efficiency values obtained for 60 MeV proton beams respectively selected with different slit apertures.

The transmission efficiency of the whole transport beam line results quite good, also for 60 MeV proton selection, where it is ranging between 5% and 10%.

3.3.2 Dose delivery: transversal and longitudinal beam profile

The total number of protons reaching the in-air final section and their spatial distribution, in both 5 MeV and 60 MeV configurations, is strictly connected with the dose distribution obtained at the irradiation point for each shot. In this section, transversal and the longitudinal dose distributions predicted at the ELIMAIA beam line are presented. The results are reported for the two mentioned energies, as in the previous section, and for 20 mm, 10 mm and 5 mm slit aperture.

As typically done in conventional dosimetry, the dose released in water has been evaluated, including in the geometrical configuration, a $1 \times 1 \times 6$ cm^3 water phantom just after the kapton window in the in-air section. The dose deposited in water as a function of the depth, i.e. the Bragg Peak, was recorded using the primitive Geant4 scorer. Slices of $1 \mu m$

thickness (for 5 MeV) and of 50 μm thickness (for 60 MeV) have been used in order to reproduce with an acceptable spatial resolution the depth dose distributions.

In figure 3.26 and 3.27, the Bragg Peak for the three slit configurations and, respectively for both 5 and 60 MeV energy selection are shown. The dose has been calculated normalizing the results to the total number of protons produced per shot, according to the PIC 2D simulations.

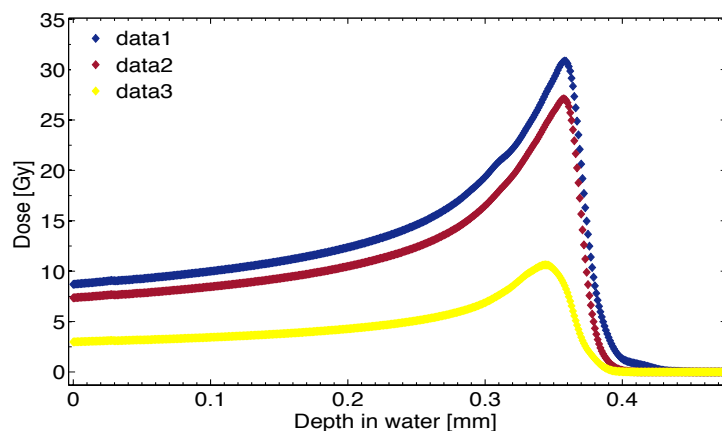


Figure 3.26: Dose-depth profile in water (Bragg Peak) of 5-MeV proton beam obtained in a water phantom placed just after the kapton window with 20 mm (blue), 10 mm (red) and 5 mm (yellow) slit aperture.

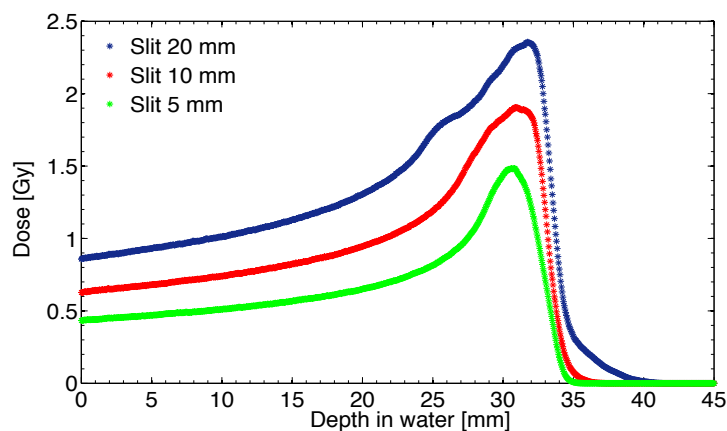


Figure 3.27: Dose-depth profile in water (Bragg Peak) of 60-MeV proton beam obtained in a water phantom placed just after the kapton window with 20 mm (blue), 10 mm (red) and 5 mm (green) slit aperture.

As it is shown in figures 3.26 and 3.27, the slit aperture determines the properties of the longitudinal profile in water, in terms of peak-plateau ratio, practical range and distal dose fall-off. These quantities have been calculated for the three configurations and for 60 MeV and 5 MeV (table 3.6 and 3.7)

Slit width [mm]	Peak-Plateau ratio	Practical range [mm]	Distal dose fall-off [mm]
5	3.49	0.392	0.028
10	3.66	0.393	0.019
20	3.54	0.391	0.026

Table 3.6: Peak-Plateau ratio, practical range and distal dose fall-off values related to figure 3.26 (5 MeV protons).

Slit width [mm]	Peak-Plateau ratio	Practical range [mm]	Distal dose fall-off [mm]
5	3.41	34	2.3
10	3	34.42	1.95
20	2.73	35.75	3

Table 3.7: Peak-Plateau ratio, practical range and distal dose fall-off values related to figure 3.27 (60 MeV protons).

The dose transversal distributions after the kapton window have been also evaluated. Those numbers are directly connected with the transversal dose distributions per shot at the sample irradiation point and can provide the first preliminary predictions useful for future multidisciplinary experiments. Similarly to before, the dose delivered in water has been evaluated placing a water phantom just after the kapton window and a scorer with the following dimension: $5 \times 5 \times 1 \text{ cm}^3$. A single slice in depth was used, while $500 \mu\text{m} \times 500 \mu\text{m}$ voxel size in transversal plane have been chosen in order to obtain a reliable spatial resolution. In the figures 3.28 and 3.29 the 2D dose distributions in the transversal plane and the correspondent X and Y profiles at the center of the beam spot for 5 MeV and 60 MeV, fixing 10 mm of slit aperture, are shown.

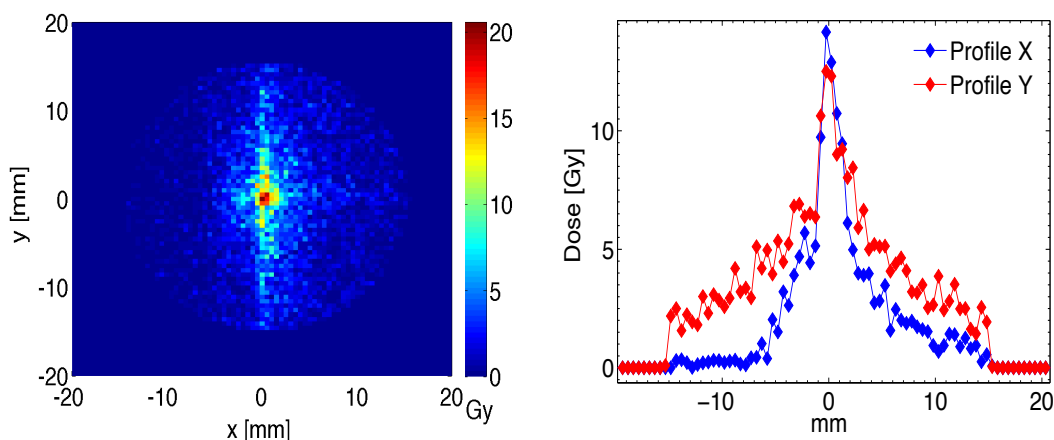


Figure 3.28: Spatial transversal dose distribution for 10 mm slit aperture and 5 MeV proton selection retrieved after kapton window (left). X and Y profiles at the center of the beam spot (right).

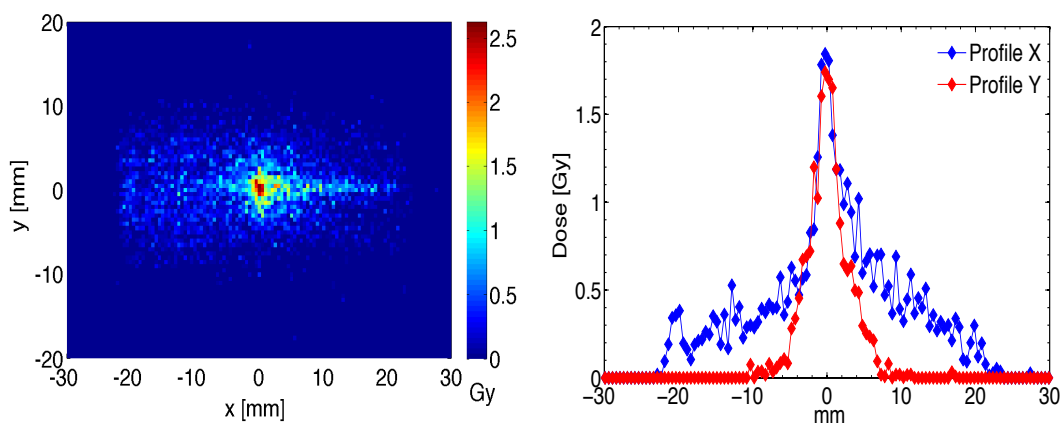


Figure 3.29: Spatial transversal dose distribution for 10 mm slit aperture and 60 MeV proton selection retrieved after kapton window (left). X and Y profiles at the center of the beam spot (right).

The results are quite far from a typical flat profile, which could be wished for multidisciplinary applications like cell sample irradiations. In order to improve the beam homogeneity also in the perspective of such kind of experiments, dedicated studies have been performed on the possibility to implement, in the in-air section, passive beam shaping elements. However, the results shown provide preliminary useful information about the

expected dose distribution per shot at the sample irradiation point, using as input realistic PIC data provided by the ELI group.

3.3.3 Optimization in air of the transversal 60 MeV proton beam profile

Starting from the output beam at the kapton window shown in figure 3.29, the in-air transport of the beam has been simulated in the final section of the ELIMED-beam line, and a transport optimization has been attempted in the case of 60 MeV proton transport. Since the transversal profile at the exit of the in vacuum beam line shown in figure 3.29 is not sufficiently flat and homogeneous as required by some multidisciplinary applications, like the medical ones, different passive elements able to spread the beam, increasing the beam uniformity, have been tested in the simulation. On the other hand, the use of passive elements as scattering foils as well as the air itself, typically decreases the particle fluence and dose and affect the energy spread and loss, therefore the most appropriate passive element thickness and material has to be chosen. For this purpose, three cases have been considered in the simulation to compare the results in terms of profile uniformity as well as energy spread, energy loss and final delivered dose:

- 2 m of air: the transversal and longitudinal beam profiles were evaluated at 2 m of air far from kapton window
- 100 μm thick Tantalum scattering foil and 2 m of air. It is placed 20 cm from kapton window and the profiles were retrieved still at 2 m from kapton window.
- 300 μm thick Tantalum scattering foil and 2 m of air. As before, it is placed 20 cm from kapton window and the profile again retrieved at a total distance from kapton window of 2 m.

The geometrical configuration used in the in-air simulations is shown in the scheme reported in figure 3.30.

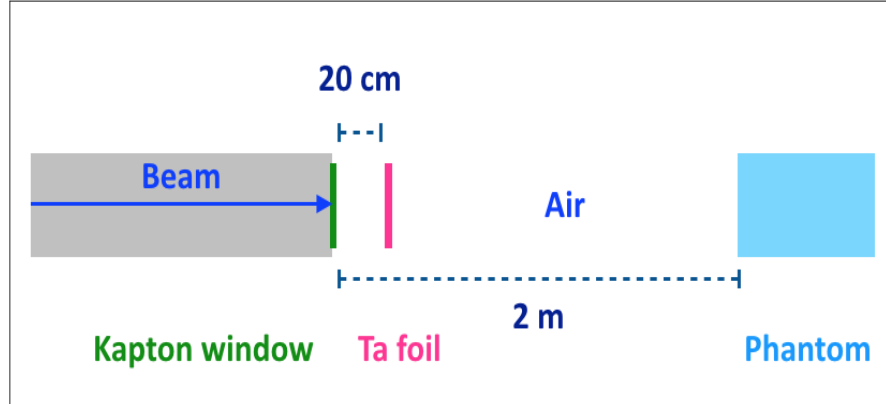


Figure 3.30: Layout of the simulation setup.

For all configurations, the slit width was fixed to 10 mm.

Figure 3.31 shows the energy spectrum retrieved at the entrance of the water phantom and the corresponding depth-dose profile in water for the three simulated cases. In particular a $1 \times 1 \times 6 \text{ cm}^3$ scorer with $100 \mu\text{m}$ as step was used to extract the Bragg Peak profile.

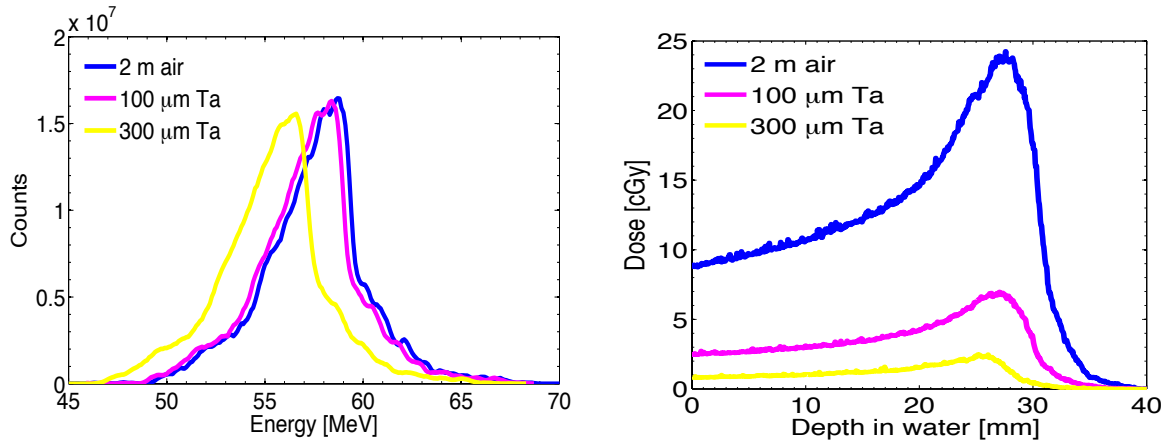


Figure 3.31: Energy spectra a) and Bragg Peaks b) retrieved on the water phantom placed at 2 m from kapton window in the three geometrical configurations chosen: 2 m air (blue line), $100 \mu\text{m}$ Ta (magenta line) and $300 \mu\text{m}$ Ta (yellow line).

Table 3.8 and 3.9 list the details on the obtained energy spectra and Bragg peak, in terms of peak-plateau ratio and dose delivered per shot at the entrance and on the peak. As expected, increasing the thickness of the scattering foil, the dose delivered per shot

decreases down to few cGy/shot for 300 μm thickness, due to the scattering of protons on the foil.

Configuration	Energy [MeV]	FWHM [MeV]	Resolution
2 m Air	58	5 MeV	9 %
100 μm Ta	57.8	5 MeV	8.7 %
300 μm Ta	56.3	5.15 MeV	9.15 %

Table 3.8: Energy, FWHM and resolution for the energy spectra shown in figure 3.31

Configuration	Peak-plateau ratio	Dose at the entrance [cGy]	Dose on the peak [cGy]
2 m Air	2.69	8.7	24.2
100 μm Ta	2.79	2.5	6.9
300 μm Ta	2.6	0.86	2.35

Table 3.9: Peak-plateau ratio and dose delivered in water at the entrance and on the peak for the three configurations related to figure 3.31.

On the other hand, the beam spot and the transversal X and Y profile obtained on the water phantom are considerably improved, as shown in figure 3.32, 3.33, 3.34. In such case a $20 \times 20 \times 0.1 \text{ cm}^3$ scorer was used, with $500 \mu\text{m} \times 500 \mu\text{m}$ voxels.

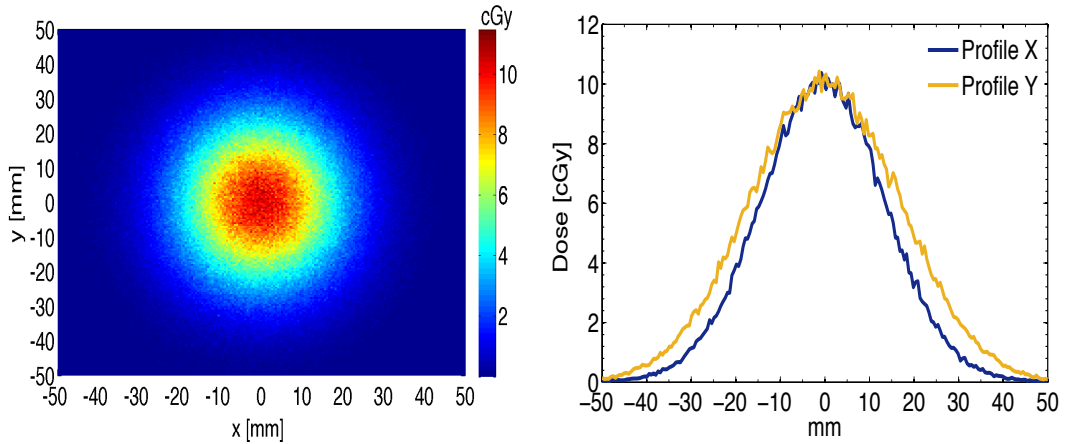


Figure 3.32: Spatial transversal dose distribution obtained at 2 m from kapton window (a) and corresponding central X and Y profiles (b).

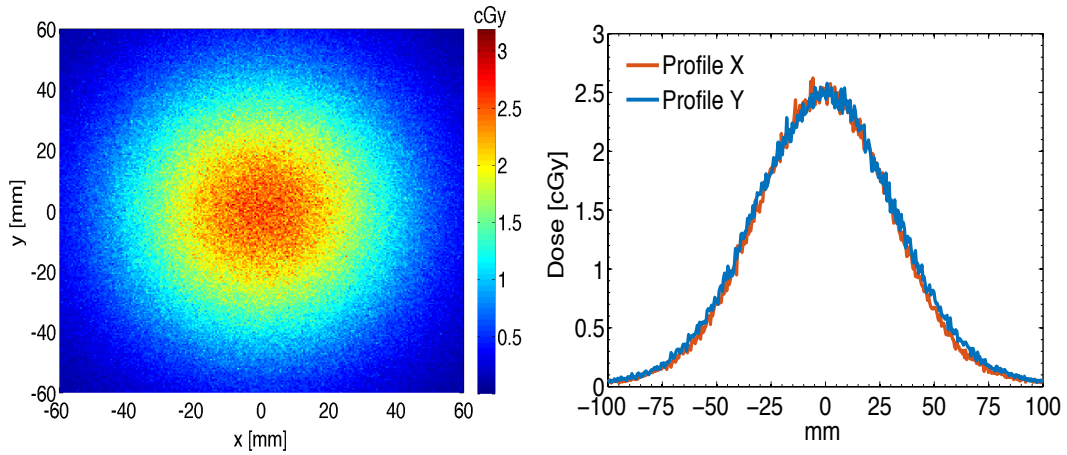


Figure 3.33: Spatial transversal dose distribution obtained at 2 m from kapton window after $100\ \mu\text{m}$ Ta scattering foil (a) and corresponding central X and Y profiles (b).

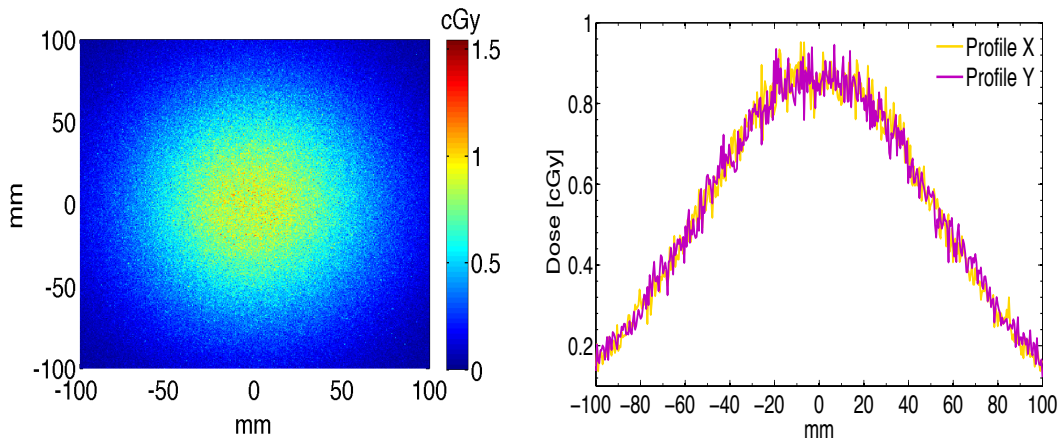


Figure 3.34: Spatial transversal dose distribution obtained at 2 m from kapton window after $300\ \mu\text{m}$ Ta scattering foil (a) and corresponding central X and Y profiles (b).

Looking at the effect of air and absorber foils on the transversal profile, it is clear that a larger thickness results in a higher broadening of the beam and as a consequence, in an improved homogeneity of the beam profile in a larger area (table 3.10).

Configuration	Beam spot diameter [mm]	Flatness (10 %)
2 m Air	32.3	$\Phi : 5mm$
100 μ m Ta	71.6	$\Phi : 14mm$
300 μ m Ta	130	$\Phi : 20mm$

Table 3.10: Beam spot diameter (at 50 % of the normalized profile) retrieved on the water phantom surface and diameter corresponding to a flat profile (10 %) for the three setups.

For both the configurations implementing a scattering foil, a collimator was also simulated in the geometry following the scheme reported in Fig. 3.35. As shown, a brass 10 mm thick collimator was placed 10 cm far from water phantom with a diameter of 10 mm and 20 mm respectively for 100 μ m and 300 μ m thick Ta.

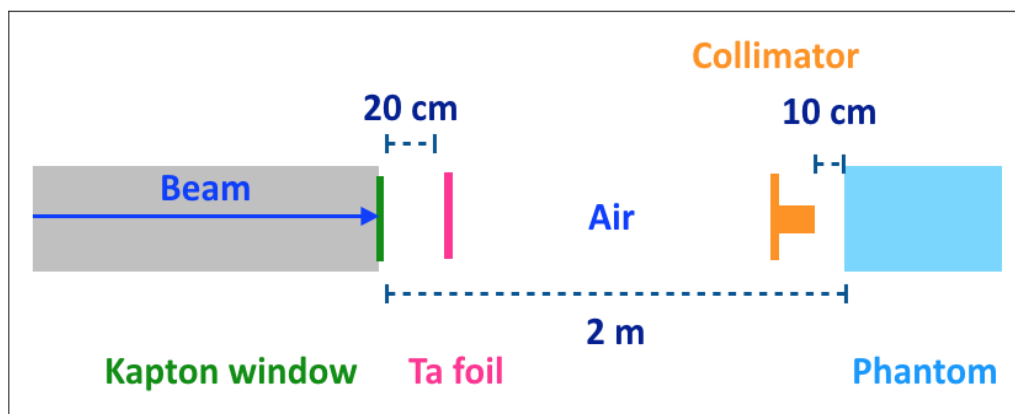


Figure 3.35: Layout of the simulation setup with the add of the brass collimator.

The beam spots and profile shown in figure 3.36 and 3.37, finally looks much closer to a typical flat profile used for multidisciplinary applications. In such way, the dose is uniformly delivered on the entire exposed surface, as required, for instance, by cell sample irradiations.

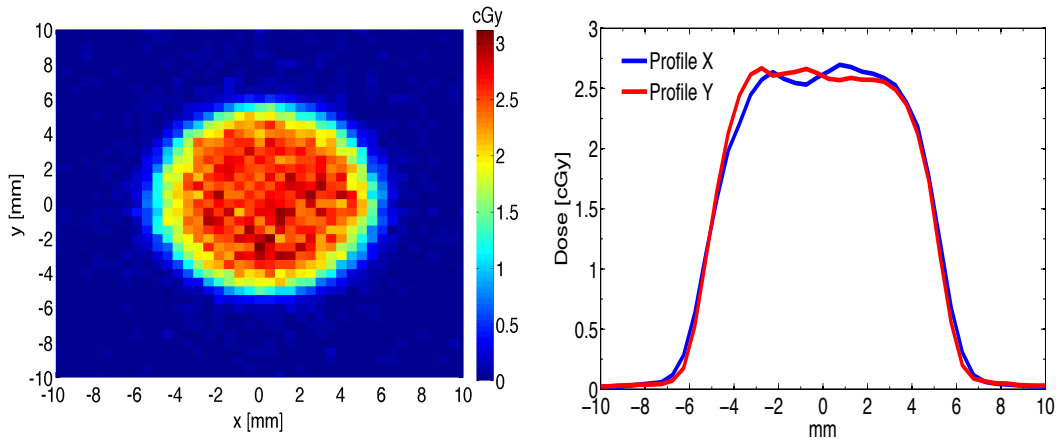


Figure 3.36: Spatial transversal dose distribution obtained at 2 m from kapton window after $100\ \mu\text{m}$ Ta scattering foil and a 10 mm diameter brass collimator (a) and corresponding central X and Y profiles (b).

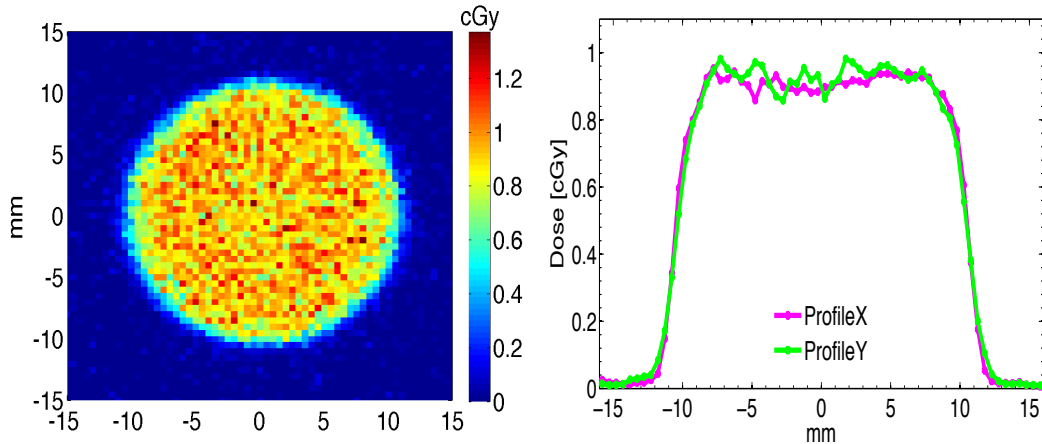


Figure 3.37: Spatial transversal dose distribution obtained at 2 m from kapton window after a $300\ \mu\text{m}$ Ta scattering foil and a 20 mm diameter brass collimator (a) and corresponding central X and Y profiles (b).

As regards the transversal profiles, the best configuration for the beam homogeneity is provided, as expected, by the one with the thicker scattering foil. Nevertheless, a compromise between the profile homogeneity and the dose delivered per shot must be achieved to assure a *good* profile maintaining an acceptable energy spread and especially a reasonable dose delivered per shot. A high dose per pulse ensures, indeed, feasible irradiation times,

providing total doses typically used for applications.

To give an example, considering the realistic repetition rate of the L3 laser delivered at the ELIMAIA experimental hall of 1 Hz, the dose rate in Gy/min (which means for a total of 60 shots) was estimated for each of the simulated in air transport configurations as reported in table 3.11.

Configuration	Dose-rate at the entrance	Dose-rate on the peak
2 m Air	5 Gy/min	14.4 Gy/min
100 μ m Ta	1.5 Gy/min	4.14 Gy/min
300 μ m Ta	0.5 Gy/min	1.41 Gy/min

Table 3.11: Dose-rate evaluated for the three simulated configurations at the entrance and on the peak

The results discussed above are of great importance to demonstrate the feasibility of using laser driven beams for multidisciplinary applications. Moreover, they demonstrate that, according to the laser parameters at ELIMAIA, the ELIMED beam line will be able to transport beams suitable to such applications.

3.4 Energy modulation with the ESS for longitudinal dose distribution of clinical interest

As mentioned before, one of the possible applications of laser-driven proton beams is the medical one, which means studying in a future perspective the use of laser-driven protons for therapeutic purposes. As it is well known, the use of energetic protons for cancer treatments, accelerated by cyclotrons or synchrotrons, offers numerous advantages with respect to conventional radiotherapy with photons, providing an highly localized dose in the target, sparing the healthy tissues. Nevertheless, the FWHM typical of a mono-energetic Bragg Peak in the energy range 60-200 MeV, of the order of few millimeters, is not sufficient to covers the total tumour width in longitudinal direction. To achieve

flat and extended longitudinal dose distribution able to properly cover the tumour target with a constant dose, a *Spread Out Bragg Peak* (SOBP) has to be used, consisting on the convolution of several pristine peaks corresponding to different proton energies and penetration depths (ranges).

Nowadays, two methods are available to longitudinally spread the pristine peak and obtain an homogeneous dose on the whole tumor thickness:

- *Passive scattering* in which the pristine peak is spread out longitudinally through the use of plastic passive absorbers of variable thickness. In this approach the SOBP is obtained typically using a range modulator wheel, consisting of a rotating wheel composed of different PMMA thicknesses.
- *Active scanning*, in which pencil beams accelerated with different energies are used to scan the entire tumor thickness and reach the corresponding depth.

The first method is typically used at low energy proton therapy facilities for eye melanoma treatment, like the CATANA protontherapy beam line at INFN-LNS in Catania (Italy). Several modulator wheels are available according to the tumor dimension and they are designed taking into account, in a proper way, the weights of the single pristine peaks. To create a flat dose in the region of interest, the total dose obtained as the sum of all pristine profiles must be equal to a constant value; mathematically it corresponds to solve a system of equations, each one related to a specific depth, in which the weights of each pristine peak represents the variables to determine. Details on this method are reported in [101].

As an example, figure 3.38 shows the expected SOBP profile resulting as the sum of several weighted pristine peaks, in the energy range between 40 and 60 MeV.

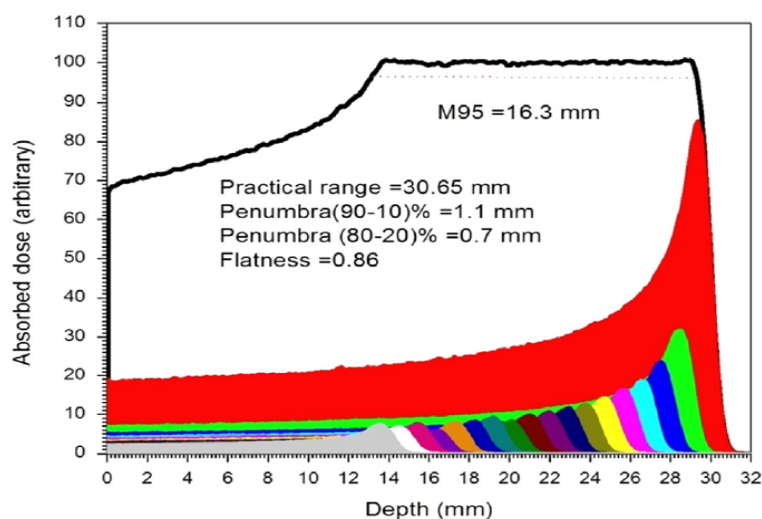


Figure 3.38: Expected SOBP profile (black) constructed with the weighted mono-energetic profiles (coloured peaks).

In this preliminary study, the possibility of obtaining flat longitudinal dose distributions of clinical interest with laser-driven beams, has been investigated. In principle, a similar approach could be followed, that means using high energy mono energetic proton beams and passively degrading them to achieve the required depths. However, for this kind of approach, high fluxes are typically required, because of the huge scattering effects on the modulation wheel, that actually is not an issue when dealing with conventional machines, like cyclotrons and synchrotrons. For laser-driven beams, the situation could be quite different, considering that for higher energy there could be sensitive losses in particle fluxes.

Therefore, the optimal solution would be achieved by using each single shot without any passive degradation, which means a kind of *active modulation*. The ESS realized for the ELIMED beam line has been actually designed in order to allow for this kind of modulation. Indeed, the current in the coils, responsible of the magnetic field, can be changed with a frequency up to about 1 Hz, which means that different energies can be selected at the same frequency. In particular, this approach has been demonstrated to be feasible for energy ranging between 30 and 60 MeV [27].

In the studied approach the ESS will operate as an active energy modulation system providing proton beams of different energies in consecutive shots, so that a total SOBP depth-dose profile results from dose accumulation of a certain number of properly weighted shots. The theoretical proof of principle of such approach has been carried out by means of the Geant4 simulations, using the ELIMED application, to demonstrate its feasibility for future irradiations of clinical interest at the ELIMAIA beam line.

In particular, the followed approach is based on three steps:

- Using a fixed quadrupole geometrical configuration for a certain energy. Indeed, due to the foresees high repetition rate of 1 Hz, it will be not possible to change the distances between the PMQs and the target for each shot, because it would require much larger configuration times. Therefore, a single geometrical configuration which guarantees to transport a wide energy range with a good transmission efficiency downstream the PMQs system, has to be chosen.
- Changing the magnetic field of the ESS, possibly maintaining the same slit aperture, according to the energy to be selected shot to shot. The magnetic field of the dipoles, i.e. the current, can be realistically changed with a frequency of 1 Hz.
- Accumulating different shots per selected energy, according to the required weight to obtain a flat longitudinal dose, previously calculated with a dedicated algorithm.

In order to fulfill the first point, the energy spectrum of protons after the focusing effect of PMQs system, using the 60 MeV geometrical configuration already shown in section 3.2.2, has been simulated and shown in figure 3.39. The input of the Geant4 simulation was a PIC-2D output obtained simulating a laser with an intensity of $5 \cdot 10^{21}$ W/cm² impinging on a thin nanosphere (NST) target reported in [102]. In particular, a decreasing almost exponential energy spectrum with an energy cutoff of 80 MeV and a constant divergence angle for all proton energies of $\sim 25^\circ$ has been obtained, reproducing the simulation reported in [102].

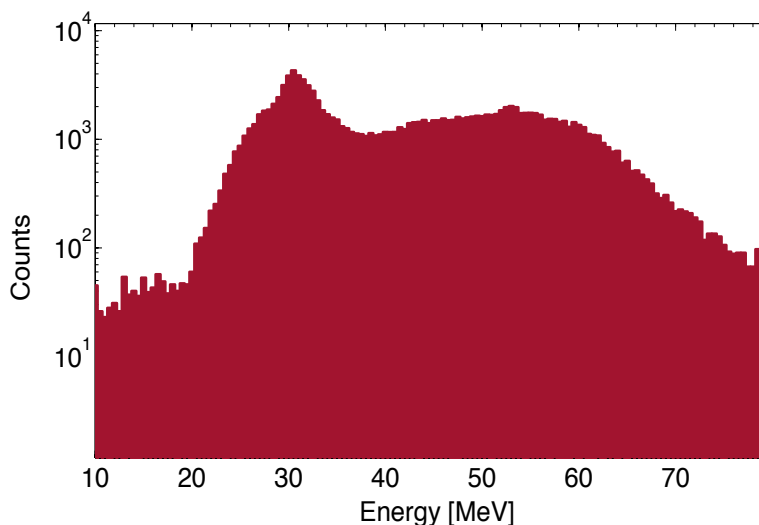


Figure 3.39: Proton energy spectrum obtained downstream the PMQs system set to transport 60 MeV protons.

As it is shown, although the PMQs are arranged to optimize the 60 MeV proton transport, still protons between 20 and 80 MeV are transmitted. In particular, a good transmission through the PMQs is visible between 30 and 60 MeV, which can be properly selected by the ESS. As a consequence, the second point can be fulfilled, using the beam shown in figure 3.39 as an input for the ESS and performing a set of simulations, in which the ESS slit is fixed at 5 mm width and the dipole magnetic field changes according to the scaling law reported in 2.11, i.e. the energy selected downstream the ESS.

A $2 \times 2 \times 6 \text{ cm}^3$ water phantom and scorer is placed downstream the ESS, after the last collimator, to retrieve the obtained depth-dose profiles.

Figure 3.40 shows the energy spectra obtained with the ESS magnetic field set to select the energies required to obtain the SOBP profile, fixing 5 mm slit width. The energies selected from the ESS are reported in the legend of figure 3.40.

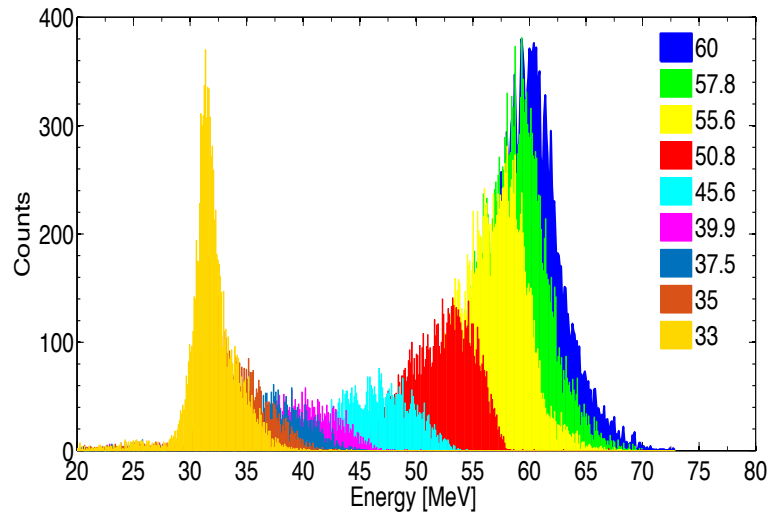


Figure 3.40: Energy spectra retrieved downstream the ESS, after the last collimator, varying the ESS magnetic field according to the energies to be selected (different colours).

Furthermore, the weight for each pristine peak has been calculated in order to obtain a flat SOBP profile following the procedure explained in details in [101].

The SOBP, in arbitrary units, obtained along with the single weighted mono-energetic Bragg peaks are shown in figure 3.41.

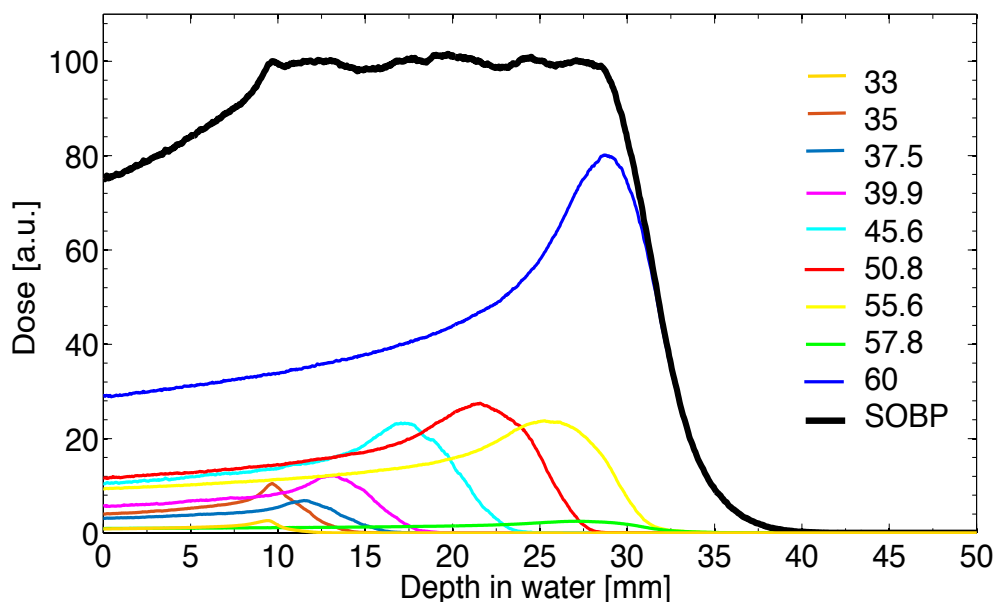


Figure 3.41: Spread Out Bragg Peak profile, in arbitrary units, obtained with all the weighted pristine peaks corresponding to energy spectra shown in figure 3.40.

As shown in figure 3.41 a flatness region (here defined as the distance between 98 % of proximal and distal dose) of about 20 mm has been obtained with only 9 different pristine peaks, which means nine different magnetic field values of the ESS. It is worth noting that this is a realistic possible example of ocular tumour size, typically treated with conventional proton beams. Moreover, an homogeneity within 3 % has been achieved in the modulation region, which is even clinically acceptable. However, a 80%-20% distal fall-off of about 3 mm has been found, which is still unacceptable from the clinical point of view.

Nevertheless, this could be quite easily improved optimizing the energy spread of the highest energy peak (in this case 60 MeV), corresponding to the longest range, in order to have a steeper fall-off.

In order to investigate the feasibility of the described procedure also in terms of irradiation time, a preliminary computation of the required shots per peak has been performed, according to the pre-calculated weights obtained for each pristine peak shown in figure

3.41.

Let's suppose to deliver an amount of dose which is typically released in a single session of an ocular proton therapy treatment (i.e. 15 Gy). If the obtained Spread-Out Bragg Peak is normalized to the required dose, it is possible to retrieve the absolute contribution in dose for each peak (figure 3.42). Simply considering the ratio between these values and the ones calculated for just one shot (considering a realistic number of particles per shot from PIC simulations), it is therefore possible to obtain the number of times any single pristine peak has to be repeated, provided to ideally have 100 % shot-by-shot reproducibility.

Assuming, as reference realistic condition, the one obtained for 60 MeV with 100 μm tantalum scattering foil and 2 meters of air reported in section 3.3.3 (which represents a good compromise between transversal beam uniformity and fluence losses) it is possible to scale the doses per shot obtained just after the kapton window to the ones required in this more relevant configuration, i.e. the SOBP at 15 Gy. Provided that the number of shots must be an integer, some approximations have to be included for the final computation. With the mentioned assumptions and following the described procedure, about 1000 shots are necessary to obtain the SOBP at 15 Gy shown in figure 3.42.

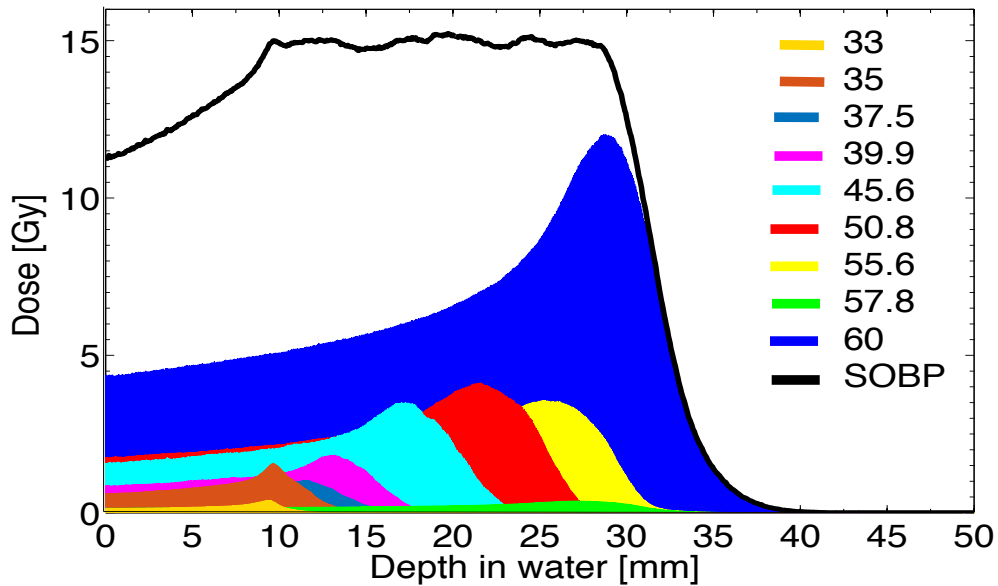


Figure 3.42: Spread Out Bragg Peak normalized at 15 Gy along with the weighted corresponding pristine peaks.

Considering both the laser repetition rate and the ESS active modulation frequency of 1 Hz, the SOBP shown in figure 3.42 is obtained in about 16 minutes of irradiation, which could be compatible with cell sample irradiations but not feasible for eventual clinical irradiations.

However, considering a laser repetition rate of 10 Hz, which will be possible at the ELI-MAIA facility once in operation, and still an ESS frequency of 1 Hz, a total irradiation time of about 110 s is obtained, which is even compatible with clinical conditions.

It is worth pointing out that the previous description has to be considered as a preliminary feasibility study. Indeed, still limitations are present in the final results and some approximations have been introduced for the computation.

However, the described study gives a valuable indication of the feasibility of future in-vitro and in-vivo irradiations using laser-driven proton beams transported with the ELIMED beam line.

More in general, it provides a first theoretical study to investigate possible future transport

configurations of clinical relevance, using the ESS as an active energy modulator. Once the ELI Beamlines facility will be in operation, there will be the opportunity to experimentally test them and to possibly verify the predicted results.

Chapter 4

The TOF based diagnostics system for the ELIMAIA beam line

As already introduced in section 2.2.3 a crucial role in the ELIMAIA beam line, is the one played by the Time Of Flight (TOF) diagnostics system, which can provide on-line important information as for instance the energy, the angular divergence, the ion species and the fluence of the transported beam. In order to monitor the beam characteristics and obtain a controlled beam at the end of the beam line, an on-line diagnostics system has been developed. The main online diagnostics system, which will be implemented along the ELIMED beam line, is based on the time of flight (TOF) technique performed using diamond and silicon carbide detectors [31, 32]. As it will be explained in details in section 4.1, the TOF method is one of the most established for low-energy laser-driven ion beam diagnostics [28, 29]. Nevertheless, the high-energy particles expected at ELIMAIA require the use of appropriate fast detectors and as a consequence the development of a specific analysis procedure able to properly reconstruct the energy spectrum of particles emitted starting from the acquired TOF signal.

4.1 Diagnostics of high-energy laser-driven ion beams: state of the arts and solutions for ELIMAIA

Laser-driven proton beam characteristics are very far from the conventional ones and, as a consequence, the detection of such high-pulsed beams cannot be performed using traditional methods. In particular, in view of the ELIMAIA beam line installation at ELI Beamlines, the main detector requirements needed to measure the energy and the flux of laser-driven beams are:

- radiation hardness ($>10^{12}$ p/bunch)
- fast charge collection, due to the intense proton pulse duration of about 10 ns
- good signal-to-noise ratio, due to the huge electromagnetic pulse (EMP) which characterizes the laser environment [103].

Several diagnostics methods are typically used in laser-driven acceleration field as the ones based on detectors like radiochromic films, image plates, nuclear track detector such as CR39, Thomson spectrometer or nuclear activation [104]. The main characteristics of these techniques are the following:

- Radiochromic films. They can be used in stack configuration to reconstruct the energy spectrum of the incident particles. Each layer records the deposited energy, and by using an optical density-dose calibration factor and an iterative method it is possible to extract the particle energy spectrum. For laser-driven ion beam diagnostics they are often used with an aluminium absorber wrapping the stack, to shield it from the UV and X rays coming from the laser-target interaction and also to stop the heavy ion contribution (in case the proton energy spectrum needs to be measured). Several works in literature have shown the results obtained with this technique [105, 106, 107, 108]. Moreover, the GAF-chromic films can be also used to measure the angular divergence and in particular the energy-angle dependence, giving also the 2D image of the beam shape in the transversal plane.

- CR-39 nuclear track detectors. They represent a very convenient tool for time-integrated measurements of charged particle fluences as well as for neutron dosimetry based on the detection of recoil protons [109, 110]. The main advantage of these detectors is their high sensitivity for ions within certain energy ranges and their insensitivity to photons and electrons for reasonable doses and to the EMP, which strongly characterizes the laser environment. Each incident particle going through a CR-39 detector, damages the polycarbonate plastic material and generates a crater which extends for few tens of nanometers along the particle trajectory [111]. After a chemical etching procedure, in a non-saturation regime $< 10^6 p/cm^2$ of the detector, it is possible to detect permanent track structures using professional microscope and count the tracks. For this reason, the CR-39 detectors are off-line dosimeters, giving a direct measurement of the particles fluence. Furthermore, the sizes of the crater, i.e. the diameter, depends on the ion species, the mass stopping power and the parameters used during the etching procedure, i.e. the concentration of the chemical solution, the temperature and the etching time [112]. By performing an energy calibration of such detector it is also possible to obtain a spectroscopic analysis of the CR-39, measuring the track diameter and extracting the corresponding incident energy. Such method has been widely used with conventional proton beams as reported in [111, 113, 114].
- Thomson Parabola Spectrometer (TP). It simultaneously provides the distribution of accelerated particles as a function of their energy, momentum, and charge-to-mass ratio [115]. The operation principle of TP, consisting of a small entrance pinhole, a parallel electric (E) and magnetic (B) fields and an imaging detector is shown in figure 4.1.

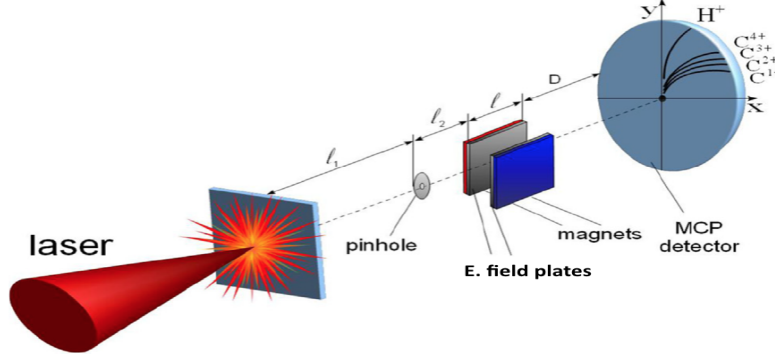


Figure 4.1: Scheme of the TP operational principle with laser accelerated charge particle beams entering the TP pinhole, passing through parallel electric and magnetic fields and tracing parabolas in the detection plane for the ions with equal q/M ratios [104].

Particles enter in electric and magnetic field through the pinhole and are deflected according to their charge-to-mass ratio (q/M). The coordinates at the detector position D can be expressed by:

$$x = \frac{qELD}{2E_i} \quad y = \frac{QBLD}{\sqrt{2ME_i}} \quad (4.1)$$

where E_i is the charged particle energy and L is the length of the electric and magnetic plates. Ions with the same charge-to-mass ratio, q/M will trace the same parabola in the detection plane. For these reasons the TP spectrometer offers the possibility to identify the accelerated ions, discriminating also the different charge states, looking at the different radius of the parabolic trajectories. Moreover, using for instance absolutely calibrated Microchannel-plate (MCP) coupled to a phosphor screen as detector, the energy distribution for each accelerated charge state can be retrieved [116, 117, 118].

Although the advantages of such kind of diagnostics, all of them are off-line devices, that require postponed analysis to extract shot information from the measurements.

Considering the high laser repetition rate (1-10 Hz) expected at ELIMAIA, the use of detectors able to give real-time shot-to-shot information of the beam is crucial in order

to monitor and control on-line the beam characteristics. Typically, electrons, protons and ions are accelerated by laser-target interaction and a time evolution signal, i.e. a Time Of Flight (TOF) signal, can be acquired using detectors such as Faraday Cups (FC) and ion collectors (IC) as reported in literature [119, 29]. They generate a signal, whose the amplitude corresponds to particle current impinging in the detector at a certain time which can be expressed by [29]:

$$J = \frac{dq}{dt} = ez_i n_i v_i \quad (4.2)$$

where t is the time-of-flight, q is the measured charge areal density, e is the elementary charge, z_i , n_i and v_i the ion charge state, density and velocity. Integrating eq. 4.2 it is possible to calculate the total charge collected. Nevertheless, the low time and energy resolution of these detectors limit the time separation of the different accelerated species or/and charge states, required for the identification and the energy reconstruction of the ion species, particularly, for high energy proton beams.

For all these reasons, fast devices as semiconductor-based detectors, e.g. silicon carbide (SiC) and diamond detectors, showing all these advantages [30, 120, 121] are the most appropriate for high energy laser-driven ion beam detection and have been chosen as TOF diagnostics system for the ELIMED beam line. As a matter of fact, both SiC and diamond detectors, thanks to a large band gap, respectively 3.26 eV and 5.45 eV, are particularly radiation hard and characterized by a high signal-to-noise ratio [122, 123, 124, 125, 126, 127]. Moreover, contrary to FC and IC, the pulse produced by ions impinging on the semiconductor detectors is proportional to ion energy and to depletion layer, i.e. applied bias [29]:

$$J = \frac{en_i m_i \mu_{eff} U_d}{2\epsilon d} v_i^2 \quad (4.3)$$

where m_i , n_i , v_i are respectively the ion mass, density and velocity, U_d the voltage applied to the semiconductor detector, μ_{eff} the semiconductor electron mobility and d the active layer thickness.

In particular, two different kind of Chemical Vapour Deposition (CVD) diamond detectors,

supplied by the CIVIDEC Instrumentation company, will be employed along the ELIMAIA beam line [128]. A 100 μm thick polycrystalline (pDD) and a 500 μm single crystal diamond (sDD) will be placed respectively downstream the quadrupole system and after the resistive quadrupoles and steerer downstream the in vacuum beam line as shown in figure 4.2.

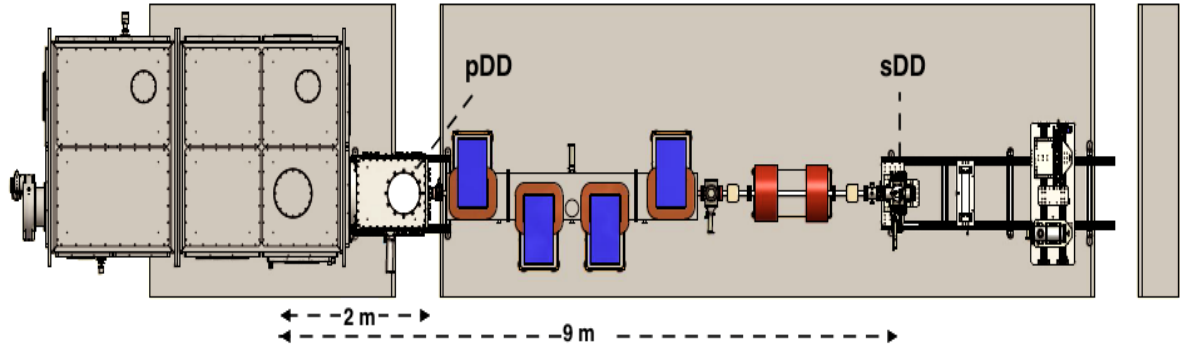


Figure 4.2: Sketch of the ELIMED beam line showing the distance of the pDD and sDD from the target position.

The pDD will measure the broad energy spectrum of the ion species focused by the PMQ system before the ESS, giving crucial information, as the beam energy component and flux, and to optimize the beam injection from PMQs system into the ESS. On the other hand the sDD placed downstream all the transport elements, before the in-air section, will allow to measure the energy and fluence for the dosimeters placed in air.

4.2 Diamond detectors for ELIMAIA beam line

Two diamond detectors will be employed for the diagnostics of the ELIMED beam line. They are provided with a housing specifically optimized for the EMP shielding, consisting of epoxy loaded FR4, gold metalized and completely RF shielded. The whole PCB board is contained in an Aluminium box with size 55 mm \times 55 mm \times 15 mm with extra RF shielding, useful for the EMP attenuation. They have been provided with window apertures of 2 mm diameter for the pDD and 3 mm diameter for the sDD. In figure 4.3 pictures

of the two detectors show the inner PCB board and the external aluminium housing.

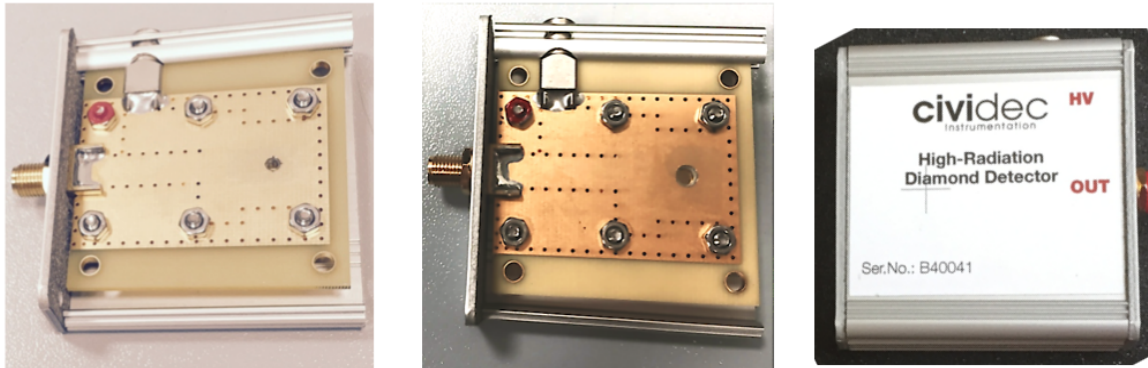


Figure 4.3: Pictures of the internal structure of pDD (left), sDD (center) and the pDD shielding box (right)

Moreover, both detectors are provided of an electronic circuit directly integrated in the PCB, made by a $2\text{ M}\Omega$ resistance and 100 nF capacitor, necessary to provide the voltage to the detectors and providing a low-pass filter to the output signal. The scheme of the integrated electronic circuit is reported in figure 4.4.

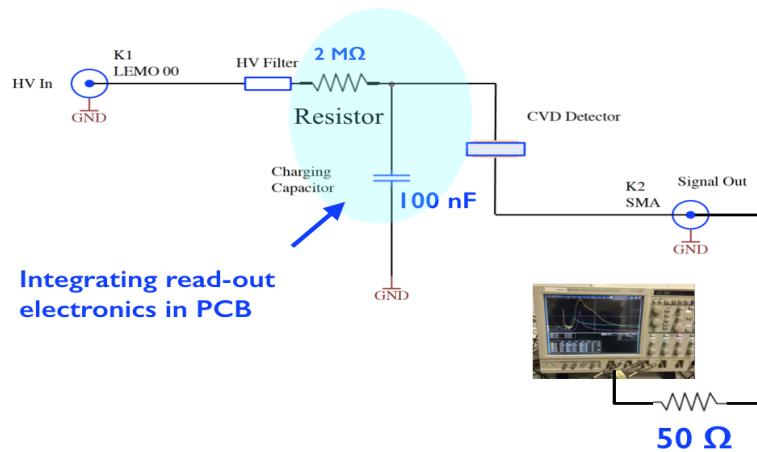


Figure 4.4: Illustration of the integrated circuit in PCB diamond detector board supplied by CIVIDEC

The operational characteristics of both detectors have been measured with an α particle ^{241}Am source facing both detectors. The radioisotope source emits α particles with specific

energies ranging from 5.1 MeV up to 5.5 MeV. The detectors were placed in a small in-vacuum chamber, as shown in figure 4.5, a CIVIDEC C2 Broadband Amplifier has been used for the signal amplification; the signal has been sampled with a 2 GHz Le Croy digital oscilloscope with a 50 Ω load impedance. Both detectors were biased using a CAEN DT1471HET power supply.

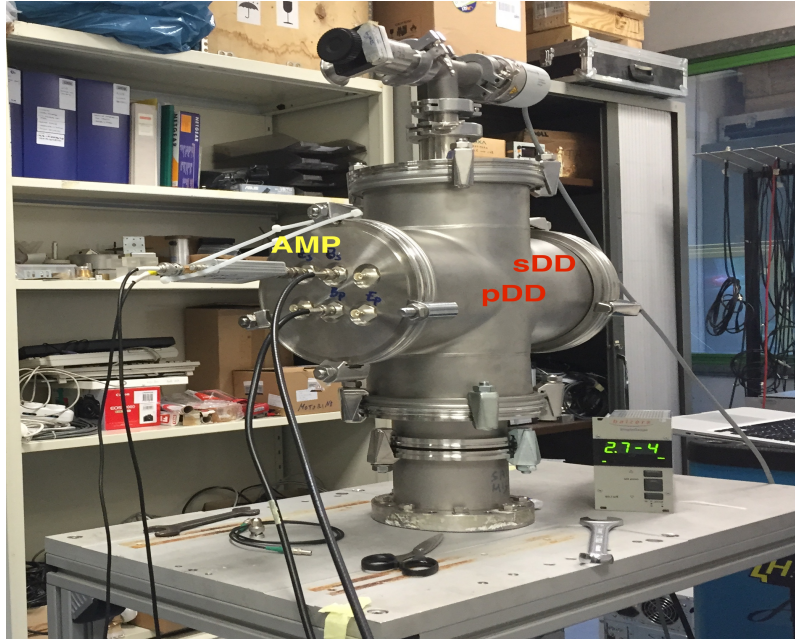


Figure 4.5: Picture of the vacuum chamber used for the test.

The signal amplitude dependence from the applied voltage has been measured for the sDD, as shown in figure 4.6 [32]. As expected, the signal amplitude increases with the voltage, applying from 250 Volt to 400 Volt, the latter being the operational value suggested by the company. At such voltage, a rise time of less than 2 ns has been measured, as shown in the inset in figure 4.6. The signal acquired applying a positive voltage of 200 V to the pDD is also shown in figure 4.7. In this case, a rise time of less than 400 ps has been measured with this detector (inset figure 4.7).

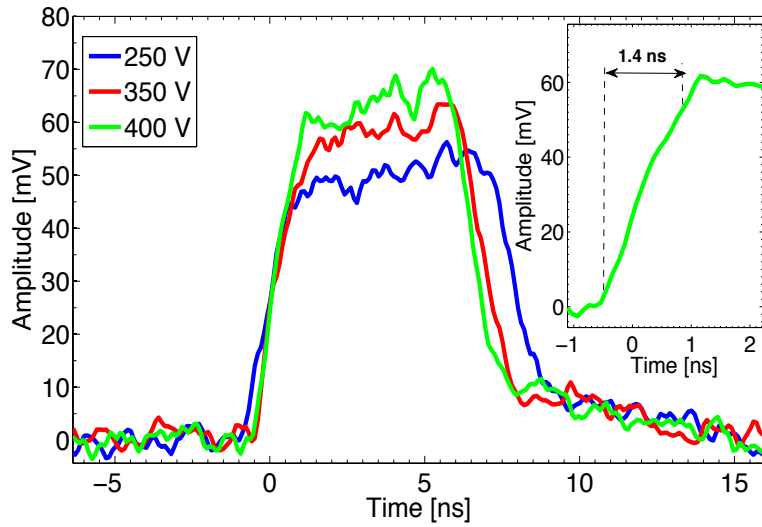


Figure 4.6: Signal acquired by the sDD detector applying 250 V (blue), 350 V (red) and 400 V (green). The inset shows the rise time of the signal applying 400 Volt [32].

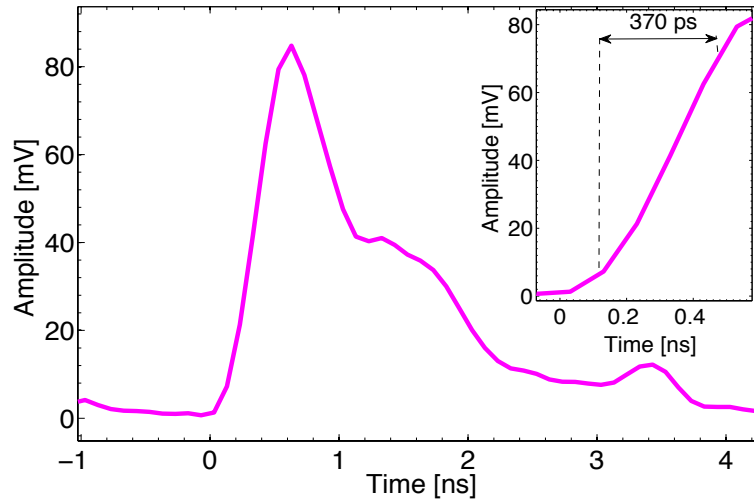


Figure 4.7: Signal acquired by the pDD detector applying 200 V and rise time of the signal (inset top-right) [32].

The results, in agreement with the specification given by the CIVIDEC, show a faster response for the thin pDD with respect to the thick sDD diamond detector. For such reason, the pDD will be placed closer to the target, where it will be necessary to disentangle the contributions of the fast beam component and a better time resolution is required. On the

other hand the $500\ \mu\text{m}$ thick sDD is more appropriate to measure the energy spectrum at the end of the beam line where the beam will show a narrow energy bandwidth and almost no ion target contaminants thanks to the selection system and lower fluxes.

In order to further investigate the pDD time response in a TOF configuration with high-energy proton beam, a test experiment using the 62 MeV proton beam delivered by the superconducting cyclotron at INFN-LNS has been performed. The main aim of the experiment was to measure 62 MeV proton beam TOF together with the corresponding uncertainty. For this purpose two detectors have been used as shown in figure 4.8: an in transmission $500\ \mu\text{m}$ thick single crystal diamond detector (D1) supplied by Diamond Detectors Ltd [129] as stop detector and the ELIMAIA pDD (D2) placed downstream at 289 cm, acting as start detector.

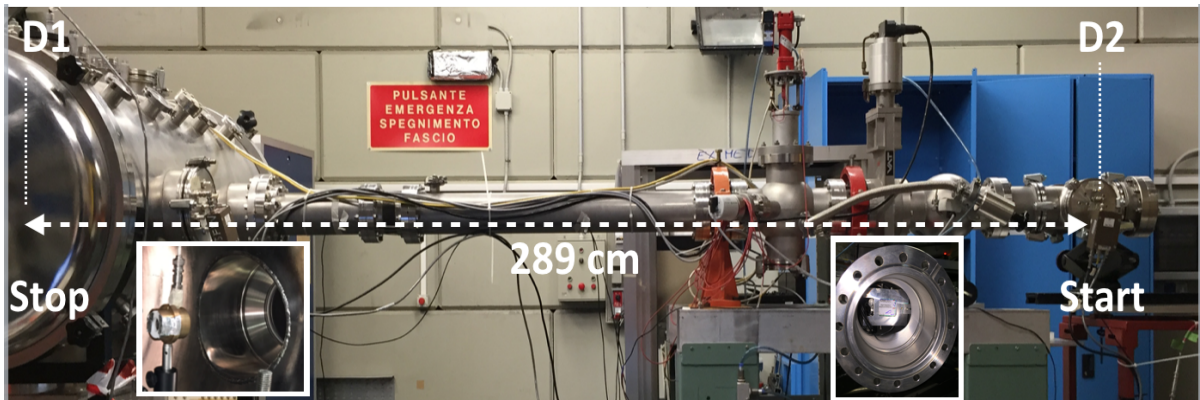


Figure 4.8: Experimental setup of the test performed @LNS with 62 MeV proton beams. The relative distance between the start and the stop detector is shown in the picture. In the insets: the details of D1 and D2 mounted along the beam line.

Two different electronic read-outs have been used for both detectors in order to compare the performances: i) a current amplifier CIVIDEC C2 Broadband Amplifier, and ii) a standard chain composed by a preamplifier 142A followed by a Timing Filter Amplifier 474, both NIM modules supplied by ORTEC [130]. The signals were stored using a 2 GHz Le Croy digital oscilloscope and a CAEN DT1471HET power supply has been used to provide the voltages (100 V to D2 and 400 V to D1). Whenever the start and the

stop signals are in coincidence, the difference between the two time signals corresponds to the TOF of the 62 MeV protons impinging on both detectors. The energy loss of 62 MeV protons inside D1 has been evaluated with LISE++ [131] and corresponds to 1.7 MeV. As a consequence, the effective kinetic energy of protons leaving D1 is of 60.3 MeV. Therefore, considering such energy loss, the proton TOF corresponding to a 289 cm flight path is 28.27 ns. In order to assure the coincidence between the two detector signals, avoiding long acquisition dead time, the start signal, i.e. the acquisition trigger, has been generated with the D2 whereas the D1 signal has been opportunely delayed and used as the acquisition stop. The signals in coincidence acquired from the two detectors in coincidence using the CIVIDEC amplifier electronics are shown in figure 4.9. Figure 4.10 shows the signal acquired by D2 using the ORTEC electronic readout.

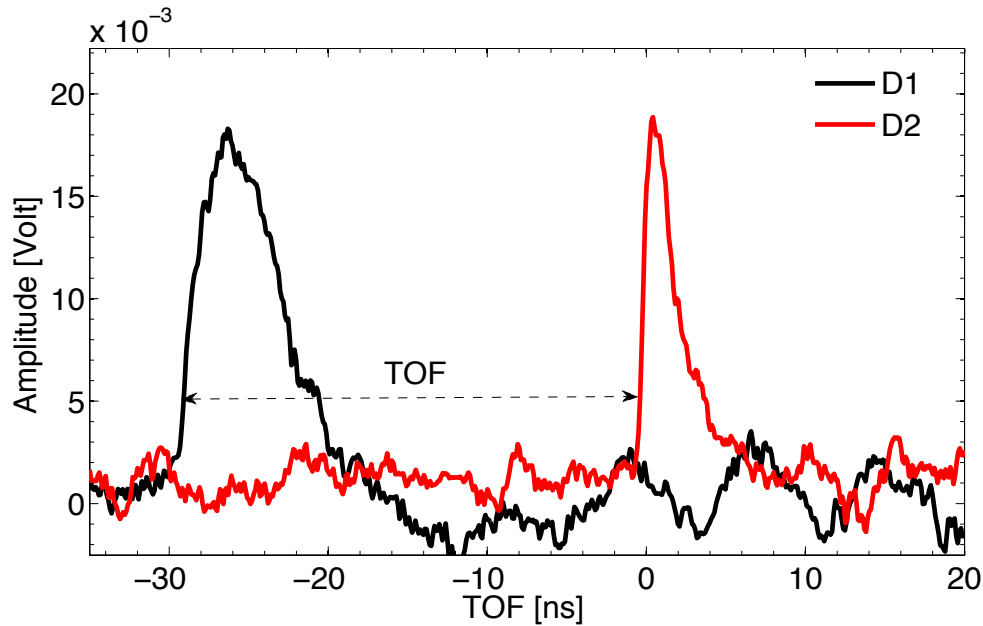


Figure 4.9: Signals from D1 (black) and D2 (red) in coincidence, acquired using the CIVIDEC current amplifier.

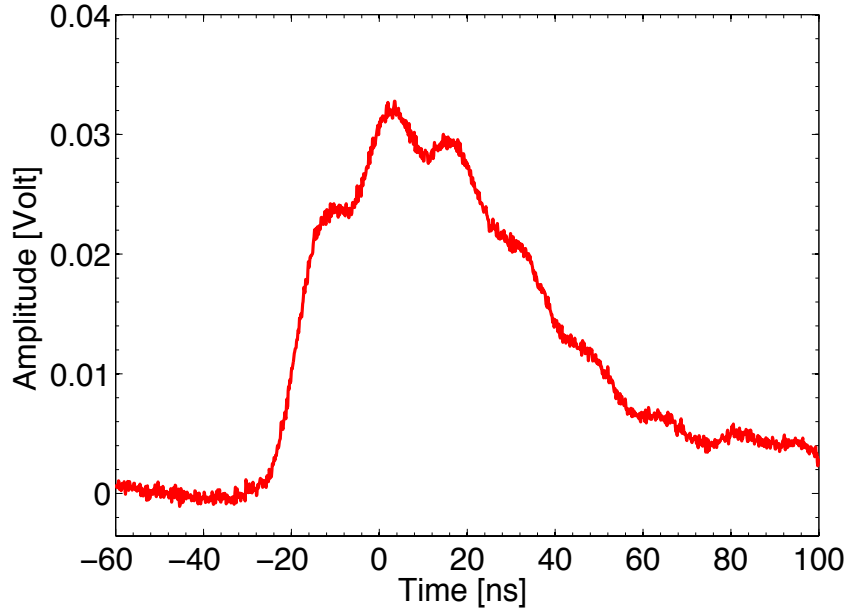


Figure 4.10: Signal acquired by D2 with the ORTEC electronic readout.

The rise time and the time resolution for D2 detector have been measured for both the electronic readouts. The time resolution of a detector, being directly connected with the *Root Mean Square* (RMS) time jitter, can be expressed by [132, 133]:

$$\sigma_t = \frac{t_r}{S/N} \quad (4.4)$$

where t_r is the rise time and S/N is the signal to noise ratio.

The rise time and the time resolution values obtained using both electronic readouts for the D2 detector, i.e. ELIMAIA pDD, are listed in table 4.1.

	Standard ORTEC chain	CIVIDEC chain
t_r	10 ns	370 ps
σ_t	300 ps	40 ps

Table 4.1

As one can see from a comparison, the CIVIDEC current amplifier, thanks to a smaller time constant, is more suitable for timing measurement leading to a time resolution measured

for the pDD of less than 50 ps. The TOF spectrum acquired using the CIVIDEC electronic, is shown in figure 4.11.

In order to compensate for the *amplitude walk* effect [132] on the signal which might cause large uncertainties, a *normalized threshold* approach was chosen to extract the proton arrival time for each signal [126]. As shown in figure 4.11, the TOF spectrum obtained has been fitted using a Gaussian function, resulting in a centroid at 28.41 ± 0.01 ns, $\sigma = 117 \pm 6$ ps and FWHM = 278 ± 14 ps. The result is in rather good agreement with the expected theoretical TOF. The time resolution obtained for the TOF measurement using D1 and D2 detectors is about 1% confirming the advantageous time characteristics of such kind of detectors.

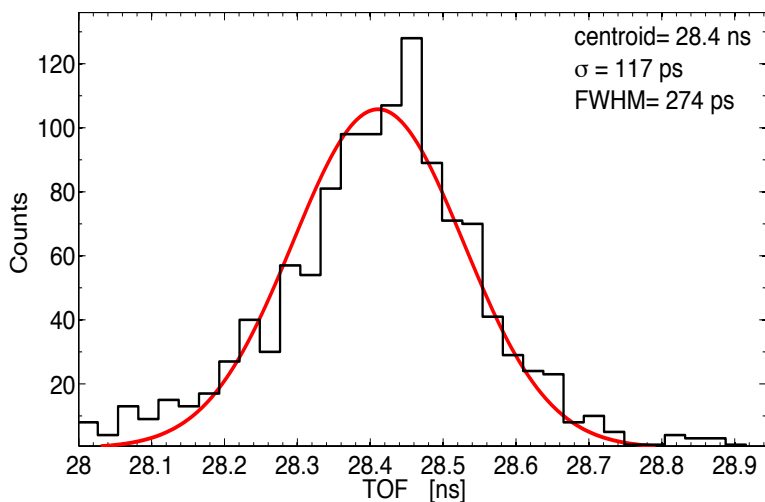


Figure 4.11: TOF spectrum obtained as the difference between the start (D2) and stop (D1) time signal. A Gaussian fit has been performed; the parameters obtained from the fit are reported in the figure.

4.3 Time Of Flight method: new approach with high-energy laser-driven ion beams

As it has been discussed in section 4.2, diamond detectors will be employed along the ELIMED beam line using the TOF technique to perform real-time beam diagnostics. As

a matter of fact, the time of flight method, based on the measurement of the time needed to reach the detectors from accelerated particles, has been used as a well-established method for low-energy laser-driven beam diagnostics with low-power laser and low repetition rate as reported in literature [134, 135]. The study of plasma formation due to the target ablation and its time evolution using TOF method can help to understand the mechanism of particle expansion under certain conditions and to develop several models to describe the behaviour of accelerated species from the target surface and, as a consequence, their time evolution.

To better understand the TOF signal it is useful to describe the particle acceleration mechanism during the laser-matter interaction. In particular, when the plasma is created and the particles are emitted from the target surface an initial unstable phase, in time and space, exists: multiple collisions still happen between ions and ion species are not yet fixed [136]. This non-equilibrium zone, called *Knudsen layer*, typically $\ll 1$ mm, determines an altered velocity distribution function of particles emitted [136, 137]. When no collisions happen between the thermally emitted particles the velocity distribution can be described by the well-known *Maxwell Boltzmann* function [138]:

$$f(v_x, T_s) \propto \exp(-mv_x^2/2k_B T_s) \quad (4.5)$$

where v_x is the velocity component perpendicular to the target surface, k_B the Boltzmann constant and T_s the surface temperature.

At high densities in Knudsen layer, due to not-negligible collisions among the emitted particles, the previous expression must be replaced by the *Maxwell Boltzmann shifted function* expressed in a centre-of-mass coordinate system [136]

$$f(v_k, T_k) \propto \exp(-m(v_x - v_k)^2/2k_B T_k) \quad (4.6)$$

where v_k is the center of mass velocity, the so called *shift* velocity and T_k was shown to be about 70% of the target surface temperature T_s .

Due to the impossibility to solve analytically the Knudsen layer problem, the equation 4.6 represents a good approximation for the velocity distribution of particles able to go

beyond the Knudsen layer boundary. Such velocity distribution depends on the explicit center of mass velocity and temperature T_k lower than the one at the surface.

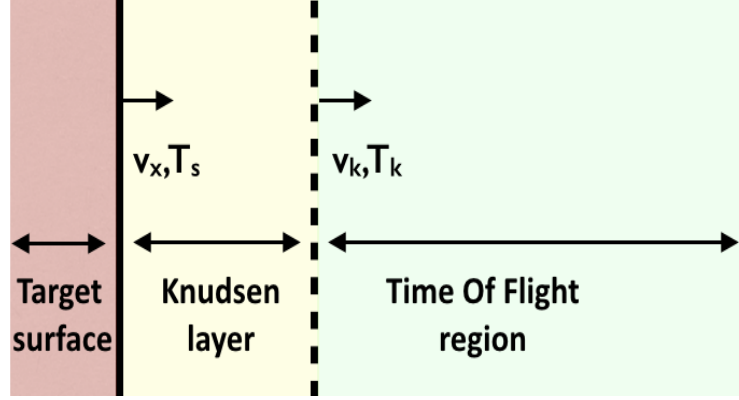


Figure 4.12: Sketch showing the spatial evolution of particle plume emitted from target ablation

As shown in figure 4.12, after the initial unstable phase, the so called TOF region starts, where the ion species are already fixed and no collisions happen anymore. Considering a small area detector placed at a reasonable distance from the target ($L > L_{cr}$ [139]) and on the axis perpendicular to target surface, the complete TOF signal, resulting from the sum of the single ion signal in the detector, can be derived from the equation 4.6 and expressed by [135]:

$$S(L, t) = \frac{L^{\alpha+1}}{t^{\alpha+4}} \sum S_{i,0} \exp \left[-\frac{m}{2kT_i} \left(\frac{L}{t} - v_{i,k} \right)^2 \right] \quad (4.7)$$

where L is the flight path, $v_{i,k}$ and $T_{i,k}$ respectively the shift velocity and temperature for each (i) ion species and α a parameter expressing the dependence of TOF detector signal from number of particle ($\alpha=0$), particle fluxes ($\alpha=1$) and particle energy deposited ($\alpha=2$). Basing on this theory, when different ion species are accelerated from target, the total acquired TOF signal results as a convolution of all the ion contributions reaching the detector [140, 141]. In this case, in order to disentangle the different ion species components and reconstruct the corresponding energy spectrum, a fitting procedure using the functions 4.7, called *Maxwell-Boltzmann shifted* function (MB), each for a specific ion population,

has to be performed.

On the contrary, when a single ion species is detected, either because the other ion species present as contaminants in the target are stopped by absorbers or magnetic selection systems, as the ELIMAIA beam line case, or because only one species is accelerated from the target as for instance using a pure hydrogen target, the TOF signal is directly the time evolution of such ion species and the energy spectrum dN/dE vs energy can be directly extracted from TOF signal.

Development and optimization of this procedure, in particular for high-energy laser-driven beams, has been one of the main goals of the present thesis work and will be described in details in the next sections.

4.3.1 Time distribution reconstruction: deconvolution procedure

A typical TOF signal is shown in fig. 4.13. This signal has been acquired during a recent experimental campaign at RAL laser facility [36], with the pDD at about 1 m from a 25 μm Al target in the backward direction. A 50 μm Al absorber was used to shield the detector and stop 2 MeV protons.

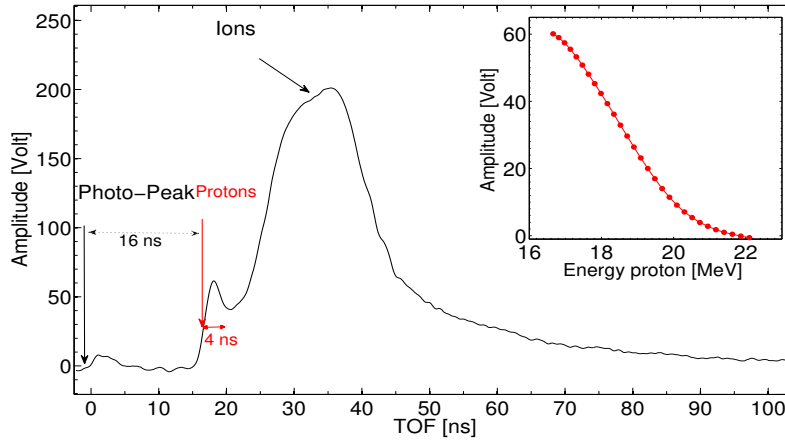


Figure 4.13: A TOF signal acquired by the pDD placed @ 1.22 m downstream the target is shown. The inset shows the incident kinetic energy calculated in the time range corresponding to the faster proton peak [31].

As one can clearly see in fig. 4.13, three peaks can be identified: the photopeak originating from the UV and X-ray laser-plasma radiation followed by a tail due to hot plasma electrons (0-8 ns), the peak generated by the fastest proton group (16-22 ns) and a broad peak arising from different ion species and charge state contribution, typically present in the target as contaminants, together with the slow proton component (22-47 ns).

The incident proton kinetic energy can be calculated from the measured TOF signal given the flight path, L . The measured TOF has to be corrected for the distance travelled from the source to the detector by the UV and X-rays using the formula:

$$t = TOF + \frac{L}{c} \quad (4.8)$$

where c is the speed of light and t is the TOF corrected for the photon flight path. Then, the incident proton kinetic energy can be obtained using the corrected TOF, t , by the well-known relativistic definition:

$$E_{kin} = (\gamma - 1)M_p c^2 \quad \gamma = \frac{1}{\sqrt{1 - \beta^2}} \quad \beta = \frac{L}{ct} \quad (4.9)$$

where M_p is the rest mass of proton or ion of interest and L is the flight path (i.e. the target-detector distance). As one can see in fig. 4.13, the peak arising from the fast protons is well separated by the slow ion contribution and rise time of 1.5 ns can be observed. The inset in fig.4.13 shows the incident kinetic energy calculated taking into account the relativistic correction from the measured TOF in the range between 16 ns and 22 ns, corresponding to the high energy proton component. Thanks to the diamond low sensitivity to the plasma visible and soft-UV radiation and the fast time response, a short photopeak with a temporal decay of about 5 ns and a rise time less than 1 ns is observed, allowing to clearly disentangle the proton energy cutoff and the high energy component from the photopeak even at about 1 m flight path. In particular, the shortest TOF measured (16 ns) indicates a maximum proton energy of about 22 MeV. On the other hand, when ion contribution on the total TOF signal is not negligible, as in this case, is quite difficult to perform a correct deconvolution of the signal, disentangle protons from other ion contaminants and

reconstruct the energy spectrum. In such case, TOF diagnostics can be coupled with other diagnostics such as Thomson Parabola spectrometers, which provide the identification of the different ion species, charge states and the corresponding maximum energies. The use of absorbers can also allow to stop the heavy ions, so that only protons with a sufficient energy are measured, obtaining a pure proton signal generated uniquely by the higher energy component. Details of these approaches in presence of a large ion contamination will be reported in next sections.

On the other hand, as an example, figure 4.14 shows a TOF signal acquired by a SiC detector during an experimental campaign carried out at PALS laser facility of the IPP CAS (Institute of Plasma Physics, Czech Academy of Sciences) using the innovative ELISE cryogenic system [142] which produces a pure solid hydrogen ribbon used as target allowing to accelerate high intensity protons without any ion contamination. The SiC detector was placed at about 1 m from target, 5° with respect to the beam axis, in the forward direction. A voltage of 150 Volt was applied to the detector, corresponding to a $5 \mu\text{m}$ depletion layer, according to [123]. A $4.8 \mu\text{m}$ thick Al absorber was mounted on top of the detector in order to stop the lowest energy proton component (up to 450 keV protons). In this case, the total TOF signal is generated uniquely by the protons accelerated from the pure Hydrogen target and the energy spectrum can be directly reconstructed from the TOF signal. Nevertheless, a deconvolution of the total TOF signal can also be performed by using the MB functions reported in eq. 4.7 in order to identify different energy proton populations as shown in figure 4.14. In particular, three different MB shifted functions have been used to fit the total TOF proton signal, assuming three different proton populations. In figure 4.14, the values of the shift velocity and temperature for each proton group are also reported, revealing the potentiality of this technique to study plasma characteristics and behaviour [33].

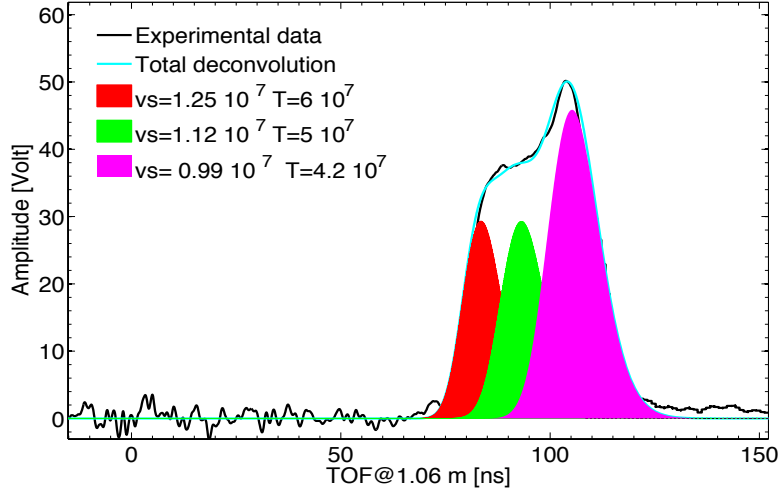


Figure 4.14: TOF signal acquired with a SiC detector at PALS with the ELISE cryogenic target, laser energy of 597 J, and deconvolution performed with the MB shifted functions [33].

4.3.2 New procedure for high-energy proton spectrum reconstruction

For semiconductor-like detectors, as for instance SiC and diamond, whose the response depends on the energy deposited in the active volume, the conversion of the TOF signal into the energy distribution for a specific ion species, represents a critical step for the reconstruction procedure. Typically the charge collected in such detector due to N incident particles, depositing energy E in the active layer, is given by [132]:

$$Q = \frac{eNE}{E_g} \quad (4.10)$$

where E_g is the electron-hole pair energy creation, i.e. 7.78 eV for SiC and 13 eV for diamond detector.

Due to the very high-particle fluxes (reaching 10^{12} p/bunch), the detector will be used in *current* mode, namely the single incident particle signals cannot be distinguish among each other and a total mean current is detected, being proportional to the particle rate multiplied for the charge generated in the detector by a single incident particle.

By deriving the 4.10, a relation for the current and the energy distribution dN/dE can be obtained [33, 29]:

$$\frac{dN}{dE} = \frac{\epsilon_g V(t)}{eRE^2} \left(-\frac{1}{2} - \delta t \right) \quad (4.11)$$

where m is the mass of the specific ion, $V(t)$ is measured voltage signal, as a function of the time, R is the total resistivity of the detector readout (including termination on the oscilloscope), t corresponds to the TOF from equation 4.9, δt is the oscilloscope time sampling (negligible by using fast scopes) and L is the detector distance. Equation 4.11 expresses the energy distribution of a specific ion species, with a mass m , impinging on the detector. In case of different ion species accelerated, the term $V(t)$ in the equation 4.11 is the MB fitting function, for the specific ion species as resulted from the deconvolution procedure explained in section 4.3.1. On the other hand, when only one species is accelerated, $V(t)$ is the acquired signal amplitude. By integrating the equation 4.11 the total number of particles impinging in the detector can be extracted. Since such kind of detectors, having typically few mm diameters, intercept only a portion of the whole accelerated beam, in order to obtain the energy spectrum and hence the total number of particle (protons or a specific ion) accelerated from laser-target interaction, the equation 4.11 has to be divided for the solid angle ratio: $\Omega_{BEAM}/\Omega_{det}$; where Ω_{det} is the detector solid angle, depending on the detector size and distance from target, and Ω_{BEAM} is the whole beam solid angle, calculated measuring the total beam size at the same position of the detector. This statement is an approximation based on the assumption that the particle beam has an isotropic spatial distribution.

Equation (4.11) has been widely used for energy spectrum reconstruction of low energy laser-driven proton beams, see for instance [29] and references therein.

Actually, for low energy particles (few MeV), whose the range is less or equal than the detector active thickness, the energy variable E in equation (4.11) corresponds to the incident kinetic energy calculated using the 4.9 relation, and the energy distribution can be directly obtained from the TOF signal. On the contrary, for those particles with

a sufficient kinetic energy to traverse the detector thickness releasing only a portion of their incident energy into the detector active layer, the energy variable E in equation 4.11 corresponds to the effective energy loss in the detector active layer which must be taken into account in order to obtain the correct energy spectrum. Considering the ion maximum energy expected to be accelerated and transported at ELIMAIA, the development of a procedure able to reconstruct the energy distribution for high-energy particles is a crucial point for a reliable beam diagnostics.

In this case, once the measured TOF is transformed in the incident kinetic energy using formula 4.9, the corresponding energy loss in the detector active thickness for each particle with a specific incident energy can be estimated using a Monte Carlo-based simulations. A simple energy loss calculation, taking into account different experimental setup conditions (as for instance detector material, detector active layer, absorber material and thickness, etc..) has been simulated using the Monte Carlo toolkit Geant4. In particular, the detector has been simulated in terms of material, density and thickness. A point-like parallel beam has been simulated as input assuming a flat energy spectrum whose energy range is determined by the TOF values measured given the shot of interest. Each particle generated in Geant4 is tracked and information, as energy and position, can be retrieved along the track till the particle stops. In such a way, it is possible to follow each generated particle along its path within the detector and calculate the corresponding energy released. Following this procedure thanks to the simulation, it is possible to obtain, for a given acquired TOF value, the energy loss in the detector as a function of the incident energy. An example is reported in Figure 4.15. It shows the TOF signal acquired with the pDD diamond detector placed at 2.35 m from target, during an experimental campaign carried out at RAL laser facility. As one can clearly see, the fastest proton component identified by a narrow peak between 39 ns and 42 ns, has been analyzed by fitting (red line) the TOF signal in the time interval corresponding to proton kinetic energies in the range $\Delta E_p = 16 - 19$ MeV.

Figure 4.16 shows the energy loss in 100 μm thick diamond as a function of the incident

energy, $\Delta E - E$ plot, for proton with incident energies in the interval between 16 and 19 MeV. A power-function fit, red curve of figure 4.16, has been performed on the simulation results.

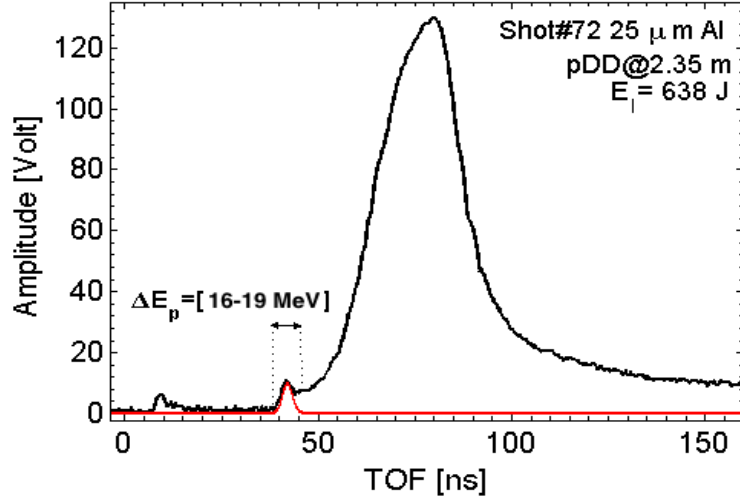


Figure 4.15: TOF signal acquired with pDD detector during the experiment carried out with Vulcan Petawatt laser at RAL laser facility. The red solid curve represents deconvolution obtained by fitting the fast proton peak using MB function.

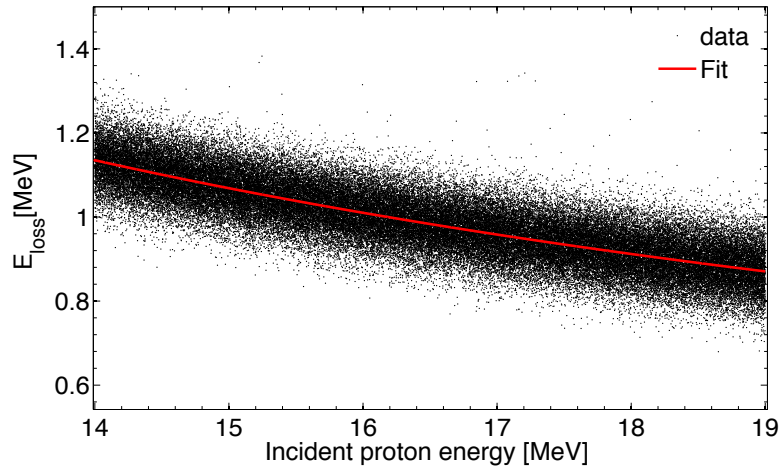


Figure 4.16: $-E$ plot simulated with Geant4 for protons with energies ranging from 16 and 19 MeV in 100 μm thick diamond.

Therefore, using the parameters obtained from fitting procedure, it is possible to evaluate

the average energy loss corresponding to the incident energy calculated from the TOF experimental data in the energy range of interest and reconstruct the energy spectrum using $E=E_{loss}$ in equation 4.11 (figure 4.17). The energy spectrum corresponding to the fast proton peak in the TOF signal shown in fig. 4.15 between 39 ns and 43 ns and obtained using the energy loss simulation is shown in figure 4.17.

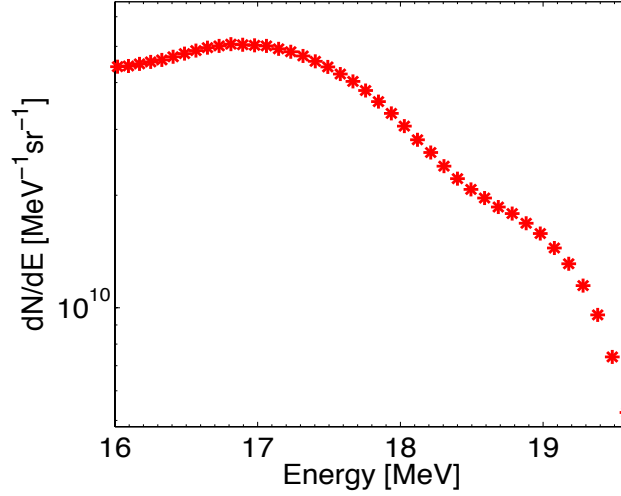


Figure 4.17: Proton energy spectrum corresponding to the TOF signal in 4.15 in the energy range between 16-19 MeV

Moreover, the use of the MC simulation can be also particularly useful when thin absorbers are placed in front of the detector to stop low-energy protons or ion component in the beam due to the target contaminants. Metallic or plastic absorbers may also help particle species discrimination, providing the minimum energy needed to traverse the absorber thickness for each accelerated ion species. Such information allows to determine, for a given ion species, the maximum expected TOF value corresponding to the minimum energy needed to reach the detector. In presence of an absorber, for those particles traversing the absorber and impinging in the detector, it is necessary to take into account, for a precise energy spectrum reconstruction, the fraction of the energy loss within the absorber thickness.

Using the Geant4 simulation toolkit, as it has been explained above, it is possible to simulate the absorber foil in terms of material and thickness in order to obtain the average

residual energy after the absorber as a function of the incident kinetic energy. Figure 4.18 shows the Residual Energy versus Energy plot for α particles with an incident energy ranging from 6 MeV up to 7.4 MeV traversing 6.5 μm thick aluminium foil.

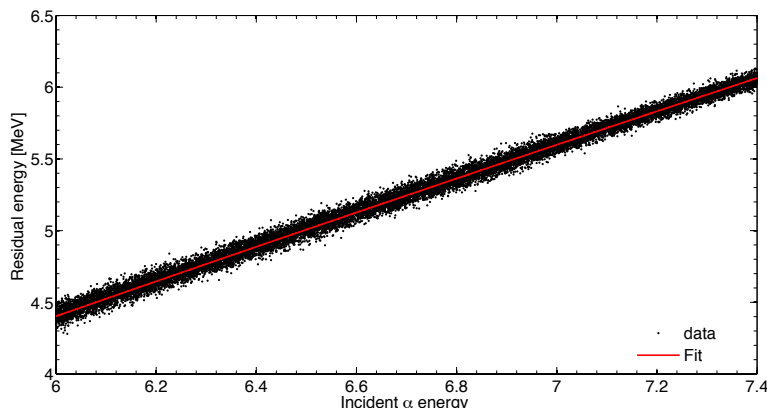


Figure 4.18: Residual energy of α particles in crossing 6.5 μm Al foil as a function of the incident energy.

Two cases can occur for particles with a sufficient energy to overcome the absorber:

1. Particles having a residual energy leaving the absorber such that they stop within the detector active thickness releasing their total kinetic energy inside the detector. In this case the variable E in equation 4.11 corresponds to the particle residual energy leaving the absorber thickness.
2. Particles leaving the absorber with a kinetic energy such that they do not stop in the detector thickness. In this case, the energy loss within the detector thickness has to be calculated using MC simulations.

Figure 4.19 shows an example of both cases described above. In particular, it illustrates the energy loss simulation for protons with an incident energy between 9 and 20 MeV through 500 μm thick aluminium foil and 150 μm thick single crystal diamond detector (sDD). As one can see, two regions can be distinguished: the first one (9-11 MeV) corresponds to protons which go through the 500 μm thick aluminium foil and release their residual

energy within the detector (case 1); the second region (11-20 MeV) corresponds to higher energy protons which do not stop inside the detector thickness (case 2).

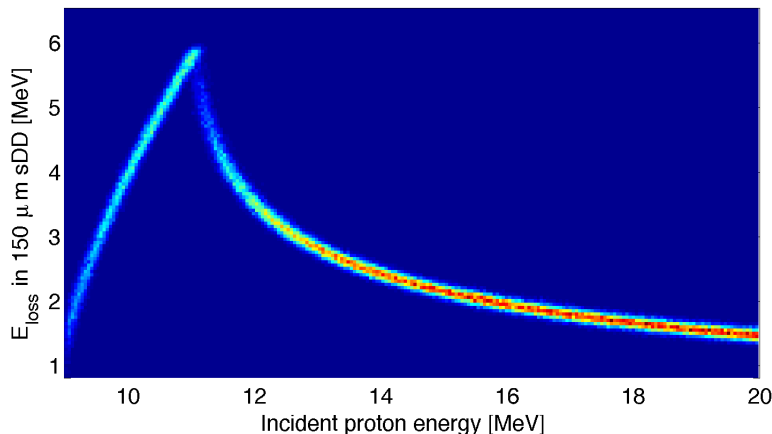


Figure 4.19: Proton energy loss through 500 μm thick Al foil and 150 μm thick single crystal diamond detector as a function of the incident energy. The colour map states the particle density

The maximum energy loss value, corresponding to 11 MeV incident energy, defines the transition from the two regimes, 1 and 2. This physical point can be directly visible in the TOF signal: for the corresponding TOF the signal trend changes indicating the different regime conditions.

An example of such effect is shown in figure 4.20. It shows the TOF signal acquired with a thin, 22 μm thick, SiC detector during a test experiment carried out with the Asterix laser system at PALS (CZ) using the ELISE pure-hydrogen cryogenic target system [142]. The SiC depletion region used during the experiment corresponds to about 5 maicron according to the applied voltage, 150 V [123].

The TOF signal (figure 4.20), has been fitted using the deconvolution procedure described in 4.3.1 with different MB functions. The energy spectrum (figure 4.21) has been reconstructed using the formula 4.11 considering the two different TOF regions : 60-80 ns (corresponding to the case 2) and 80-120 ns (corresponding to the case 1).

In the second region (for $\text{TOF} > 80$ ns) corresponding to protons which, after the absorber,

stop inside the detector active layer, the signal amplitude, being directly proportional to the energy loss, i.e. the incident energy, results much higher than the amplitude signal in the first region ($\text{TOF} < 80 \text{ ns}$), where protons do not stop in the detector active thickness and the amplitude depends on the energy loss, i.e. only a fraction of the total incident proton energy.

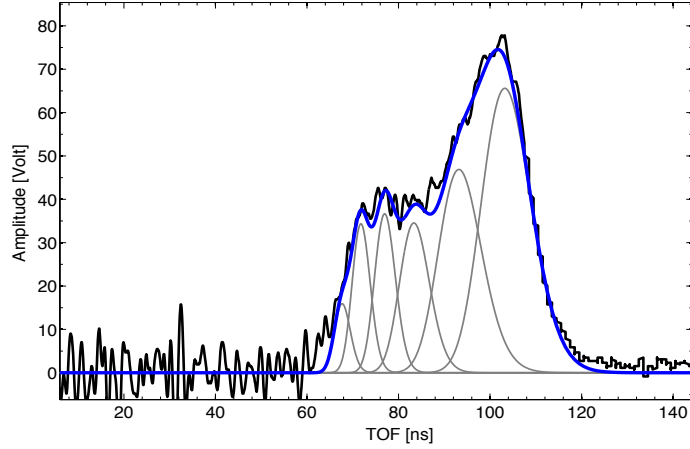


Figure 4.20: TOF signal acquired with SiC detector using a pure-hydrogen target at PALS laser facility. The thin grey solid curves represent the MB functions used to deconvolve the total signal. The thick solid blue curve represent the sum of all the MB functions.

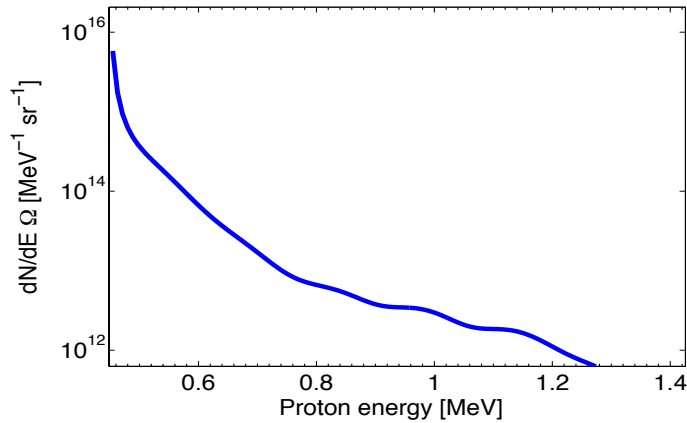


Figure 4.21: Proton energy distribution corresponding to TOF signal reported in 4.20. The number of protons per solid angle obtained integrating the energy spectrum is also reported.

Chapter 5

Experimental campaigns with TOF-based diagnostics

5.1 TOF analysis procedure validation with high energy laser-driven ion beams

The diamond detectors described in section 4.2 and the analysis procedure, developed for high energy laser-driven proton beam diagnostics presented in section 4.3.2, have been tested in an experimental campaign carried out using the Vulcan PW laser system at Rutherford Appleton Laboratory (RAL, UK) in collaboration with the Queen's University (Belfast, UK). The VULCAN laser system is a neodymium glass laser operating at a central wavelength of 1053 nm, delivering about 650 J in a time pulse of about 500 fs, capable to accelerate protons up to 60 MeV [36]. The main aim of the experiment was the cell irradiation with laser-driven proton beams in the forward direction. Besides the radiobiological purpose, it has also been possible to test the ELIMED TOF-based detectors for the first time with high-energy (several tens of MeV) laser-driven proton beams and extract from TOF signals the energy cut-off, the energy distribution and the corresponding fluence. The experimental setup and the results obtained exclusively for TOF diagnostics test, will be presented in next sections.

5.1.1 Experimental Setup

Different diagnostics have been used in order to validate the TOF technique. The experimental setup used in the experiment, shown in figure 5.4, consists of:

- Diamond detectors (TOF): 100 μm polycrystalline diamond detector (pDD) and 500 μm single crystal diamond detector (sDD). They were placed both in backward (laser incidence side) and forward direction (opposite to the laser incidence side), at about 10° with respect to the target normal direction at different distances from target (flight path) ranging from about 1 to about 4 m in backward direction (figure 5.1) and about 2.5 m in forward direction. TOF signals were stored with a 2.5 GHz 40Gs/s Tektronik digital oscilloscope terminated with a 50 Ohm load impedance. A power supply module (CAEN DT1471HET) has been used to provide a voltage of 200 V to pDD and 500 V to the sDD.

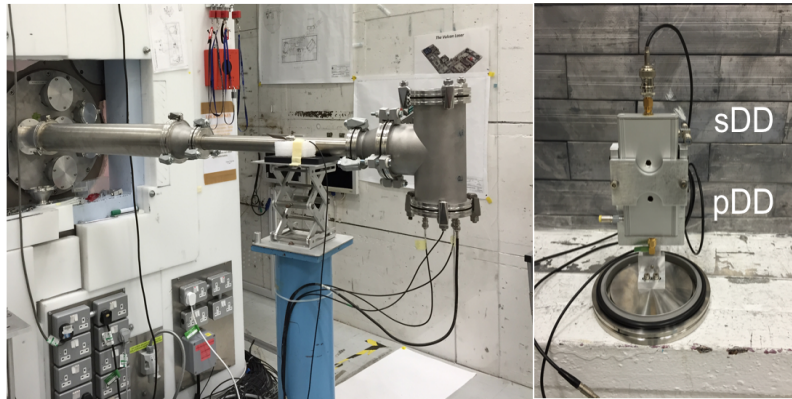


Figure 5.1: Pictures of pDD and sDD placed in backward direction in a beam pipe, used to increase the flight path, attached to the TAP chamber (left), detail of diamond detector holder (right).

- Thomson Parabola Spectrometer (TP). It was placed in backward direction, the distance between the target and the pinhole was 1.22 m. TOF detectors have been placed close to the pinhole at the same distance, as shown in figure 5.2. Image plates were used to acquire the image of different ion charge state trajectories within the

TP fields.

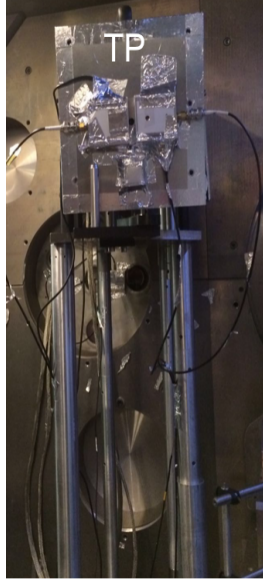


Figure 5.2: Picture of TP installed in backward direction.

- Radiochromic films, EBT3 type (RCF). They were used in stack configuration to measure the proton energy spectrum in forward and backward direction, at different distances from the target. Different thicknesses of Al absorber were used to wrap the RCF stack to stop x-rays and ion contributions.
- Nuclear track detector, CR-39 type. They were placed in backward direction at about the same distance and angle of TOF detectors, with different Cu absorber thicknesses, to disentangle between different proton energy components and to measure the absolute fluence (figure 5.3).

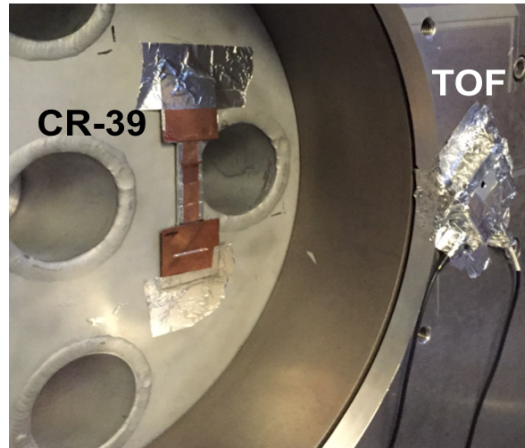


Figure 5.3: Picture of CR-39 detector placed on the interaction chamber walls in backward direction close to TOF detectors.

A 25 μm thick Al target was used during the entire experiment as shown in figure 5.4.

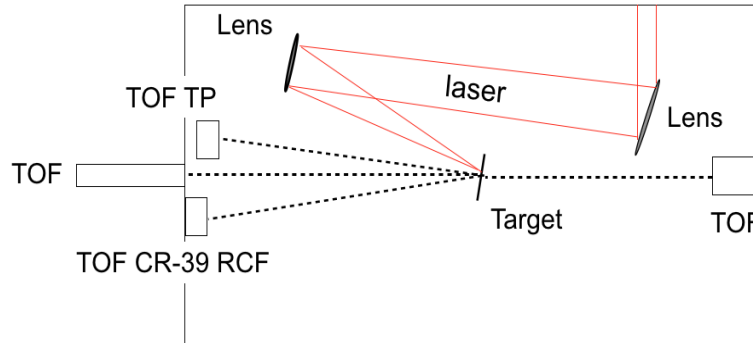


Figure 5.4: Experimental setup used in the TAP interaction chamber at RAL laser facility.

5.1.2 Analysis procedure and results of TOF signals acquired in backward direction

As mentioned in previous section, Thomson Parabola spectrometer, providing the identification of accelerated ion charge states and the corresponding energy cutoffs, gives complementary information to the TOF signal, helping in the analysis especially when the target contains ion contamination and not only protons are accelerated. Different ions, as for instance carbon and oxygen, are expected to be accelerated from the Al flat foil together

with fast and slow protons resulting in a TOF signal generated by different overlapping contributions.

Nevertheless, thanks to the ion parameters extracted from the TP image analysis, it is possible to identify the TOF signal, i.e. time intervals, exclusively generated by protons.

In such way, the proton energy spectrum can be retrieved using formula 4.11.

In order to better clarify the procedure, the TOF signal acquired by pDD in backward direction at a flight path of 2.35 m and without any absorbers is shown in figure 5.5.

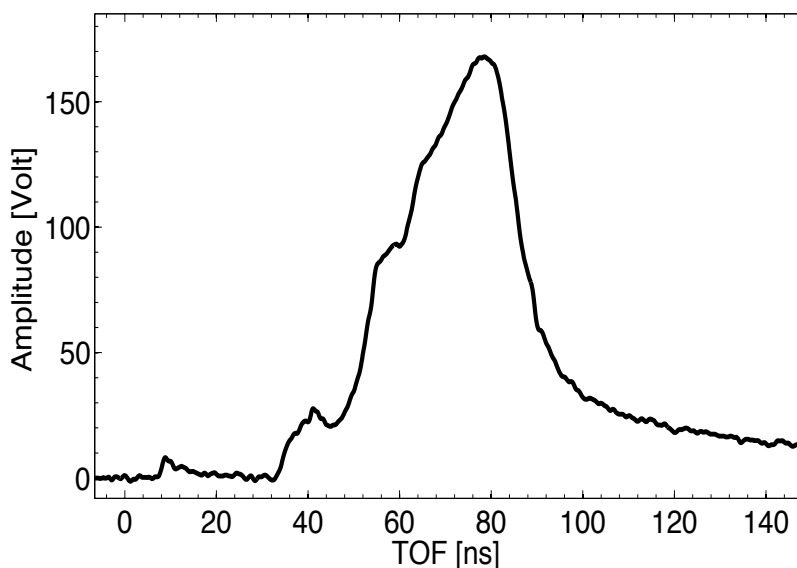


Figure 5.5: TOF signal acquired by the pDD detector at 2.35 m from target in backward direction. No absorbers have been used in this case.

As shown in figure 5.5, the tiny peak corresponding to the so-called photopeak coming from x-rays and fast electrons, triggers the acquisition, a narrow peak and a broader one, respectively, arising from protons and ions accelerated from target, follow according to the time evolution of the ion signal. The TOF signal amplitude results as the overlap of the single ion species signals generated in the detector, therefore it is not possible to directly disentangle the single contribution from the resulting amplitude vs time signal. Figure 5.6 shows a typical image acquired with the image plate (IP). As one can see, proton, carbon

and oxygen ions are accelerated in the following charge states: H^+ , C^{6+} , C^{5+} , C^{4+} , O^{8+} , O^{7+} , O^{6+} .

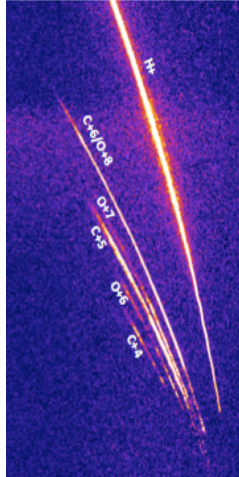


Figure 5.6: Ion trajectories deflected from TP field and detected at the IP plane

The energy spectrum for C^{6+} extracted from figure 5.6 is shown in figure 5.7.

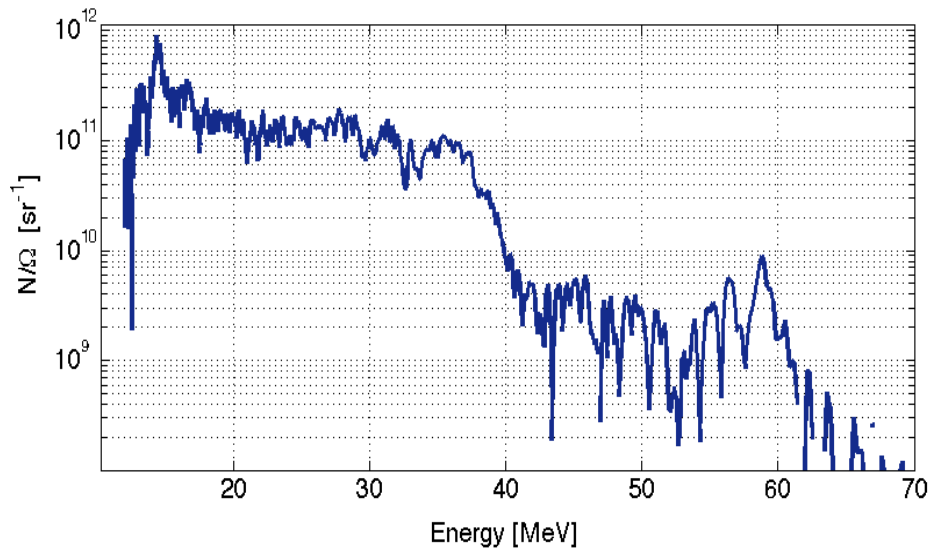


Figure 5.7: C^{6+} energy spectrum reconstructed the TP image.

As one can see, the maximum energy observed for C^{6+} is about 60 MeV, corresponding to a TOF of 76 ns at 2.35 m, i.e. diamond detector flight path. Cut-off energies of each ion

charge states accelerated and extracted from TP analysis together with the corresponding TOF at 2.35 m are listed in table 5.1.

Charge states	Energy cut-off [MeV]	TOF @2.35 m
C ⁶⁺	60 MeV	76 ns
C ⁵⁺	50 MeV	82 ns
C ⁴⁺	30 MeV	107 ns
O ⁸⁺	80 MeV	76 ns
O ⁷⁺	45 MeV	101 ns
O ⁺⁶	39 MeV	108 ns

Table 5.1

The TOF values corresponding to the cut-off energies extracted from the TP analysis for each ion species represent a threshold in the TOF signal indicating a region, in this case identified by TOF value > 76 ns, where proton, carbon and oxygen ions contribute to the total TOF signal amplitude. In such region, it is not possible to disentangle in between the different contributions and reconstruct the energy spectrum for each ion species. On the other hand, for TOF < 76 ns the TOF signal arises uniquely from fast proton contribution, therefore the corresponding proton energy distribution can be obtained, using the analysis procedure discussed in section 4.3.2. Figure 5.8(a) shows the TOF proton signal deconvolution obtained in the TOF time interval between 33 ns and 76 ns, for the shot shown in figure 5.5. Figure 5.8(b) shows the proton energy spectrum extracted by the deconvolution using the formula 4.11.

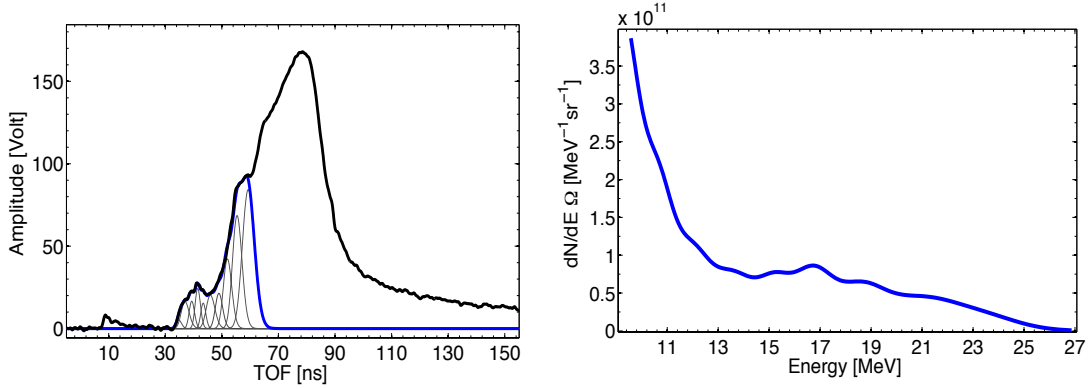


Figure 5.8: a) TOF signal deconvolution in the time interval $33 \text{ ns} < \text{TOF} < 76 \text{ ns}$ for the shot shown in figure 5.5. Ten different MB functions have been used to deconvolve the signal, with v_s ranging from $3.9 \cdot 10^7$ to $6.7 \cdot 10^7$ m/s and a temperature $T \sim 10^8$ K. b) Proton energy spectrum obtained by the deconvolved TOF signal.

As shown in figure 5.8 the maximum proton energy measured in this shot (shot 62) is of $27 \text{ MeV} \pm 0.1 \text{ MeV}$. Then, integrating the energy spectrum in figure 5.8, a number of protons per solid angle in the energy interval between 9.5 and 27 MeV of $2.1 \pm 0.7 \cdot 10^{12}$ p/sr has been obtained. The uncertainties for the maximum energy and the proton/sr have been evaluated applying the error propagation law in formula 4.11 and considering the statistics uncertainty. The error on the energy loss, of the order of 10%, has been estimated with Geant4 simulation taking also into account the energy straggling, whereas an uncertainty on the solid angle of 0.1 % has been evaluated.

A complementary tool useful in the proton energy spectrum reconstruction, is the use of absorbers to put just in front of the detectors; the absorber purpose will be twofold:

- stop the slow heavy ion contribution allowing to determine the minimum energy needed for each accelerated ions to reach the detector and identify the region where ions contribute to the TOF signal
- stop the low-energy proton component, which, due to the low energy high fluxes typical of an exponential TNSA distribution, might saturate the detector.

As an example, figure 5.9 shows the TOF signal acquired by the pDD placed in backward, 2.35 m flight path, and using 50 μm kapton foil absorber.

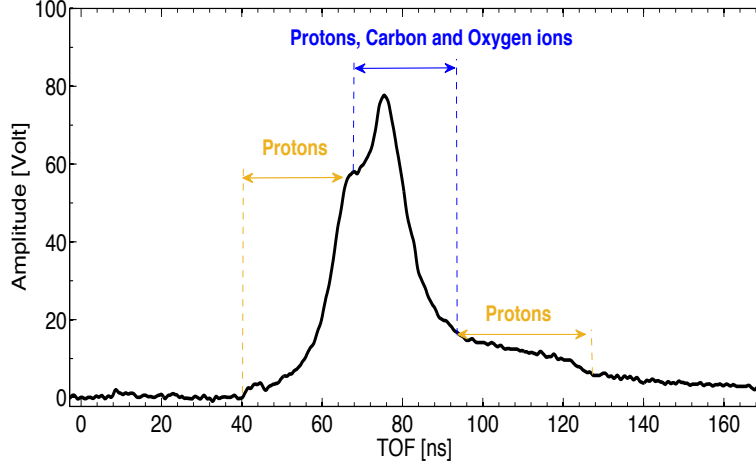


Figure 5.9: TOF signal acquired in backward direction with the pDD, flight path = 2.35 m. A 50 μm kapton foil was used to stop heavy ion contribution and slow protons. Proton and ion contributions in the three different time intervals are shown.

The minimum residual energy detected after the absorber for protons, carbon and oxygen ions and the corresponding TOF @ 2.35 m have been calculated using LISE++ [131] software and are reported in table 5.2.

Ion species	Residual energy [MeV]	TOF @2.35 m
Protons	1.83 MeV	125 ns
C ions	35.6 MeV	98 ns
O ions	47.4 MeV	98 ns

Table 5.2: Values of proton, carbon and oxygen minimum residual energy after the absorber. The corresponding TOF at 2.35 m are also listed.

Coupling together the cutoff energy information obtained from the TP analysis and the energy values selected using the absorber, it is possible to distinguish three time regions in the TOF signal as shown in figure 5.9: 1) the region between 41 ns and 76 ns corresponds uniquely to the high-energy proton contribution; 2) 76-98 ns, in this interval the total

signal results as the sum of proton, carbon and oxygen ion contributions; 3) the interval between 98 ns and 125 ns, the signal is generated by the low-energy proton component down to the TOF corresponding to the residual energy after the absorber. In regions 1 and 3, being protons the only contribution to the TOF signal, it is therefore possible to apply the deconvolution procedure to the signal and extract the energy spectrum, considering the energy loss in the absorber and in the detector thickness itself as explained in section 4.3.2.

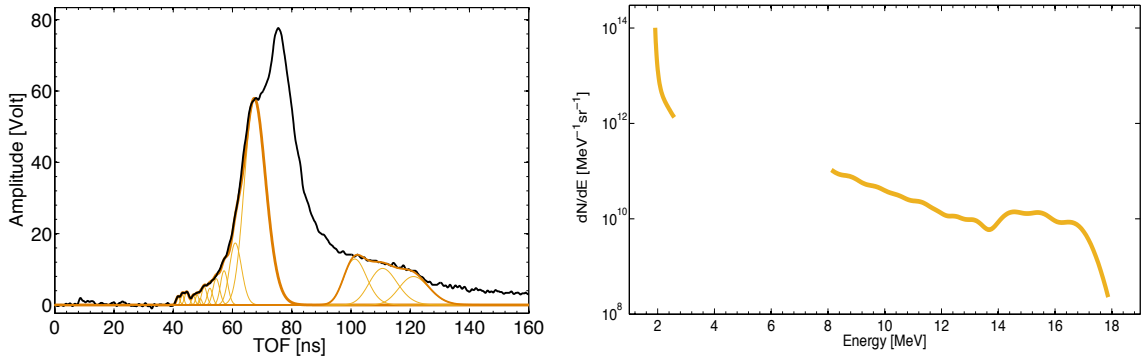


Figure 5.10: a) Deconvolution of the TOF signal shown in figure 5.9 for $40 \text{ ns} < \text{TOF} < 76 \text{ ns}$ and $98 \text{ ns} < \text{TOF} < 125 \text{ ns}$. Fifteen MB functions were used for the fitting procedure, having v_s ranging between $1.9 \cdot 10^7 \text{ m/s}$ (slow protons) to $5.6 \cdot 10^7 \text{ m/s}$ (fast protons) and T from $6 \cdot 10^6 \text{ K}$ to $4 \cdot 10^7 \text{ K}$. b) Proton energy spectrum reconstructed from the TOF signal in the regions 1 and 3.

Figures 5.10a and b show the deconvolution and the energy spectrum obtained for the two energy regions 2-2.5 MeV and 8-18 MeV (corresponding to the TOF region 1 and 3). As one can see from the energy spectrum in fig 5.10b, the decreasing exponential energy distribution, typical of the TNSA acceleration regime, can be clearly observed. Moreover, integrating the energy spectrum, separately, in the two energy intervals the number of proton per solid angle obtained respectively, for high-energy and low-energy proton component, results of $2.3 \pm 0.8 \cdot 10^{11}$ and $5.7 \pm 1.5 \cdot 10^{12}$.

Comparison with TP results

As it has been discussed in section 5.1.2, in order to validate the procedure developed for high energy proton and ion TOF diagnostics, the results have been compared with well established reference diagnostics, for instance TP spectrometer, RCF and CR-39.

A Thomson Parabola was placed in backward direction and the pDD diamond was inserted close to the pinhole at 1.22 m from target. Image plates were used to acquire image of the ion trajectories deflected in the magnetic and electric field shot by shot. A 50 μm thick Al absorber was used to shield the pDD.

The main parameters of the used TP are reported in table 5.3

B field	B length	E field	Electrode length	Pinhole	B-IP
1 T	5 cm	19 kV/cm	15 cm	200 μm	27 cm

Table 5.3: TP parameters.

In order to shield the IP detector from X-rays, the IP has been wrapped with a 80 μm Al foil. Thanks to the IP calibration [143], the energy spectrum can be reconstructed from the TP image for each ion species.

The Al absorber on the pDD stops protons with an energy up to 2.2 MeV, carbon up to 45 MeV and oxygen up to 68 MeV. Following the approach described in section 5.1.2, the TOF signal has been deconvolved for $20 \text{ ns} < \text{TOF} < 35 \text{ ns}$ and $47 \text{ ns} < \text{TOF} < 60 \text{ ns}$ as shown in Figure 5.11 a. Figure 5.11 b shows the corresponding proton energy spectrum reconstructed with the TOF analysis procedure, compared with the one obtained from TP analysis.

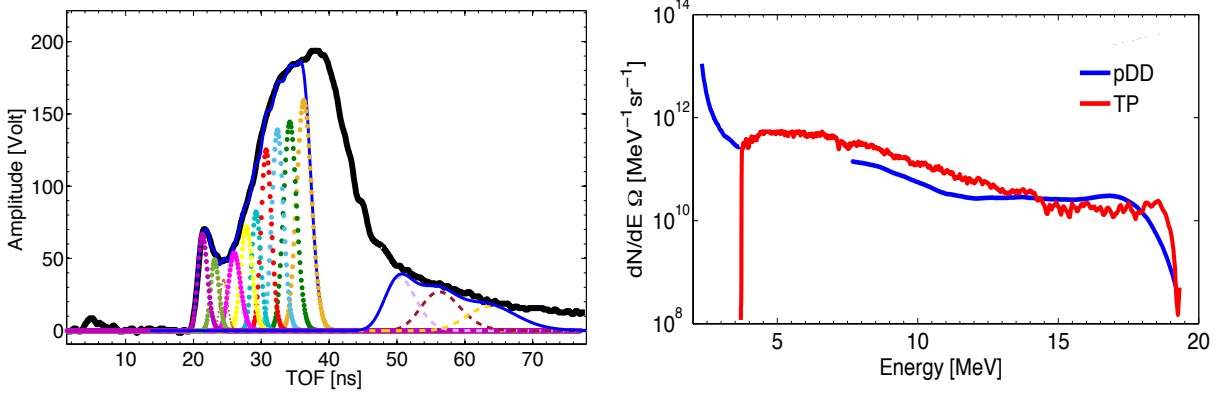


Figure 5.11: a) Deconvolution of TOF signal detected with pDD at 1.22 m from target with 50 μ Al absorber. b) Proton energy spectra obtained with TOF analysis procedure (blue) and TP-IP (red).

As one can clearly see from the comparison in figure 5.11, a rather well agreement between the proton energy spectra obtained with the two complementary diagnostics can be observed. Moreover, integrating the energy spectra in the same energy range, between 10 and 19 MeV, the number of proton per solid angle values obtained from the two spectra have been compared. The results are listed in table 5.4 together with the cutoffs energies for protons measured by pDD and TP, respectively.

Detector	pDD	TP
Cutoff Energy [MeV]	19.4 ± 0.2 MeV	19.2 ± 0.2 MeV
N_p/Ω_{det} [sr^{-1}]	$2.6 \pm 0.6 \cdot 10^{11}$	$3.3 \pm 1 \cdot 10^{11}$

Table 5.4: Proton cutoff energies and N_p/Ω obtained with TOF and TP analysis.

As one can see from the comparison in the table 5.4, results from TOF and TP diagnostics are in quite good agreement considering also the uncertainties associated. The 20 % discrepancy can be explained considering that the TP and the pDD were not exactly placed at the same angle with respect to the target normal direction. Moreover, the stability of the technique has been verified comparing the N_p/sr calculated from TOF diagnostics

using pDD and from the TP spectrometer in the energy interval ranging between 13 MeV and 18 MeV, for 6 different shots. The comparison obtained is shown in figure 5.12. The energy range selected is the only energy region common to all the shots analyzed. The obtained values along with the corresponding uncertainties are listed in table 5.5.

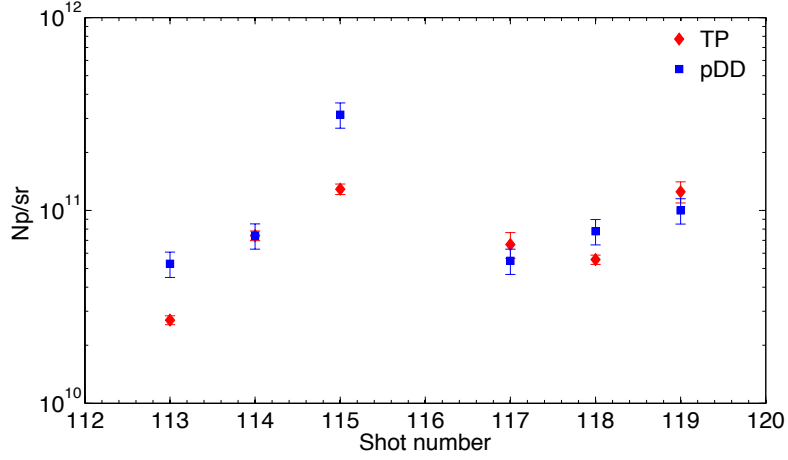


Figure 5.12: Number of protons per solid angle in the energy range 13-18 MeV extracted from the TOF signals (blue solid squares) and TP images (red solid diamonds) for 6 consecutive shots.

Shot	pDD	TP
113	$2.7 \pm 0.3 \cdot 10^{10}$	$5.3 \pm 0.8 \cdot 10^{10}$
114	$7.4 \pm 0.8 \cdot 10^{10}$	$7.4 \pm 1.1 \cdot 10^{10}$
115	$1.4 \pm 0.2 \cdot 10^{11}$	$1.9 \pm 0.3 \cdot 10^{11}$
117	$6.1 \pm 0.7 \cdot 10^{10}$	$5.5 \pm 0.8 \cdot 10^{10}$
118	$4.6 \pm 0.5 \cdot 10^{10}$	$7.8 \pm 1.1 \cdot 10^{10}$
119	$1.2 \pm 0.3 \cdot 10^{11}$	$1.2 \pm 0.2 \cdot 10^{11}$

Table 5.5: Values of N_p/sr values shown in figure 5.12

The uncertainty of the N_p/sr obtained with TOF technique has been estimated considering the error propagation in formula 4.11 as explained in section 5.1.2. The TP result uncertainty was estimated to be about 15%, considering the statistical uncertainty and the one associated to the calibration procedure. A similar comparison has been performed

between the maximum proton energies measured by TOF diagnostics and the TP spectrometer (figure 5.13 and table 5.7).

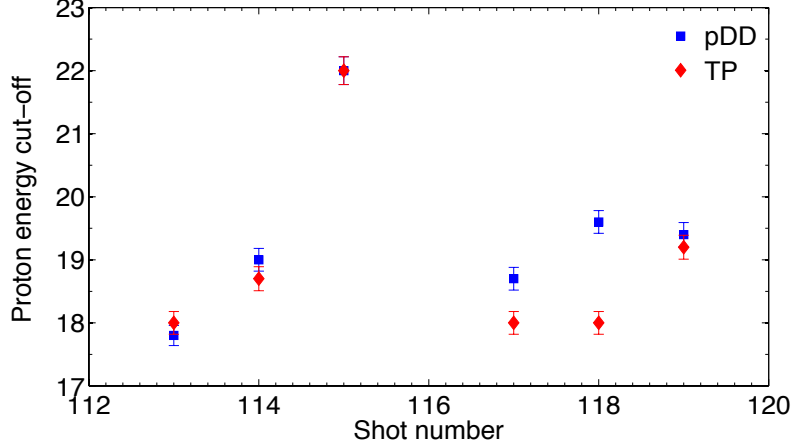


Figure 5.13: Proton energy cutoff measured with TOF technique (blue points) and TP (red point) for 6 consecutive shots.

Shot	pDD	TP
113	17.8 ± 0.2 MeV	18.1 ± 0.2 MeV
114	19.1 ± 0.2 MeV	18.7 ± 0.2 MeV
115	22.1 ± 0.2 MeV	22.1 ± 0.2 MeV
117	18.7 ± 0.2 MeV	18.1 ± 0.2 MeV
118	19.6 ± 0.2 MeV	18.1 ± 0.2 MeV
119	19.4 ± 0.2 MeV	19.2 ± 0.2 MeV

Table 5.6: Measured proton energy cutoffs shown in figure 5.13

As one can see from the comparison in figure 5.12 and 5.13, the TOF results are in good agreement with the ones obtained with the TP, although both diagnostics are sensitive to the shot to shot fluctuation effect on the N_p/sr and energy cutoffs, due to the different laser-plasma interaction (i.e. laser energy on target, pulse duration, contrast etc.). This result indicates a good reproducibility of the TOF technique and validates the procedure

developed to extract the proton energy spectrum of high-energy laser driven proton beams, confirming the TOF technique as a reliable tool for the diagnostics of such kind of beams.

Comparison with RCF analysis

Radio Chromic Films (RCF), EBT3 type[105], have been used in stacks to measure the proton energy spectrum in backward direction and the results have been compared with the TOF ones. In particular, an RCF stack consisting of 10 layers was placed at 1.22 m from target together with the pDD and close to the TP pinhole. The images acquired are shown in figure 5.14.

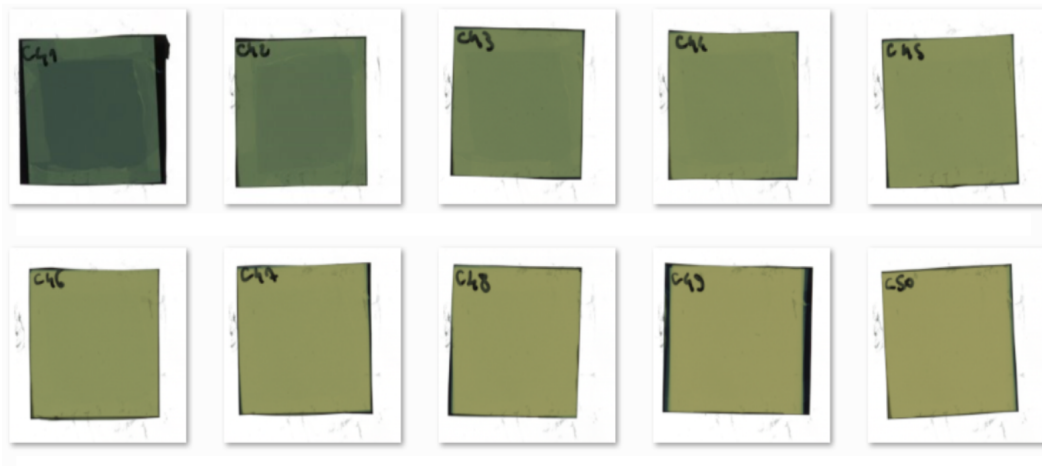


Figure 5.14: RCF stack C41-C50 placed at 1.22 m from target in backward direction shielded by 500 μ m thick Al foil.

A 500 μ m thick Al foil was used to shield the RCF stack from x-rays, to stop protons up to 8.76 MeV and C ions up to 126 MeV. The Al absorber assures, therefore, that the dose deposited in the RCF stacks is only due to the proton contribution. Due to the EBT3 structure [144], such kind of RCF is particularly sensitive to delivered dose and it is typically used in the dose range between 0.25 and 10 Gy. The procedure to retrieve the proton energy spectrum from RCF stacks consists of three main steps:

- In transmission scanning the RCF with a flatbed color scanner to acquire raw images of irradiated films.

- Optical density-dose conversion. A dose calibration of the RCF can be performed in order to convert the observed blackening of irradiated RCF, measured through the optical density, in dose. The calibration is, indeed, typically obtained irradiating the RCFs with given dose values and measuring the corresponding optical densities. In such way a calibration curve, dose vs optical density, is constructed and can be used for the same RCF type and lot, to directly measure the dose released from incident beam in other experiments.

In particular, the RCFs used for the experiment at RAL, have been calibrated with 62 MeV proton beams at CATANA protontherapy facility (INFN-LNS).

- Energy spectrum reconstruction. Once the optical density is converted in dose for each RCF layer, the total energy deposited from protons per unit of depth for each RCF can be calculated integrating the dose and multiplying for the active layer density. The position of each RCF within the stack identifies a certain energy range of protons in water. The proton energies corresponding to a given RCF layer of the stack, shown in figure 5.14, and obtained considering the 500 μm Al absorber are reported in table 5.7.

RCF	Energy [MeV]
C41	9.77 MeV
C42	11.4 MeV
C43	12.85 MeV
C44	14.15 MeV
C45	15.35 MeV
C46	16.5 MeV
C47	17.55 MeV
C48	18.6 MeV
C49	19.55 MeV
C50	20.5 MeV

Table 5.7: Proton energy values corresponding to each RCF of the stack C41-C50.

The number of protons corresponding to the delivered dose in a given layer, and hence in a given energy range, can be extracted for each of the RCF composing the stack, using an iterative procedure.

The proton energy spectrum obtained with such procedure for the stack shown in figure 5.14, is shown in figure 5.15.

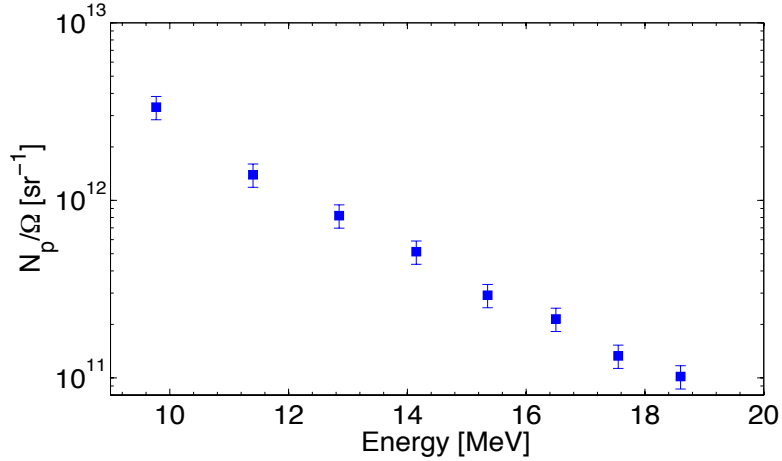


Figure 5.15: Energy spectrum obtained from the C41-C50 RCF stack.

The uncertainties on the number of protons per sr, is about 15%, and have been estimated considering the uncertainty deriving from dose calibration, from the iterative reconstruction procedure and from statistical error.

A comparison between the energy spectrum and N_p/sr resulted from RCF spectroscopy and TOF diagnostics has been performed. Figure 5.16 shows the comparison between the energy spectra extracted from the pDD signal (orange closed squares) and RCF (blue closed circles) in the energy range [13-19 MeV] for the same shot. The two diagnostics were placed at the same distance from target and also almost at the same angle. As one can clearly see, the results are in good agreement, although the discrepancy increases at lower energies: such discrepancy can be explained considering that in the TOF procedure, in order to assure that the TOF signal analyzed originates only by protons and exclude ion contribution, a sharp cut on the TOF signal is applied, causing a possible underestimation

of the total number.

The N_p/sr for RCF and TOF diagnostics have been obtained integrating figure 5.16 in the energy range [13-19 MeV] and is reported in table 5.8.

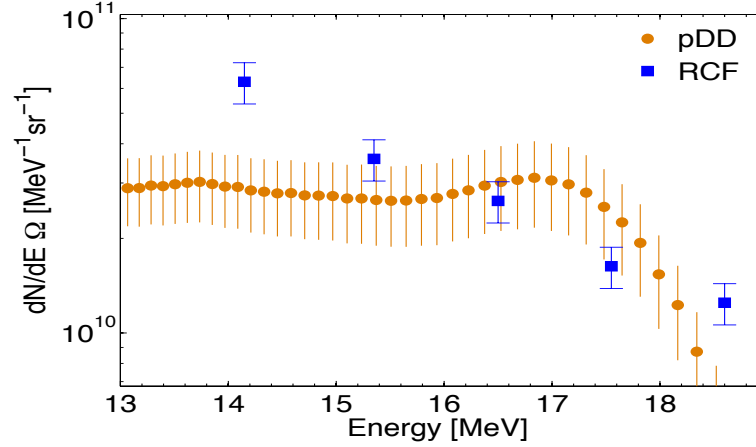


Figure 5.16: Comparison of proton energy spectra retrieved with TOF technique (orange closed circles) and RCF procedure (blue closed squares) in the energy range from 13 up to 19 MeV.

	pDD	RCF
$N_p/\Omega_{det} [sr^{-1}]$	$1.2 \pm 0.3 \cdot 10^{11}$	$1.3 \pm 0.2 \cdot 10^{11}$

Table 5.8: Number of protons/sr in the energy range 13-19 MeV measured with the pDD and the RCF.

A discrepancy of about 7% between the numbers obtained with the two diagnostics is observed, confirming the good agreement.

Comparison with CR-39 results

Nuclear track detectors CR-39 have been also used as reference detector to validate the developed TOF procedure.

5.1. TEST WITH HIGH-ENERGY LASER-DRIVEN ION BEAMS

CR-39 detectors are sensitive to single particle detection, in particular, each particle, releasing energy in the material, creates a damage in the detector structure resulting in craters visible with a microscope after a chemical etching procedure.

In order to stop the ion component and discriminate different proton energy components, different thicknesses absorber foil were used. In particular, during the experiment a 5×2 cm CR-39 was placed at 1.22 m from the target close to the diamond detector pDD, with 6 different Cu thicknesses as shown in figure 5.16. The thicknesses used for the Cu absorber together with the corresponding minimum proton and carbon energies required to traverse each Cu thicknesses are shown in figure 5.16.

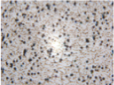
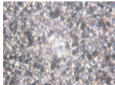
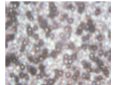
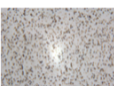
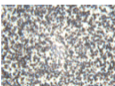
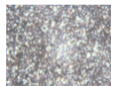
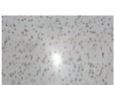
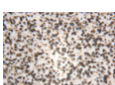
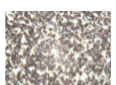

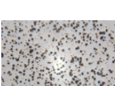
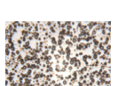
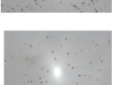
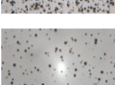

C cut-off	p cut-off	Cu thickness	ETCHING TIME		
			1h	2h	3h
41 MeV/n	23 MeV	1000 μm	NO TRACKS		
4.5 MeV/n	2.5 MeV	25 μm			
10 MeV/n	6 MeV	100 μm			
15 MeV/n	8 MeV	175 μm			
18 MeV/n	10 MeV	250 μm			
27 MeV/n	15 MeV	500 μm			

Figure 5.17: The figure shows the copper thicknesses used to stop protons and ions in the CR-39 detectors. On the left side the minimum proton and carbon energies required to traverse each Cu absorber are reported. On the right side the pictures of each CR-39 areas, observed with a microscope, for three different etching times are shown.

The track characteristics, such as the size, depend on etching procedure parameters: chem-

ical solution composition, concentration, temperature and time. For the CR-39 analysis a 6.25 NaOH etching solution at 70 °C was used. In particular, the crater diameters typically grow with increasing the etching time. In order to select the appropriate etching time and avoid the overlapping of the closest tracks (saturation effect) and at the same time observe also high energy proton tracks typically characterized by very small diameters, three etching times were investigated. The etched tracks are then observed using an optical inverted microscope, picture with an area of $185 \mu\text{m} \times 139 \mu\text{m}$ have been taken and analyzed with IMAGE J software. As shown in figure 5.16, 1, 2 and 3 hour etching times have been considered and images for each CR-39 area are shown for each etching time. As one can clearly see, the high number of low-energy protons together with the track widening with the etching time, cause the overlapping of the closer craters, which makes the analysis very difficult. For this reason, the analysis has been performed uniquely in the CR-39 areas with thicker absorber, in which high-energy ($> 15 \text{ MeV}$) proton tracks are well visible and separate. Moreover, since high-energy protons traverse not only the absorber but also the CR-39 thickness itself, the analysis of the CR-39 backside has been also performed in the regions corresponding to $200 \mu\text{m}$ and $500 \mu\text{m}$ thick copper absorber. Being the CR-39 1 mm thick, the corresponding proton energy cut-offs in such case, are respectively, 15 MeV and 19 MeV. The images acquired from the CR-39 backside corresponding to these absorber thicknesses are shown in figure 5.18.

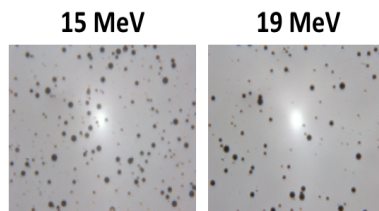


Figure 5.18: Pictures of the backside of irradiated CR-39 with $200 \mu\text{m}$ (left) and $500 \mu\text{m}$ thick Cu foil.

The comparison between the CR-39 data and TOF results have been obtained, integrating the energy spectrum extracted from TOF signal in the energy range $>15 \text{ MeV}$ and >19

MeV. Figure 5.19 and table 5.9 show the comparison between the results obtained. Data in figure 5.9 represent the number of protons per solid angle with energy higher than 15 MeV and 19 MeV obtained with the two diagnostics. The uncertainties on the CR-39 track number have been obtained considering the statistical uncertainty and the systematic uncertainty, resulting of the order of 25%.

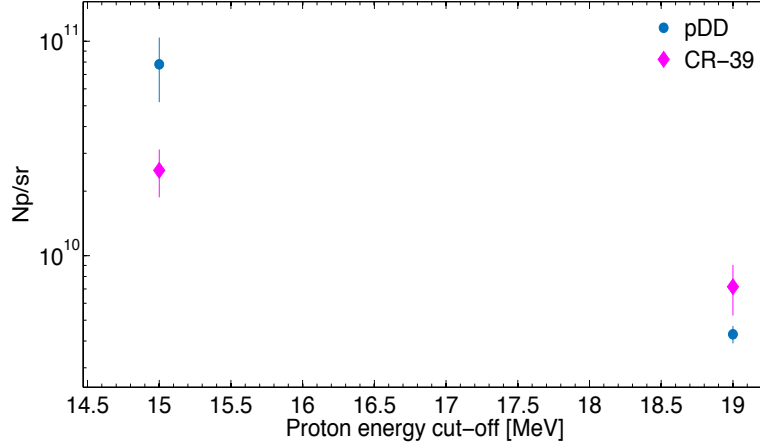


Figure 5.19: Comparison between TOF (blue circles) and CR39 (magenta diamonds) results.

	pDD	CR-39
$Np/\Omega_{det} [sr^{-1}] [>15 \text{ MeV}]$	$7.8 \pm 2.6 \cdot 10^{10}$	$2.5 \pm 0.6 \cdot 10^{10}$
$Np/\Omega_{det} [sr^{-1}] [>19 \text{ MeV}]$	$4.3 \pm 0.4 \cdot 10^9$	$7.1 \pm 1.9 \cdot 10^9$

Table 5.9: Number of protons/sr in the energy ranges >15 MeV and >19 MeV measured with the TOF diagnostics and the CR-39 detectors

As one can see from figure 5.19, proton number obtained with CR-39 analysis for the energy range >15 MeV is slightly less than the one extracted from TOF signal. This underestimation can be explained looking at figure 5.18: some of the tracks are indeed overlapped; therefore they have been excluded from the final counting by the software. Moreover, CR-39 were placed at the same distance from the target with respect to the TOF detector, but at slightly different height, about 10 cm with respect to the detector,

which might explain the lower particle flux detected. On the other hand, a good agreement is observed for the number of protons with an energy higher than 19 MeV obtained with the two diagnostics: in such case, the lower flux, and the small track diameters of high-energy protons allow to disentangle the tracks in the CR-39 without overlap, avoiding the underestimation of the total number of craters observed in the CR-39.

Comparison between pDD and sDD TOF signal

Once the technique and the analysis procedure have been validated with reference diagnostics, TP, RCF and CR-39, a comparison between the results obtained with two different diamond detectors using the TOF method has been also performed. In particular, in the experiment, two different kinds of diamond detectors have been used as described in section 5.1.1, a 100 μm thick polycrystalline (pDD) and a 500 μm thick single crystal diamond detector (sDD).

A comparison for some shots acquired with the two detectors placed in backward direction at 4.10 m far from the target at about 10° with respect to target normal direction, will be shown. A 50 μm Al absorber has been used on the pDD, in order to cut protons up to 2.2 MeV and carbons up to 45 MeV; the sDD was provided with a 100 μm thick Al foil in order to stop protons up to 3.4 MeV and carbons up to 72 MeV. Moreover, a long flight path allows to disentangle different beam components with higher resolution with respect to a short flight path and explore different detector advantages and limits. The TOF signals acquired with the pDD and the sDD are, respectively, shown in 5.20a and 5.21a.

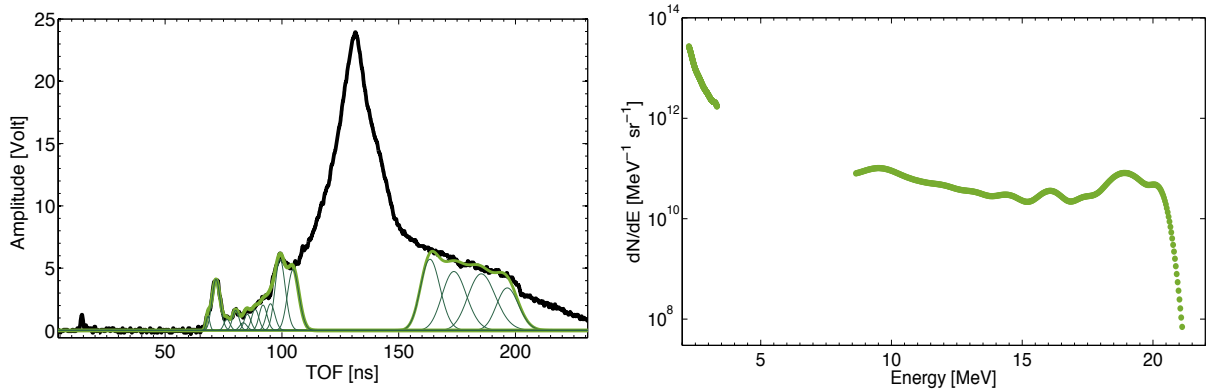


Figure 5.20: a) TOF signal acquired with pDD in backward direction, flight path=4.10 m. The deconvolution procedure has been performed for $66 \text{ ns} < \text{TOF} < 123 \text{ ns}$ and $152 \text{ ns} < \text{TOF} < 200 \text{ ns}$. b) Proton energy spectrum extracted from the TOF regions analyzed.

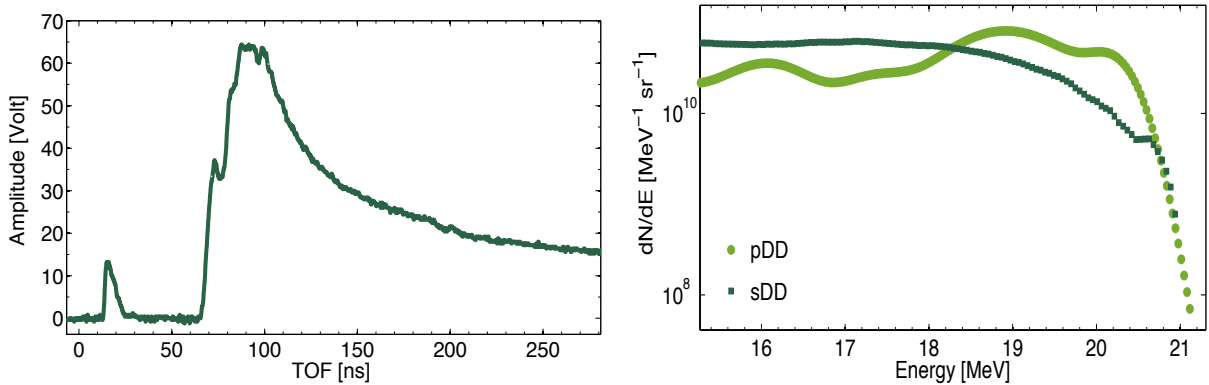


Figure 5.21: a) TOF signal acquired with sDD in backward direction, flight path= 4.10 m. b) Comparison of proton energy spectra obtained from pDD (light green circles) and sDD (dark green squares) in the energy range between 15 MeV and 21 MeV.

The pDD signal shows, apart a short photopeak, three peaks in the time region between 66 ns and 200 ns: the two peaks in the time interval between 66 ns and 123 ns originate only from fast protons and the third peak in the time interval $123 \text{ ns} < \text{TOF} < 200 \text{ ns}$ arises from both ion and slow proton contributions. A deconvolution of the TOF signal shown in figure 5.20, can be performed for $66 \text{ ns} < \text{TOF} < 123 \text{ ns}$ and $152 \text{ ns} < \text{TOF} < 200 \text{ ns}$ and the energy spectrum can be extracted as shown in figure 5.20b. On other hand, the sDD

signal shown in figure 5.21, since ions are completely stopped in the 100 μm Al foil, is due only to protons whose energy is sufficient (more than 3.4 MeV) to traverse the absorber. Nevertheless, the long tail observed for TOF higher than about 100 ns in figure 5.21a, which could be generated from saturation effects of the detector itself, cannot be associated to a physical signal originated by proton impinging on the detector at those large TOF.

For this reason, the sDD signal has been analyzed considering the time interval $66 \text{ ns} < \text{TOF} < 77 \text{ ns}$ corresponding to first narrow peak, i.e. high energy protons (15-21 MeV). The comparison between energy spectra obtained with pDD (light green circles) and with sDD (dark green squares) in the overlapping energy range between 15 and 21 MeV is shown in figure 5.21b. Table 5.10 lists the number of protons/sr obtained considering such energy range in the both spectra.

pDD	sDD
$1.7 \pm 0.5 \cdot 10^{11}$	$2.4 \pm 0.2 \cdot 10^{11}$

Table 5.10: Number of protons/sr in the energy range 15-21 MeV measured with the pDD and the sDD

As shown in figure 5.21 and listed in table 5.10, despite the different characteristics of the pDD and sDD detector, such as the thickness as well as the time response and resolution (section 4.2), the proton energy spectra reconstructed from the two measured TOF signals, as well as the total number of proton per solid angle extracted in the energy range between 15 and 21 MeV, are in good agreement, confirming the reliability of TOF technique for laser-driven proton beam diagnostics.

5.1.3 Analysis and results of TOF signals acquired in forward direction

In order to validate the TOF method and developed analysis procedure also for higher proton energy detection, diamond detectors were placed on the rear side of the target

direction (forward direction), where particles are expected to be accelerated up to an higher energy cut-off with respect to the backward direction. The scheme of the experimental setup is shown in figure 5.22.

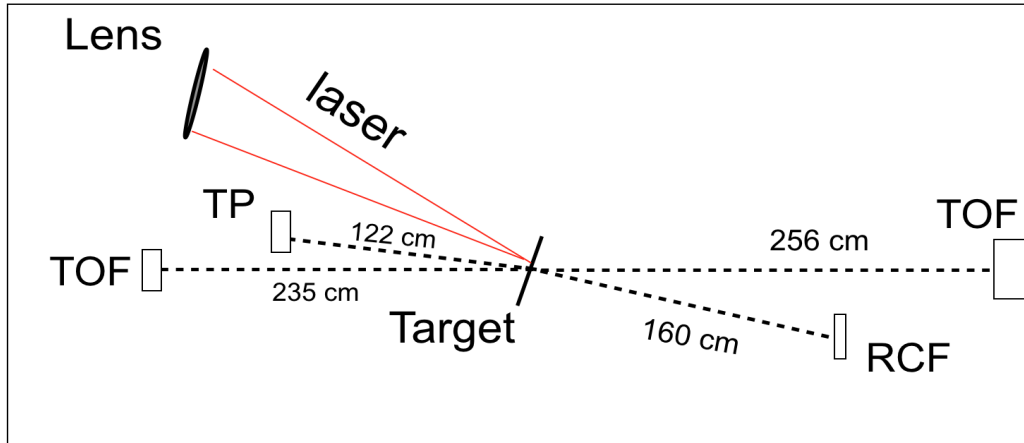


Figure 5.22: Experimental set-up used in forward direction.

The pDD was placed in forward direction at 2.56 m from the target and about 10° with respect to the target normal direction; the sDD and the TP were placed, to provide a reference, in backward direction respectively, at 2.35 m and 1.22 m from the target. Moreover, a RCF stack was placed along the target normal at 1.6 m from the target in order to measure the maximum proton energy along the beam axis. The proton energy spectrum measured in forward direction with the RCF stack is shown in figure 5.23, showing a maximum proton energy of about 40 MeV along the target normal.

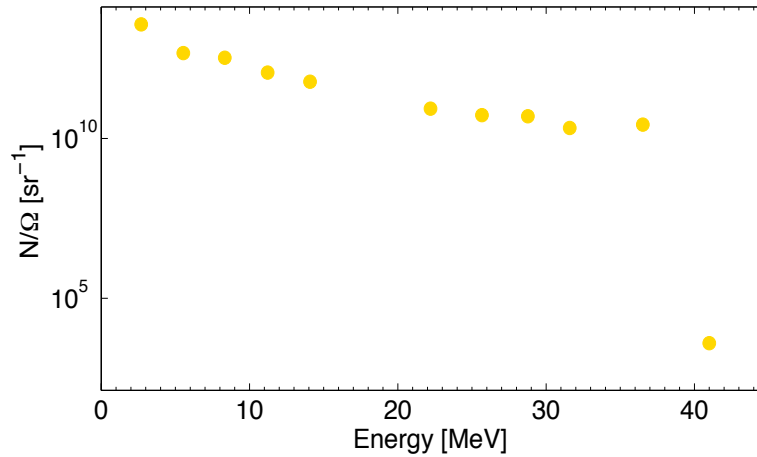


Figure 5.23: Proton energy spectrum measured with the RCF stack placed in forward direction.

The TOF signal acquired by the pDD, using a 50 μm Al foil, in forward direction at 2.56 m is shown in figure 5.24.

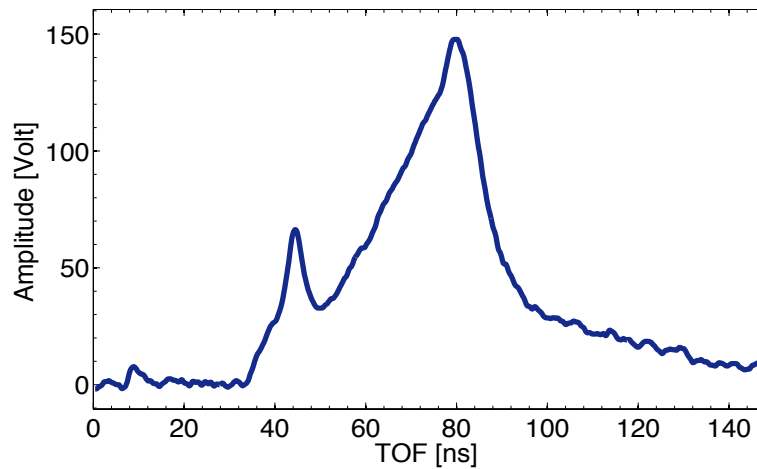


Figure 5.24: TOF signal acquired with the pDD at 2.56 m from target in forward direction.

As typical TOF spectrum has been observed in figure 5.24: a tiny photo-peak is visible and followed by a narrow peak (33-50 ns) and a broader bump (50-120 ns), coming from protons and ions. The proton energy cut-off measured from the TOF signal is 33 MeV. The discrepancy in the measured cutoff energies with TOF and RCF diagnostics, can be mainly

attributed to the different angular position of the RCF stack with respect to the pDD. Indeed, since the RCF stack is placed along the target normal direction, might detect the higher energy proton component, according to TNSA acceleration regime. Nevertheless, the RCF analysis does not provide information about accelerated ion species and their maximum energies, useful to analyze the TOF signal, identifying the TOF region coming only from protons. However, by taking into account the analysis of the diagnostics placed in backward direction some important assumptions can be done to analyze the TOF signal in forward direction. The analysis of the sDD signal, shown in figure 5.25, and the TP images, acquired during the same shot of the signal shown in figure 5.24, provide measurement of the proton energy spectrum and cutoff energy in backward direction (20 MeV measured from both diagnostics), as one can see from figure 5.25 that shows a comparison between the sDD (dark green diamonds) and TP (red closed circles) energy spectra in the same energy range [16-20] MeV. Moreover, the analysis of the C^{6+} charge state parabola in the TP-IP allowed to obtain the carbon energy spectrum (figure 5.26) along with cutoff energy of about 60 MeV.

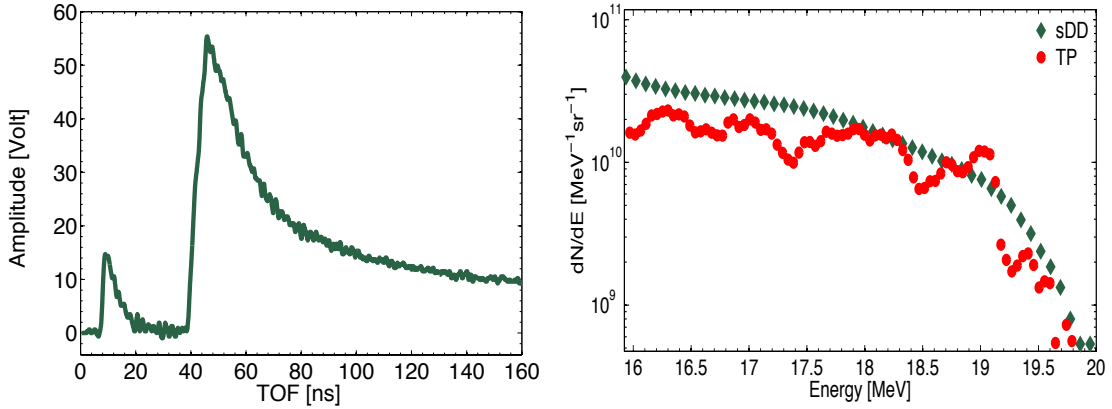


Figure 5.25: a) sDD TOF signal retrieved in backward direction. b) Proton energy spectra in the energy range 16-20 MeV obtained from sDD and TP signal analysis.

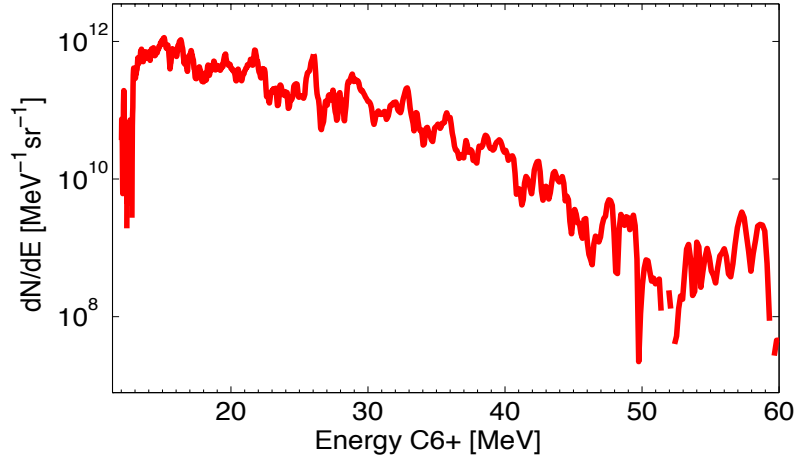


Figure 5.26: C^{6+} energy spectrum extracted from TP analysis.

According to further experiments carried out with the Vulcan PW laser at RAL, where similar targets have been used (private communication), in which carbons, with an energy not higher than 150 MeV, have been observed in forward direction, it can be assumed that the narrow peak between 33 ns and 45 ns shown in figure 5.24 is originated only from high-energy proton contribution. Consequently the corresponding proton energy spectrum can be properly obtained as shown in figure 5.27b.

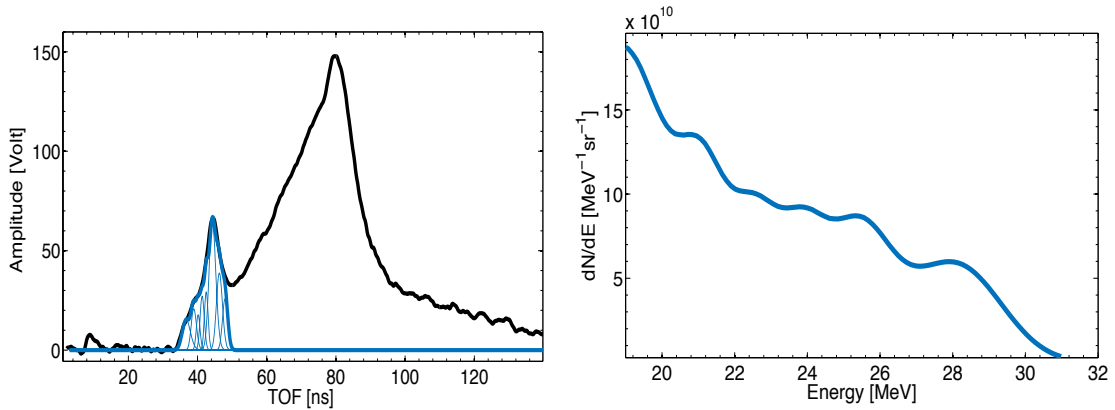


Figure 5.27: a) Deconvolution of the fast proton narrow peak in the TOF signal interval between 33 ns and 45 ns shown. Values for v_s range from $5.3 \cdot 10^7$ m/s to $1 \cdot 10^7$ m/s and for temperature $\sim 10^7$ K. b) Energy spectrum reconstructed from the TOF deconvolution of the signal shown in a).

A comparison between numbers of protons/sr measured in backward and forward direction in a common energy range has been also performed. Energy spectra obtained with sDD and TP, in backward direction, and pDD and RCF stack, in forward direction, have been integrated in the energy interval [16-20] MeV. The obtained values for different diagnostics are reported in table 5.11; the number of protons accelerated in forward direction results about one order of magnitude higher than the one measured in backward direction, as it can be expected considering the higher acceleration efficiency from the target rear side, typically characterizing the TNSA acceleration regime.

sDD (back)	TP (back)	pDD (fwd)	RCF (fwd)
$6.8 \pm 0.3 \cdot 10^{10}$	$4.3 \pm 1.3 \cdot 10^{10}$	$6.4 \pm 1.6 \cdot 10^{11}$	$9.7 \pm 1.4 \cdot 10^{11}$

Table 5.11: Number of protons/sr in the energy range 16-20 MeV measured with the sDD and the TP placed in backward direction (back) and with pDD and the RCF stacks placed in forward direction (fwd).

The comparison of TOF analysis with the reference diagnostics, TP, RCF and CR-39, shown in sections 5.1.2, 5.1.2 and 5.1.2, as well as the comparison between the different used diamonds detectors shown in section 5.1.2, are all in good agreement. The results obtained in forward direction allowed to verify the reliability of TOF technique, and in particular of the method developed to reconstruct the energy spectrum of high-energy particles described in section 4.3.2. Furthermore, the excellent time resolution and response of diamond detectors allowed to detect high-energy proton component also at short flight path; this fact demonstrates that such kind of detectors are particularly suitable for the beam diagnostics along the ELIMED beam line, where high-energy protons, up to 60 MeV, are expected to be accelerated and detected also at a short flight path (2 m).

5.2 Test with laser-driven proton beams along a compact transport beam line

A test experiment with laser-driven proton beams has been carried out using the high repetition rate, less than 1 Hz, laser system ATLAS, able to deliver 3.6 J on a short pulse of 30 fs, and the compact transport beam line installed at the Max-Planck-Institut für Quantenoptik in Garching [37].

The main purpose of the experiment was to demonstrate the possibility to use TOF-based diagnostics for real-time energy and flux measurement of focused and selected proton beams provided by a transport beam line. In particular, in view of the forthcoming installation of the TOF-based diagnostics along the high-power high repetition-rate ELIMAIA beam line, this experiment has made possible to investigate the capability of TOF technique to monitor online the beam transported through different magnetic elements and to provide crucial information for transport optimization, using a high repetition rate laser. The compact transport beam line available at the ATLAS facility consists of a focusing section, composed by two permanent magnet quadrupoles (PMQs), and an energy selection part, consisting of a 10 cm length permanent magnet dipole with a constant magnetic field around 150 mT, as shown in figure 5.28. PMQ system is based on a Halbach array structure, providing a magnetic gradient of 330 T/m and a maximum magnetic field of 1.3 T in a 6 mm diameter bore. PMQ system was provided with a remote controlled moving system in order to vary the relative quadrupole position according to the different energy to be focused.

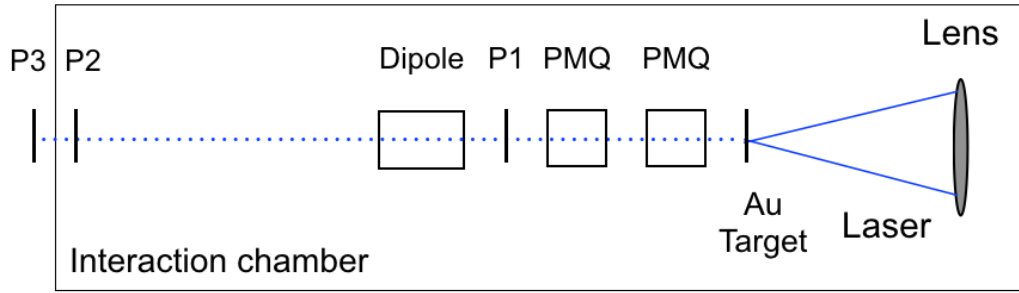


Figure 5.28: Experimental set-up.

As shown in figure 5.28 three diagnostics points have been set up along the beam line:

- P1 corresponding to a 44 cm flight path, downstream the quadrupoles
- P2 at 132 cm from the target, after the dipole
- P3 at 158 cm from target, in air about 1 cm downstream a 50 μm exit kapton window

In the experiment two detectors have been used (figure 5.29):

- D2: the 100 μm thick polycrystalline diamond detector supplied by CIVIDEC described in 4.2. It has been placed both in the position P1 and P2.
- D3: the 500 μm thick single crystal diamond detector supplied by CIVIDEC described in 4.2. It has been placed in the position P3.

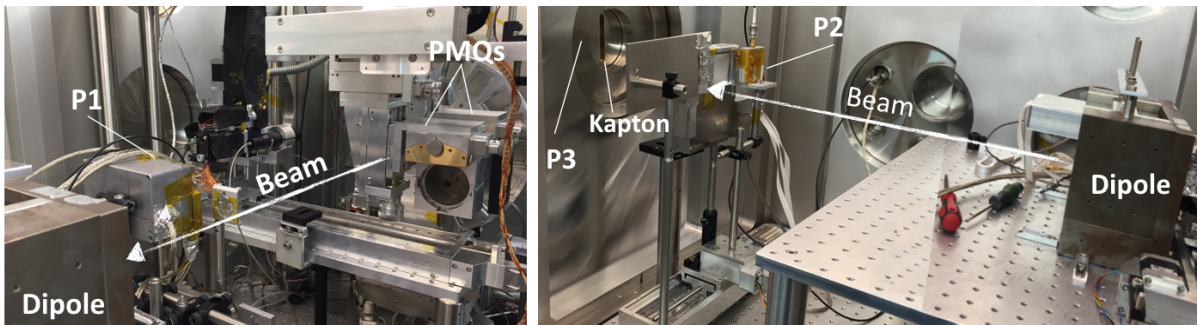


Figure 5.29: Pictures of the different employed detectors along the beam axis in the established positions P1, P2, P3.

5.2.1 Results

The TOF signal of the laser-driven proton beam generated by a 500 nm thick Au target has been measured at a 44 cm flight path (P1 position) with no PMQ system, in order to measure the energy spectrum of the optically accelerated beam. A 6 μm Al foil has been used to stop protons up to 530 keV, carbon ions up to 6 MeV and gold ions up to 34 MeV. Figure 5.30a shows the TOF signal acquired with D2 placed in the position P1 and the corresponding proton energy spectrum obtained using the method discussed in section 4.3.2 (figure 5.30b).

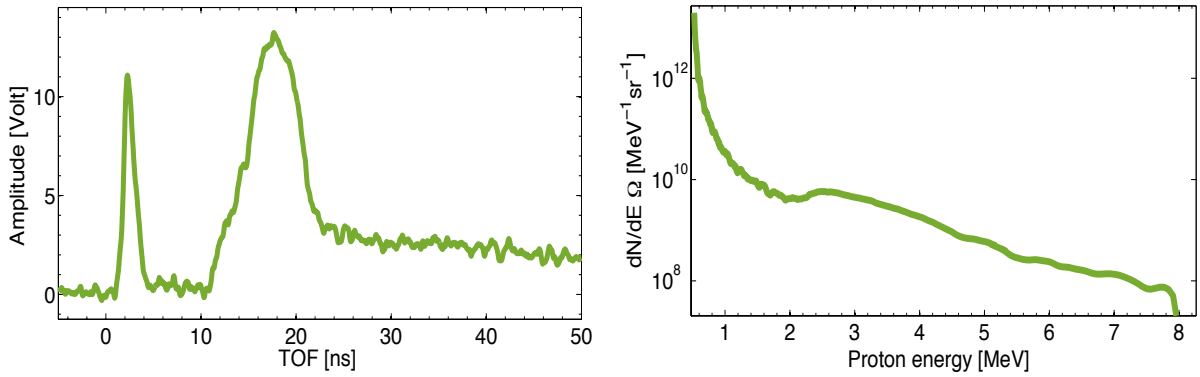


Figure 5.30: a) TOF spectrum acquired with D1 in position P1 without PMQs focusing system and b) corresponding proton energy spectrum.

According to several experiments carried out with ATLAS laser system and with similar target structure (private communication), no carbons with energy higher than 6 MeV are expected. Therefore, the TOF signal shown in figure 5.30a can be attributed uniquely to proton contribution and the proton energy spectrum can be extracted as shown in figure 5.30b. A typical exponential decreasing proton energy distribution with an energy cut-off of 8 MeV can be clearly observed.

The PMQs focusing system was set up, according to the optics study, in order to focus 7 MeV proton beam on the detector D2 placed in position P1. In order to verify the focus position with respect to the detector position P1 and check also the detector alignment, an EBT3 gafchromic film (RCF), placed in front of the detector, has been irradiated. The

RCF is shown in figure 5.31.



Figure 5.31: RCF-EBT3 irradiated in position P1 after PMQs set to focus 7 MeV protons at 44 cm from the target.

Indeed, a typical *cross-like* shape resulting from the optics envelope of permanent magnets [145] can be observed in figure 5.31. The focus spot size, corresponding to the region with higher particle density, is about 2 mm (both in x and y direction). Therefore, the 2 mm diameter D2 detector placed in the focal position can detect the focused beam component, not being affected by the defocused beam.

Figure 5.32 shows the TOF signal acquired with D2 placed downstream the PMQs set to focus 7 MeV protons on the detector. In order to investigate the PMQ focusing effect on the TOF distribution detected (figure 5.32), as well as on the energy spectrum (figure 5.33), the TOF signal, acquired by the D2 using the PMQs in position P1 is shown, together with the signal acquired by D2 without the focusing system in the same position P1.

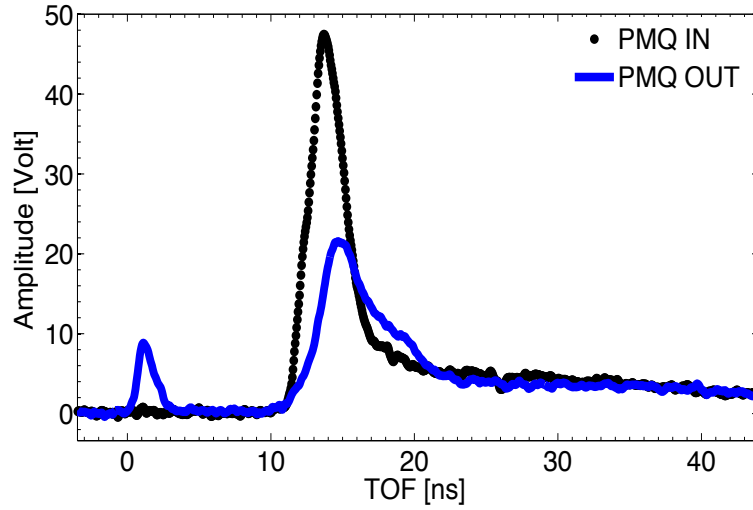


Figure 5.32: Comparison between the TOF signals acquired by D2 in position P1, without using the PMQs (blue line) and with the PMQs (black circles).

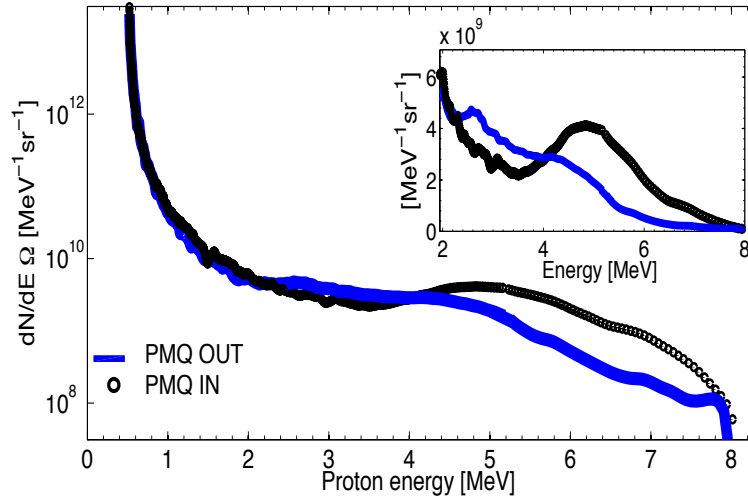


Figure 5.33: Proton energy spectra corresponding to the TOF signals shown in figure 5.32.

As one can see from fig. 5.32 and 5.33, the proton energy distribution is strongly affected by the PMQs focusing effect. In particular, the proton energy spectrum, measured using the PMQs system, clearly shows a peak (inset in Fig. 5.33) indicating a narrow bandwidth compared to the typical exponential energy spectrum obtained measuring without the PMQs. Moreover, considering the beam shape shown in the RCF of figure 5.31, the

PMQs system is able to focus the 7 MeV proton energy component on the detector surface, resulting in a higher signal, i.e. higher fluence, in the corresponding TOF interval, $11 \text{ ns} < \text{TOF} < 15 \text{ ns}$. In table 5.12, are listed, the number of protons/sr in the energy range between 4.5 and 8 MeV ($11 \text{ ns} < \text{TOF} < 15 \text{ ns}$) measured by D2, without and with PMQs, obtained integrating the energy spectra in figure 5.33. The comparison shows a boost in the number of protons/sr with the PMQs with respect to the non-focused beam.

D1 PMQ OUT	D1 PMQ IN
$1.79 \pm 0.2 \cdot 10^9$	$7.8 \pm 0.7 \cdot 10^9$

Table 5.12: Number of protons/sr in the energy range 4.5-8 MeV measured with the D2 in the position P1, without (PMQ OUT) and with (PMQ IN) the focusing PMQs.

The measured TOF signal, due both to the detector area and the peculiar beam focus spot shape and size, is extremely sensitive to the focus conditions, and can provide an on-line monitoring of the beam transport condition. In order to explore such sensitivity, D2 positions has been varied in 2 mm steps to find the optimal focus condition on the detector, in terms of energy and transmission.

Figure 5.34 shows D2 TOF signals acquired, in P2 position with the PMQs, changing the transversal position in 2 mm step. As it can be observed in figure 5.34, proton energy cut-offs, energy spectra, as well as signal amplitude, i.e. particle flux, change, and in particular decrease moving the detector further away from the focal position, confirming that the initial position is indeed optimized with respect to the beam focus conditions.

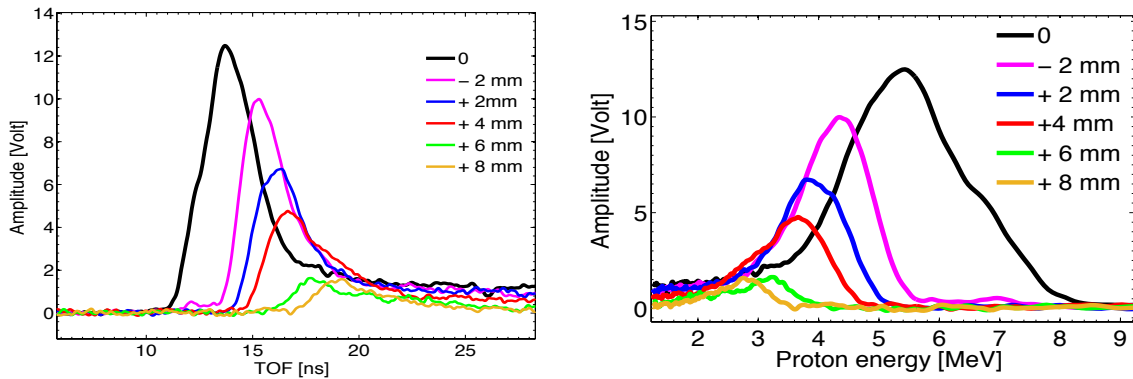


Figure 5.34: a) TOF signals acquired with D2 by changing its transversal position in 2 mm step. b) Kinetic energy corresponding to TOF signals on the right.

Detector D2 has been also placed behind the permanent magnet dipole in order to measure the 7 MeV beam component and its bandwidth selected by using both PMQs and dipole. Considering the dipole setup, particles were vertically deflected by the dipole according to their mass and kinetic energy. Therefore, moving the detector in the vertical direction and placing it at a given height, a certain energy component can be detected. As an example, figure 5.35 shows the TOF signal acquired with D2 placed behind the dipole, position P2, at the height corresponding to about 7 MeV proton deflection. The TOF signal acquired in position P1, corresponding to the PMQ focal position, is also shown in figure 5.35. In order to directly compare the TOF distributions, in spite of the different flight paths, the TOF signals shown in figure 5.35 have been normalized at 44 cm flight path, i.e. position P1.

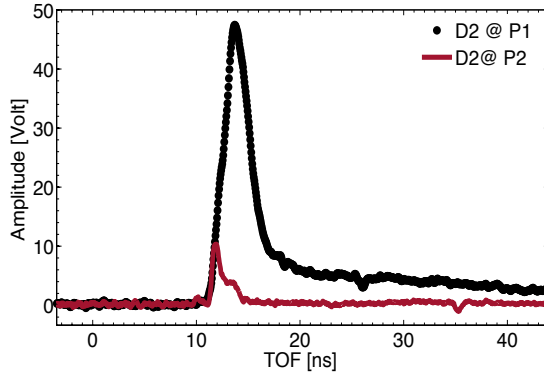


Figure 5.35: TOF signal acquired by D2 in position P1 after PMQs (black circle) and in position P2 after the dipole (reddish line). Both TOF signals are normalized at 44 cm flight path.

As it can be seen in figure 5.35 and 5.36a, after the dipole selection, the TOF signal measured in P2 exhibits a narrower peak than the one measured in P1, and lower signal amplitude indicating particle loss in the transmission through the magnet, as it is expected. The energy spectrum measured after the energy selection is shown in figure 5.36b.

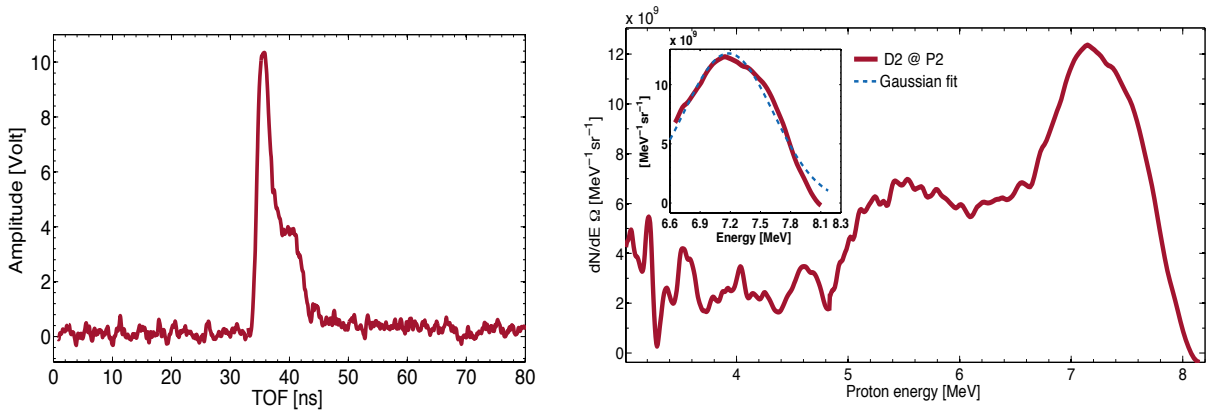


Figure 5.36: a) TOF signal acquired by D2 in position P2 . b) Proton energy spectrum reconstructed from TOF signal shown on the left. The inset shows the Gaussian fit performed on the higher energy peak.

A peak is well visible in the energy range between 6.5 MeV and 8 MeV, as expected considering the setup of the PMQs and dipole. A Gaussian fit has been performed in this

energy range, shown in the inset of figure 5.36, and is peaked at 7.18 MeV with a FWHM of 1 MeV (14 % energy resolution).

A tiny tail is also present in the energy spectrum shown in figure 5.36b, in the energy range between 4.8 MeV and 6.5 MeV, which can be explained considering the finite size of the detector's surface, which might detect also closer energy bandwidths deflected from the dipole and to the possible effect of spatial mixing due to the use of a single permanent dipole which might cause a residual mixing of different energy components at the same height, i.e. detector position.

Detector D3 was placed in position P3 in air, at about 1 cm from the exit kapton window. In such case, the 50 μm thick kapton window as well as the air traversed by the beam after the PMQs and the dipole selection, determine a not-negligible energy loss along the path in air, resulting in a shift towards lower energy and in a widening of the energy spectrum. Also the TOF signal is affected by the presence of air, resulting in a broader time distribution as shown in figure 5.37a. Moreover, in general, the flight path of particles traversing a material cannot be considered as the simple straight distance from the target, which is assumed in vacuum, due to the scattering with the atoms of the material traversed. Nevertheless, considering that the particle path in air is only 1 cm, which can be assumed negligible with respect to the total distance from the target (1.58 m), a straight flight path can be qualitatively assumed also for the in-air final path. The proton energy spectrum obtained from D3 TOF signal and shown in figure 5.37b ranges, indeed, from 3 MeV up to about 6.6 MeV as a consequence of the energy loss in the traversed kapton window and in 1 cm thick air.

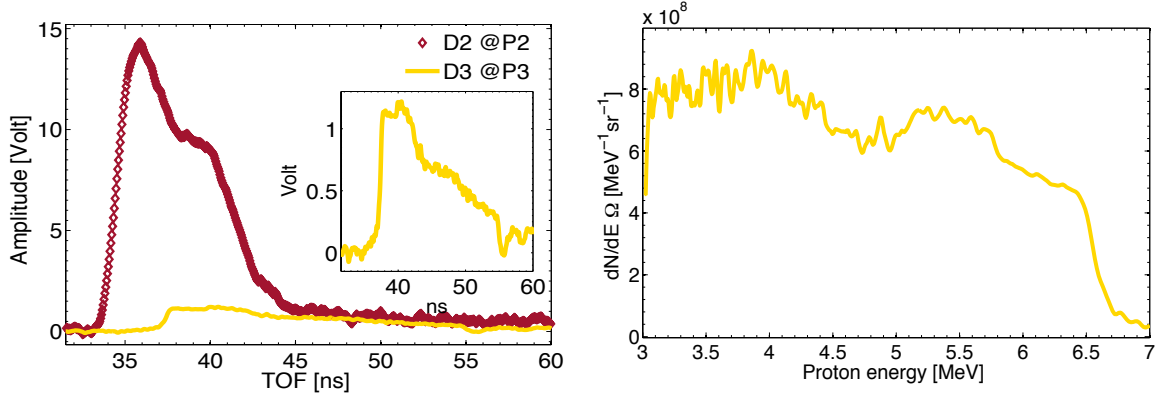


Figure 5.37: a) TOF signal acquired with the D3 in position P3 position the TOF signal acquired with the D2 detector in position P2. The inset shows the details of the D3 TOF signal. b) Proton energy spectrum extracted from the D3 TOF signal.

As shown in figure 5.37, also the amplitude of the signal acquired by D3 in position P3 is clearly lower than the one acquired by D2 in the position P2, resulting, as it is expected, in a lower number of protons. Table 5.13 lists the number of protons/sr in the energy range [4.8-7 MeV] extracted from the energy spectra measured with D2 and D3, shown in figure 5.35 and figure 5.37.

D2 @ P2	D3 @ P3
$1.4 \pm 0.1 \cdot 10^{10}$	$1 \pm 0.1 \cdot 10^9$

Table 5.13: Number of protons/sr detected with D2 in the position P2 and with D3 in the position P2 in the energy range 4.8-7 MeV.

As it has been shown, the experiment carried out with the high-repetition rate table-top ATLAS laser system at LMU, allowed to highlight the capability of TOF-based diagnostics to provide on-line time, energy and fluence information of the accelerated beam. In particular, such detectors coupled with the TOF technique offer the possibility to tune on-line the transport element setting, in this case PMQs and energy selector dipole, in order to obtain the best transport configuration. This fact, together with the detector fast response, which allows to use such kind of detectors also with an high repetition rate, is

extremely important in view of their use along the ELIMAIA beam line, representing one of their main advantages.

5.3 TOF diagnostics for laser-induced aneutronic fusion reaction studies

The TOF-based diagnostics may also represent a powerful tool to study nuclear reactions occurring in the plasma generated by the laser-matter interaction and resulting in the production of given ion species. In particular, the TOF-based diagnostics developed as one of the main goal of the present thesis, has been recently used as main diagnostics in the LASERLAB experimental campaign dedicated to the *Laser Induced Aneutronic Fusion Reaction by Advanced Materials*(PALS002126) carried out at PALS laser facility (Prague) in November 2016 and in May 2017.

The experiment concerns the investigation of the aneutronic fusion occurring in the nuclear reaction of Boron ions with protons and generating α particles [38, 39, 40]. In particular, the α particles can be produced via three main channels [146]:

1. ${}^{11}_5B + p \rightarrow \alpha_0 + {}^8_4Be + 8.59MeV \rightarrow \alpha_0 + \alpha_{01} + \alpha_{02}$
2. ${}^{11}_5B + p \rightarrow \alpha_1 + {}^8_4Be^* + 5.65MeV \rightarrow \alpha_0 + \alpha_{11} + \alpha_{12}$
3. ${}^{11}_5B + p \rightarrow 3\alpha + 8.68MeV$

When a proton collides with a ${}^{11}B$ nucleus the excited ${}^{12}C^*$ compound nucleus is formed. Being extremely unstable, the ${}^{12}C^*$ decays immediately into an unbound 8Be in its fundamental (channel 1) or excited state (channel 2), emitting exactly one α particle, α_0 , in channel 1, and α_1 , in channel 2, with a well-defined energy.

In both cases, the 8Be nucleus in turn decays into two secondary α particles, α_{01} , α_{02} in channel 1 and α_{11} , α_{12} in channel 2.

The third channel corresponds to the direct 3-body reaction, without 8Be intermediary

formation, with released energy of 8.68 MeV in form of kinetic energy given to the α particles. The channels 1 and 2 are considerably dominant with respect to the channel 3, characterized by low cross section (about $10 \mu\text{barn}$).

On the other hand, in order to activate the reaction, protons with a sufficient high energy are required. In particular, according to the theoretical calculation reported in [147], the highest cross-section value of about 1.2 barn is obtained for proton incident kinetic energies between 600 and 700 keV with a resonance at 675 keV [147, 148], see figure 5.38. Alpha particles in a broad energy range between 2.5 and 5.5 MeV are produced with a resonance peaked around 4.3 MeV [149, 150]. Moreover, channel 2 can also generate α particles in higher energy range between 6 to about 10 MeV [151, 152, 153].

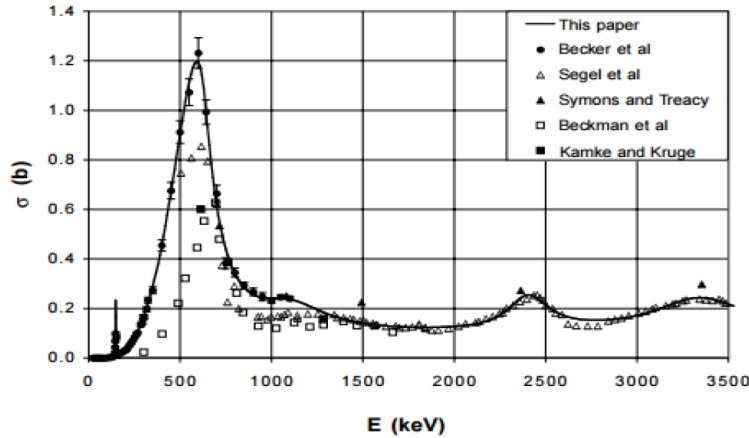


Figure 5.38: Cross section of the proton-boron reaction as a function of incident proton energy [147].

The study of such reaction, producing Multi-MeV α particles, without neutron emission, is particularly attractive for applications, as the medical one, providing a possible alternative therapy for cancer therapy, called Proton-Boron Fusion Therapy (PBFT) [154]. It consists on the injection of ^{11}B on the tumor region, in the irradiation with proton beams and in the consequent α particle production from fusion reaction. The α particles produced in the reaction, are known as high-LET particles and, having a range in water shorter than the cell or tumor dimension ($\sim 30 \mu\text{m}$), could significantly enhance the total dose deposited

in the tumor and the RBE (Relative biological effectiveness [155]).

In this context, a huge effort of the researchers has been recently addressed on the possibility to use laser-accelerated protons to induce proton-boron reaction, in contrast to the conventional acceleration technique, as it is reported in [151], [156]. The extremely high flux (p/s) of laser-accelerated proton beams, in contrast to conventionally accelerated proton beams, might represent, in fact, a great advantage, allowing to increase the number of interaction with Boron nucleus in the target, and hence the α production.

In particular, an experiment carried out by Picciotto et al. [41] has been performed at the PALS laser facility, indicating a clear enhancement in the α particle yield, measuring a number of $10^9\alpha/sr$ and resulting from the combination of the specific target structure and the laser pulse (10^{16} Wcm^{-2}) shape.

A recent experimental campaign, which will be described in details in the current section, has been carried out at PALS laser facility in November 2016 and May 2017, with the main purpose to confirm the results reported in [41] and demonstrate the enhancement of α particle yield from nuclear reaction, by using thin structured boron-doped hydrogen-enriched silicon target fabricated at the Micro-Nano Facility of Fondazione Bruno Kesler in Trento, Italy [157].

Moreover, the angular distribution of α particles produced from the fusion reaction has been measured for the first time by using an array of TOF-based detectors, namely diamond and silicon carbide ones, surrounding the target, at different angles with respect to target normal direction.

In such case, simultaneous on-line TOF measurements at different angles, will provide important information on the fusion reaction occurring in the laser-target interaction, particularly on the α particle emission direction, demonstrating TOF technique advantages also in such kind of investigation.

5.3.1 Experimental setup

The Prague Asterix Laser System (PALS) is an high-power Iodine laser able to deliver laser pulses with an energy of 600 J (nominal value 1 kJ) in about 300 ps pulse duration, corresponding to a power of 2 TW. It operates at the fundamental wavelength 1315 nm and a power density on the target up to $3 \cdot 10^{16} \text{ W/cm}^2$. The experimental setup, shown in figure 5.39, consisted of Thomson Parabola, positioned in forward direction, diamond, silicon carbide and nuclear track CR39 detectors placed at different angles with respect to the target normal direction; the setup allowed to measure the angular distribution of both proton and alpha particles.

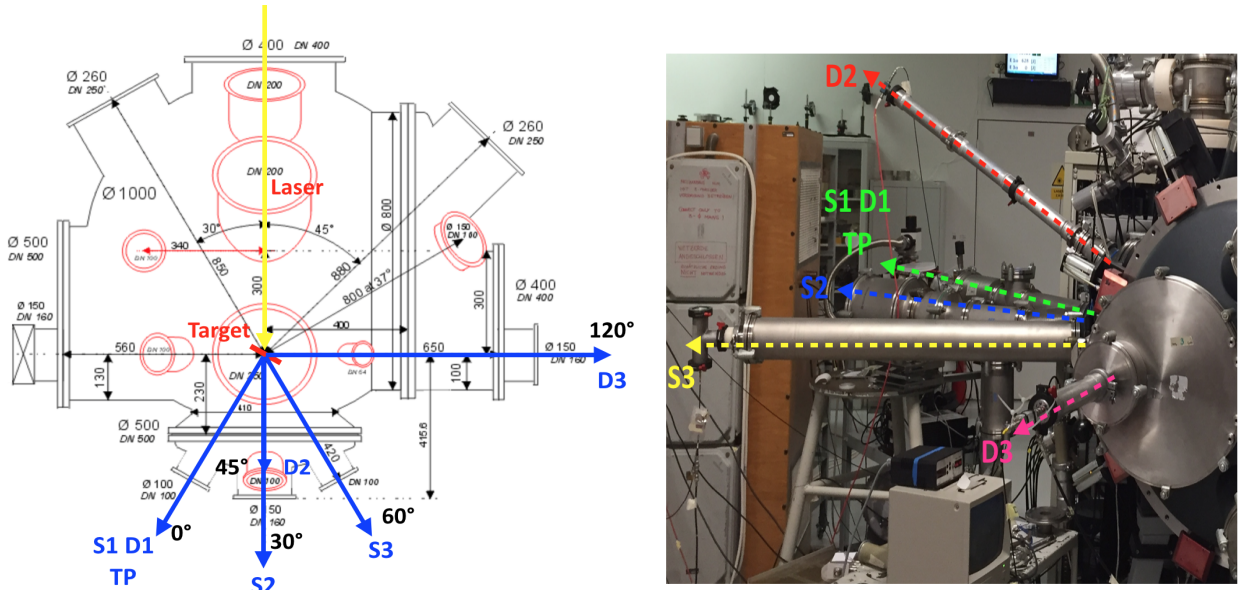


Figure 5.39: Layout and picture of the experimental set-up at PALS laser facility. The angular positions of TOF detectors with respect to target normal direction are also reported.

D1, D2, D3 respectively stand for $20\mu\text{m}$ thick single crystal diamond detectors fabricated at University of Rome Tor Vergata and S1, S2, S3 for silicon carbide detectors provided by CNR-ST collaboration. TOF signals have been stored with fast digital scopes, terminated with a 50 Ohm load impedance. A voltage of -300 V was applied to S1, S2 and S3

5.3. TOF DIAGNOSTICS FOR LASER-INDUCED FUSION REACTION STUDIES

corresponding to a depletion layer of $27 \mu\text{m}$, i.e. the detector active thickness. Detector positions, angle and distances with respect to the target position are listed in table 5.14.

Detectors	θ [°]	Distance [m]
D1	0 °	1.58 m
D2	45 °	1.39 m
D3	120°	1.08 m
S1	0 °	1.58 m
S2	30 °	1.36 m
S3	60 °	1.40 m

Table 5.14: Distances from target and angular position (θ) for each of the used detector.

CR39 nuclear track detectors were also used as additional diagnostics for α particle and proton absolute fluence measurement and were placed on the chamber walls at different detection angles with respect to the target. Both TOF detector and CR39s were used with different Al absorber foils, in order to discriminate particles from protons. In particular, $6.5 \mu\text{m}$ Al and $10 \mu\text{m}$ thick Al foil were chosen as absorber to cut protons with an energy respectively up to 570 keV and up to 770 keV and α particles with an energy up to 1.88 MeV and up to 2.74 MeV.

As shown in figure 5.39 the target was tilted of -30° with respect to laser direction to increase the interaction surface and enhance the cross section. Two different target structures were used during the experiment:

1. SiHB: A SiHB target consisting of a $10 \mu\text{m}$ thick Silicon layer doped by boron atoms installed in a depth of 200 nm in Silicon (Si), forming a layer with a thickness of 100 nm and boron concentration of $1 \cdot 10^{22} \text{cm}^{-3}$. The hydrogen atom concentration was increased by thermal annealing during which hydrogen atoms diffuse into Si matrix and form Si-H bonds reaching the concentration of $5 \cdot 10^{22} \text{cm}^{-3}$.
2. SiHB+PR: A SiHB target coated with a photoresist (PR) layer (CH compound) with a thickness of $5 \mu\text{m}$ and density of 1 g/cm^3 .

Structures and pictures of doped silicon targets are shown in figure 5.40.

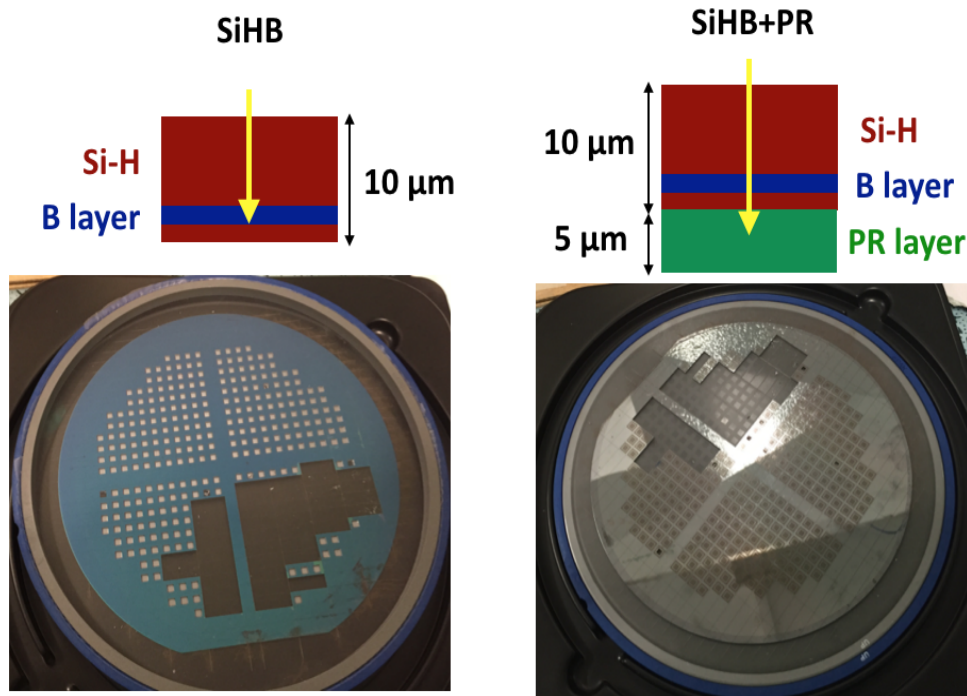


Figure 5.40: Simplified model and pictures of the two target structures SiHB and SiHB+PR.

A comparison between the results acquired with different diagnostics allowed to identify α particles, disentangling the latter from the accelerated proton contribution, and to measure the number of α particles produced for both targets.

5.3.2 Methods

Figure 5.41 shows the TOF signal acquired by detector D3 placed at 120° with respect to target normal direction, with 10 μm thick Al foil, using the SiHB+PR target. The corresponding energy calculated for protons and α particles are reported in figure 5.41b .

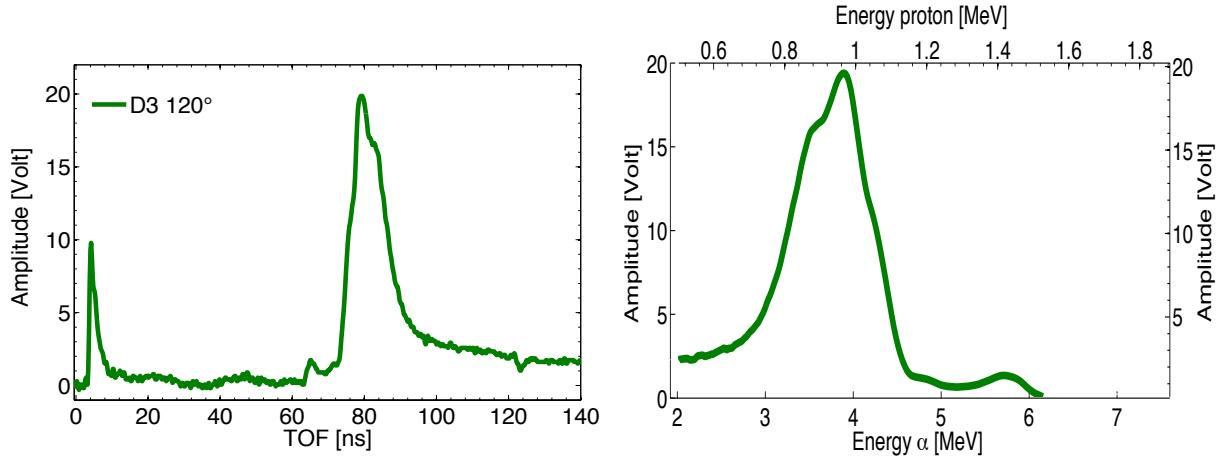


Figure 5.41: TOF signal acquired with D3 placed at 120° with $10 \mu\text{m}$ Al foil (a) and corresponding proton and α energy (b).

In figure 5.41b the bottom axis reports the α kinetic energy while the corresponding proton energy is reported on top. As one can see in figure 5.41, the TOF range of α particles in the energy range of interest (3-10 MeV) overlaps with the TOF range corresponding to the accelerated protons (500 keV-3 MeV). Therefore, due to the similar TOF and stopping power of α particles and protons in the energy range of interest, it is not possible to disentangle α contribution from protons only from TOF signal, even using absorbers.

In such case, in order to be completely sure to detect only α particles in TOF detector placed at a given angle, the proton energy cut-off dependence from the angle has been studied, using a $6.5 \mu\text{m}$ Al flat foil as reference target, accelerating only protons and ions. The proton energy cut-off was measured at 0° , 30° and 60° respectively with S1, S2, S3. Figure 5.42 reports the maximum proton energy as a function of the angle θ with respect to the target normal direction. As expected, the cut-off decreases with the angle following, in this case, a quadratic law obtained by fitting the measured data. The uncertainties reported in figure 5.42 were obtained with the error propagation on the energy calculation.

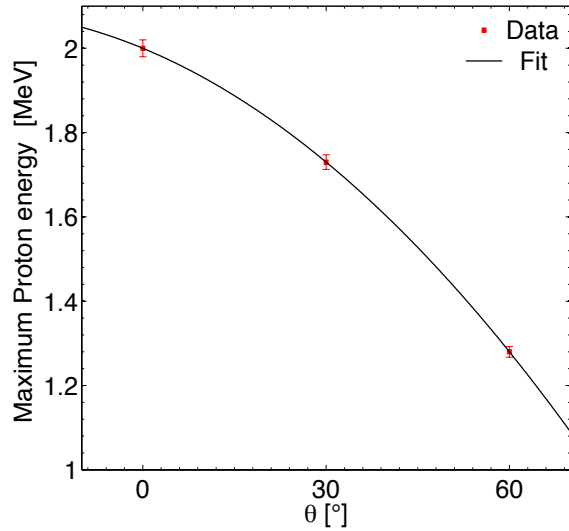


Figure 5.42: Proton energy cut-offs measured with S1, S2, S3 respectively at 0° , 30° and 60° with an Al reference target.

Considering the dependence of the maximum proton energy with the angle, a high-energy threshold was defined in order to analyze the TOF region where only alpha particles may contribute to the signal. For this reason, the TOF signals were converted in energy spectrum for α particles with energy higher than 5 MeV, which correspond to 1.2 MeV energy for protons. As an example, for TOF signal shown in figure 5.41 a, the α energy spectrum reconstruction has been performed in the TOF interval $62 \text{ ns} < \text{TOF} < 70 \text{ ns}$.

Under this assumption, the calculation of α particle production yield was performed at large angles (30° , 45° , 60° , 120°), not including 0° . This method leads to an underestimation of the measured α particle yield, since the α particles in the energy range between 2 and 5 MeV, which is the main expected contribute from the occurring nuclear reaction, are not considered, but assures to not include in the α particle analysis the proton contribution.

5.3.3 Results

Based on the assumptions discussed in section 5.3.2 the analysis of TOF signals acquired with silicon carbide as well as diamond detectors was performed for both target structure to highlight the possible difference in α particles efficiency production and angular emission. Figure 5.43 (a) shows the TOF signals acquired with D2 (45°), S2 (30°) and S3 (60°) using the SiHB target, while figure 5.43 (b) shows the TOF signals detected with D2 (45°) and S2 (30°) irradiating SiHB+ PR target from the silicon side. For simplicity, both TOF signals shown in figure 5.43 are normalized at 1 m flight path.

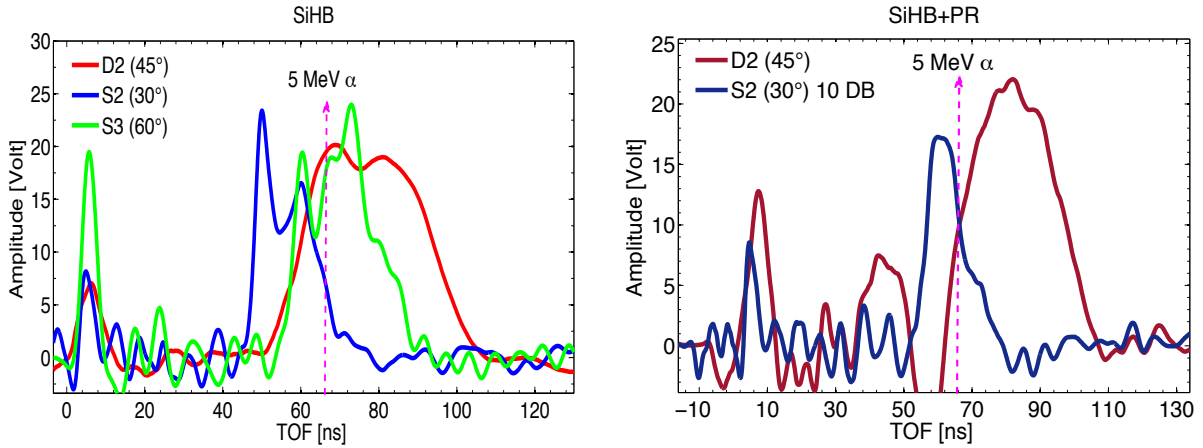
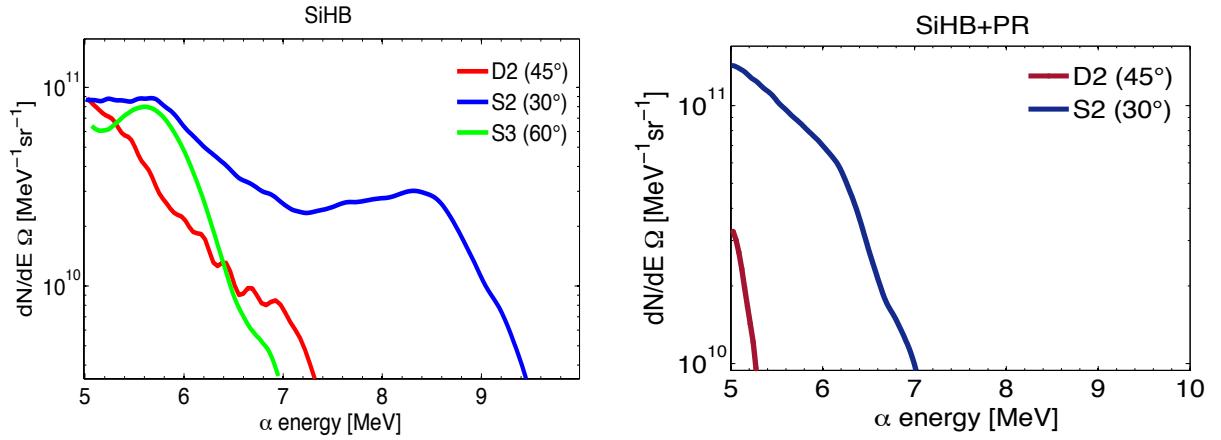


Figure 5.43: TOF signals acquired with D2, S2, S3 with SiHB target (a) and with D2 and S2 irradiating SiHB+PR target (b)

Since the TOF value corresponding to 5 MeV α particles at 1 m as flight path, is about 65 ns, as indicated in figure 5.43, the α energy spectrum was reconstructed for the considered detector in the time interval < 65 ns. The results are shown in figure 5.44 for both target configurations. Integrating the energy spectra obtained for energies > 5 MeV, the numbers of produced α particles per sr, have been estimated for all the detection angles (table 5.15).


 Figure 5.44: α energy spectra reconstructed for signals shown in figure 5.43.

Detectors	SiHB	SiHB+PR
D2	$6.2 \pm 0.3 \cdot 10^{11}$	$5.5 \pm 0.3 \cdot 10^{10}$
S2	$1.76 \pm 0.1 \cdot 10^{11}$	$1.4 \pm 0.1 \cdot 10^{11}$
S3	$7.8 \pm 0.3 \cdot 10^{10}$	

 Table 5.15: N_α /sr extracted for each detector and target configuration for $E_\alpha > 5$ MeV.

A yield of 10^{11} α /sr has been extracted for both target structures with TOF detectors showing a relevant enhancement of alpha particle yield of about two orders of magnitude with respect to the previous investigations [41]. Nevertheless, the number of α /sr extracted from TOF signal analysis represent an underestimation of the effective number of α particles produced in the reaction, since the TOF analysis has been performed considering only α particles with an energy higher than 5 MeV.

The angular distribution of α particles was measured with the TOF detectors placed at angle between 30° and 120° (in backward direction). The number of α /sr as a function of the angle in the energy range >5 MeV for six different shots for both targets are shown in figure 5.45 and 5.46.

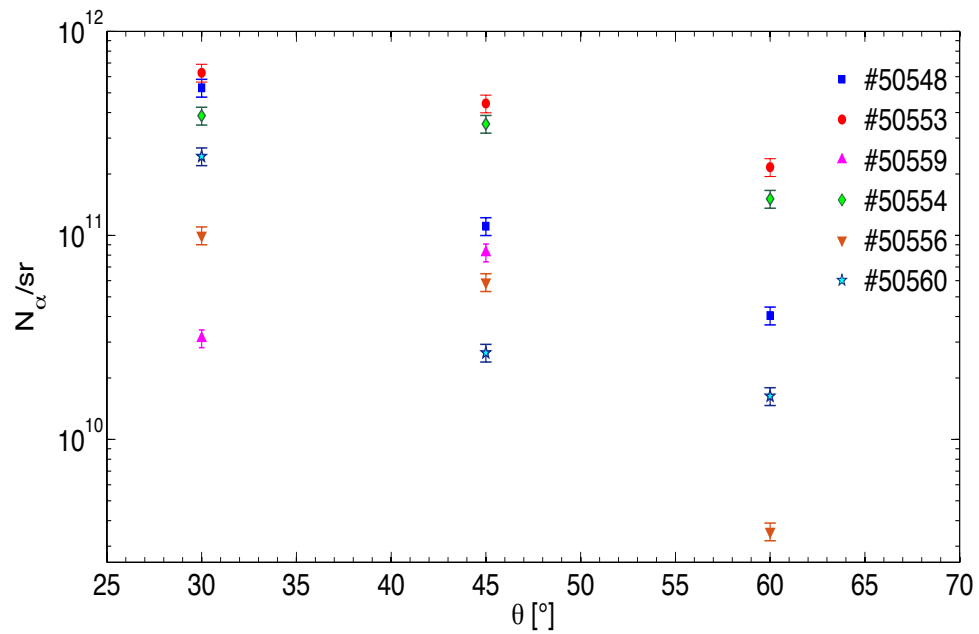


Figure 5.45: N_α /sr measured from TOF detectors as a function of the emission angle θ irradiating SiHB target. Colors state for different shots.

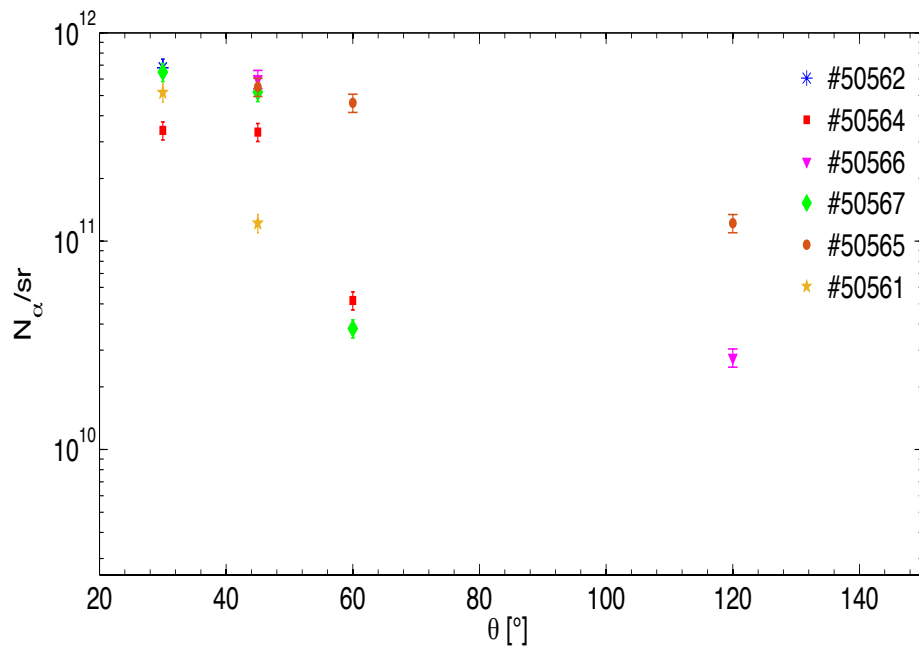


Figure 5.46: N_α /sr measured from TOF detectors as a function of the emission angle θ for SiHB+PR target. Colors state for different shots.

5.3. TOF DIAGNOSTICS FOR LASER-INDUCED FUSION REACTION STUDIES

A decreasing trend can be clearly observed for all the shots analyzed and for both targets, although more statistics is required to confirm these results.

Despite the low statistics, the α angular distribution obtained with the SiHB target (figure 5.45) seems to show an exponential decrease with the emission angle. On the other hand, the α angular distribution measured with SiHB+PR target seems to show a smoother slope indicating a more uniform emission than the SiHB target. An increment in the α yield is also detected at 45° and 60° with respect to the target without PR (figure 5.46). This could be qualitatively explained looking at the different laser-target interaction characteristics. The PR layer might actually act as a *sheath* compressing the plasma expansion and holding the accelerated particle expansion. As a consequence, this could results in a more isotropic angular emission of α particles compared to the target without the PR layer.

CR39 nuclear track detectors analysis confirms also the results achieved with TOF detectors. As an example, in table the number of α particles per sr measured with CR39 in the α energy range >5 MeV, during two shots and for SiHB and SiHB+PR target is reported.

Shot	Target	θ	Energy range [MeV]	α /sr
50556	SiHB	90°	5-5.5	$1.37 \cdot 10^{11}$
50562	SiHB+PR	60°	5-6.5	$2.10 \cdot 10^{11}$

Table 5.16: N_α /sr extracted from CR-39 track analysis.

As one can see from table 5.16, the numbers of α particles detected by CR-39 detectors are in good agreement, within the same order of magnitude, with the ones obtained in TOF measurement for the same energy region, reported in table 5.15. In order to directly compare the results obtained with TOF detectors and with CR-39s, the average number of α particles measured with TOF detectors for each detection angle and for all the shots shown in figure 5.45 and 5.46 have been calculated. Figures 5.47 and 5.48 show the average numbers obtained with TOF analysis respectively for SiHB and SiHB+PR target together with the CR-39 results. The uncertainties on the TOF data are obtained by calculating

5.3. TOF DIAGNOSTICS FOR LASER-INDUCED FUSION REACTION STUDIES

the standard deviation. As one can see in Figures 5.47 and 5.48, a rather good agreement can be observed between the number of particles detected by the CR-39 and the ones extracted from the TOF detectors.

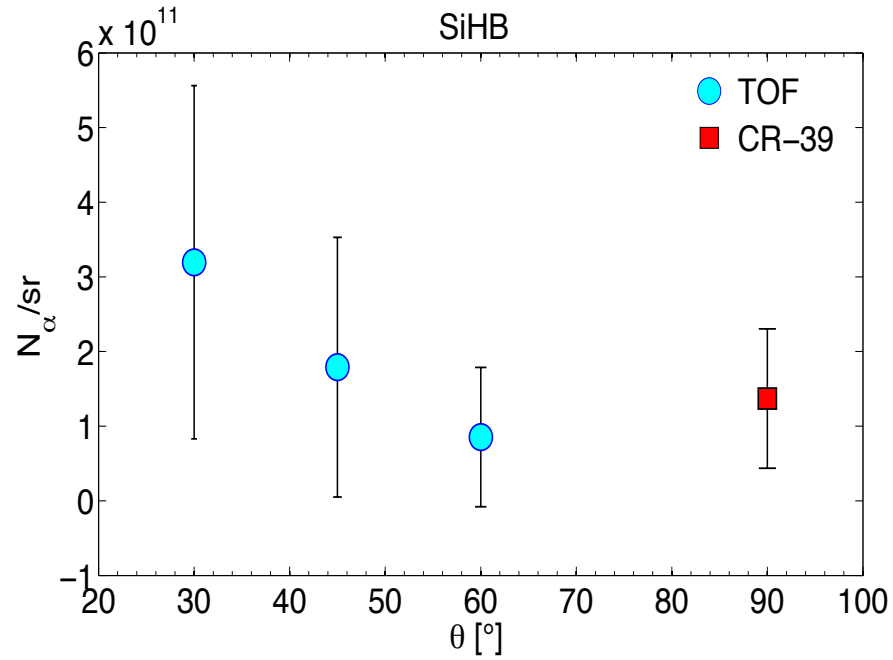


Figure 5.47: Average number of particles per sr evaluated by TOF detector (light blue closed circles) together with CR-39 results (red closed squares) for the SiH-B target.

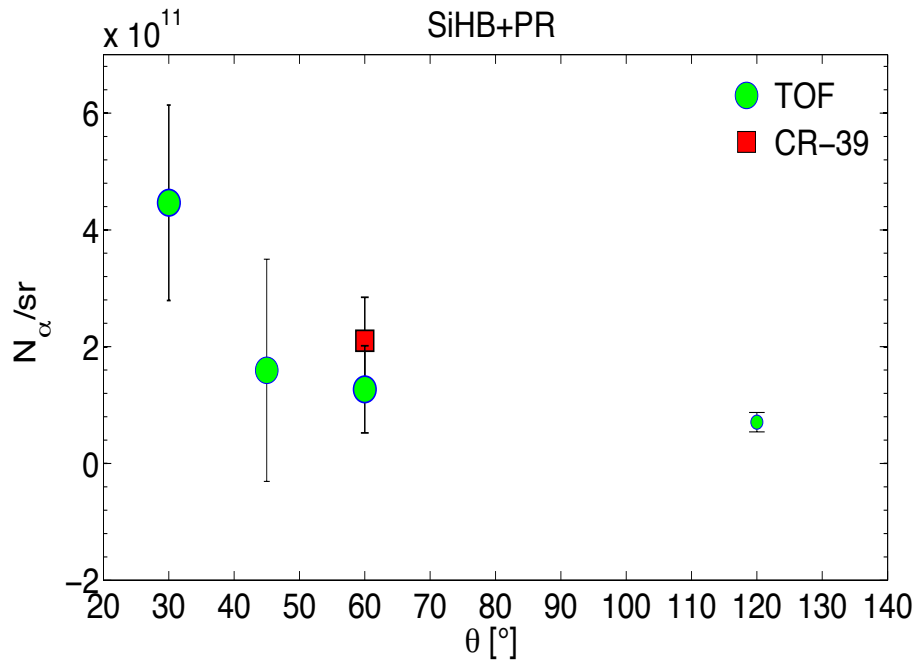


Figure 5.48: Average number of particles per sr evaluated by TOF detector (green closed circles) together with CR-39 results (red closed squares) for the SiH-B+PR target.

As one can clearly see in figures 5.47 and 5.48, the poor statistics as well as the poor laser reproducibility (see the shot to shot fluctuations in figures 5.45 and 5.46), lead to a high uncertainty. In order to increase the statistics and obtain more results with stable conditions, the second part of the experiment, carried out in May 2017 and whose analysis is still ongoing, allowed to complete the data set here presented. Moreover, the last part of the experiment has been performed using a bigger array of TOF detectors, consisting of 12 detectors, SiC and Diamond, and CR-39s covering the entire solid angle around the target, including backward direction, allowing to measure the α particle angular distribution with higher granularity.

Conclusions and future perspectives

The work presented in this thesis has been carried out in the framework of the ELIMED beam line development and realization at INFN-LNS. The beam line is devoted to the transport and the dosimetry of high-energy optically accelerated ion beams and will be installed by the end of 2017 at ELI Beamlines facility in Prague.

In particular, the thesis has been mainly focused on two aspects of the ELIMED beam line development; a complete Geant4 simulation of the ELIMED beam line, the realization of an on-line diagnostics system, based on the TOF technique and the development of an analysis procedure, optimized for high-energy laser-driven ion beams, required to extract the energy spectrum from the TOF signal.

Transport and the dosimetry elements composing the ELIMED beam line described in chapter 2, have been fully simulated with the Geant4 simulation toolkit, providing a user-oriented application that will be available for future users, to predict different experimental setups and will represent a powerful tool for experiment preparation. The possibility to use typical laser-driven ion source, such as Particle In Cell (PIC) outputs, as input for the simulation, has been also foreseen and implemented in the application in order to provide realistic prediction. Top to bottom simulations of the whole beam line have been also performed in order to evaluate expected energy spectra, fluence and dose distributions per shot downstream the PMQ system, the ESS and at the in air irradiation point. Energy spectra, transmission efficiency, longitudinal and transversal dose distributions in water at the irradiation point as a function of the slit aperture, for low (5 MeV) and high (60 MeV) energy selected along the ELIMED beam line have been studied. For both energy

configurations, small slit aperture results in small total energy spread, with a resolution ranging from 4% to 7% for 5 MeV protons and between 7% and 11% for 60 MeV protons. The transversal profile optimization for 60 MeV proton selection, has been studied in order to improve beam homogeneity and provide flat transversal profiles needed for applications, like the medical ones. The use of passive energy degrading elements as scattering foils, including the straggling effect of air, has been investigated with the simulation in order to identify the optimum configuration in terms of beam homogeneity ensuring a sufficient dose delivered per shot. The best compromise between profile flatness and particle transmission has been obtained with 100 μm Ta scattering foil and acquiring the profiles after 2 m of air from the kapton window. In this configuration, a profile flatness (10 %) for a 10 mm diameter beam spot size with a delivered dose per shot in water of about 7 cGy on the peak, have been evaluated. Considering 1 Hz of laser repetition rate, it will lead to a reasonable dose-rate of about 4 Gy/min.

On the other hand, as it is known, medical applications, such as hadrontherapy, require also a longitudinal flat beam profile (Spread Out Bragg Peak) in order to deliver a constant dose on the total tumour thickness. The possibility to use laser-driven proton beams transported with the ELIMED beam line, to provide SOBP profiles of clinical interest has been preliminary investigated by using the Geant4 simulation. In particular, the studied approach is based on the active energy modulation of the beam changing the magnetic field of the ESS. The weights of each mono-energetic Bragg peak corresponding to the energy selected with the ESS, and required to obtain a flat depth-profile, have been calculated with a proper algorithm, following the approach reported in [101]. In particular, an homogeneity within 3% has been achieved in a 20 mm thick modulation region of the obtained SOBP profile. Nevertheless, some improvements are needed to obtain a sharper distal fall-off in the SOBP, still far from clinical requirement, through the optimization of the energy spread of the highest energy peak, i.e 60 MeV.

A realistic delivered dose, reproducing a typical single session of an ocular proton therapy treatment, i.e. 15 Gy, has been considered in order to estimate the corresponding

irradiation time, considering both 1 Hz and 10 Hz laser repetition rate. In particular, an homogeneity within 3 % has been achieved in a 20 mm thick modulation region of the obtained SOBP profile at 15 Gy, achieved in about 16 minutes and 110 s, considering respectively 1 Hz and 10 Hz laser-repetition rate. The latter is particularly compatible with typical clinical irradiation times, and provide promising results in view of future clinical applications at ELI Beamlines.

The study carried out in the thesis is a preliminary feasibility study to investigate possible future transport configurations of clinical relevance, using the ESS as an active energy modulator, and will be deeply investigated in the next future.

The second part of the thesis has been dedicated to the development of an on-line diagnostics system to monitor shot-to-shot the laser-driven ion beam parameters and to measure the energy spectrum and flux along the ELIMED beam line. Diamond and silicon carbide detectors, providing interesting advantages, as the high time and energy resolution and radiation hardness, as well as the good signal-to-noise ratio, have been chosen and will be used with the TOF technique. The TOF method has been widely used as a stable on-line diagnostics with low-energy (few MeV) laser-driven proton beams, as reported in many works in literature. Nevertheless, the high-energy of particles expected at ELIMAIA, up to 60 MeV/n, required the development of a proper analysis procedure in order to convert TOF signals arising from laser-driven ion beams, in energy spectrum for a given ion species. The details of the developed method, needed to obtain the energy spectrum and as a consequence the particle flux, are reported in chapter 4. Detectors, methodology and analysis procedure have been tested during three experimental campaigns with different laser systems, i.e. different laser power, energy and repetition rate, in order to explore advantages and limits of the TOF technique for on-line high-energy proton and fluence measurement:

- A test carried out with high-energy, up to 30 MeV, laser-driven proton beams at RAL laser facility (UK). The analysis procedure has been validated by comparing the TOF

results with the ones obtained with the well-established diagnostics, as Thomson parabola, RCFs and CR-39. The energy spectra as well as the number of protons extracted with the different used diagnostics are in good agreement, confirming the reliability of TOF technique with high-energy laser-driven ion beams.

- A test performed with a compact transport beam line and with the high-repetition rate ATLAS laser system at LMU (Munich). The capability of TOF detectors to provide real-time information, such as the time, energy distribution and the energy cut-off, downstream focusing and selecting magnetic elements has been verified. Moreover, the test confirmed that such kind of diagnostics is particularly suitable for on-line optimization of transport parameters with laser-driven ion beams, giving real-time crucial information.
- Test performed with the TW PALS laser system. The nuclear fusion reaction occurring between protons and boron nucleus and producing alpha particles with an energy ranging from 2 MeV up to 10 MeV, has been studied, using an array of diamond and silicon carbide detectors surrounding the target. In such case, the simultaneous TOF signals acquired by detectors at different angles, allowed to confirm the enhancement of alpha particle yield, previously observed in literature, and, for the first time, to measure the alpha particle angular distribution.

All these experiments have shown that the TOF technique is a powerful tool for high energy-laser driven ion beams diagnostics. In particular, the high time resolution of diamond detector is a peculiar advantage in view of the high-energy laser-driven ion beams expected to be accelerated at ELIMAIA. The narrow photopeak (few ns) typically measured by diamond detectors, poorly sensitive to X-rays, allows to detect the high-energy proton beam component also at very short flight path. As an example, the TOF value corresponding to 100 MeV protons at a flight path of 2 m, i.e. the first diagnostics section along the ELIMED beam line, is about 14 ns, which according to the results obtained at RAL, is sufficient to discriminate the proton energy cut-off. On the other hand, the

developed analysis procedure has still some limitations, which will be improved in the next future. For instance, the sharp threshold used on the TOF signal in the region where also ions contribute to the total signal, leads to an underestimation of the total number of protons. This can be improved, considering the relative abundances of the accelerated ion species measured by the TP using them to properly deconvolve the TOF signal. In this way, the proton contribution can be disentangled also in the overlap region, and considered in the reconstructed energy spectrum and fluence. More in general, the results achieved in this thesis, show that TOF-based detectors represent a powerful tool for beam diagnostics, offering the possibility to get on-line information of the beam. In particular, when only protons are accelerated, as in the case of the experimental campaign ELISE carried out at PALS with a cryogenic hydrogen target, the TOF technique is a powerful on-line tool, allowing to easily and directly reconstruct the proton energy spectrum from the total TOF signal. Moreover, the use of such kind of target, providing a high flux, up to 10^{14} p/sr, is particularly interesting also for applications, such as medical one, providing an intense proton source, without ion contamination. Moreover, recently the ELISE target system has been tested to accelerate high-energy protons with the PW Vulcan laser at the RAL laser facility. TOF detectors have been used to measure on-line the proton energy cut-off and spectrum in order to measure possible enhancement in the maximum proton energy and flux. According to the results obtained with the TW PALS laser system, this experiment may lead to study new scenarios in the acceleration mechanisms with low-density and pure hydrogen target, demonstrating the possibility to obtain high-intensity and high-energy laser-driven proton beams, which could be very interesting also in view of medical applications at ELI Beamlines.

Bibliography

- [1] G. Mourou, T. Tajima, S.V. Bulanov, *Reviews of Modern Physics* 78 (2006) 309.
- [2] A. Macchi, M. Borghesi, M. Passoni, *Reviews of modern physics*, Volume 85, April-June 2013
- [3] H. Daido, M. Nishiuchi, A.S.Pirozhkov, *Reports on Progress in Physics* (2012) 75
- [4] D. Bauer, *Theory of intense laser-matter interaction*
- [5] Clark, E. L., et al., 2000a, *Phys. Rev. Lett.* 84, 670.
- [6] A. Maksimchuk, K. S. Gu, D. Flippo, Umstadter and V.Y. Bychenkov, 2000, *Phys. Rev. Lett.* 84, 4108.
- [7] R. A. Snavely et al., 2000, *Phys. Rev. Lett.* 85, 2945.
- [8] S. A. Gaillard et al., *Physics of Plasmas* 18, 056710 (2011); doi: 10.1063/1.3575624
- [9] M. Passoni, V. T. Tikhonchuk, M. Lontano, and V.Y. Bychenkov, 2004, *Phys. Rev. E* 69, 026411.
- [10] M. Borghesi, J. Fuchs, S.V. Bulanov, A. J. MacKinnon, P. K. Patel and M. Roth, 2006, *Fusion Sci. Technol.* 49, 412
- [11] T. Esirkepov, M. Borghesi, S.V. Bulanov, G. Mourou, and T. Tajima, 2004, *Phys. Rev. Lett.* 92, 175003.
- [12] D. Doria et al., *AIP Advances* 2 (1) (2012) 011209

- [13] S. C. Wilks, A. B. Langdon, T. E. Cowan, M. Roth, M. Singh, S. Hatchett, M. H. Key, D. Pennington, A. MacKinnon, and R. A. Snavely, 2001, *Phys. Plasmas* 8, 542.
- [14] S.V. Bulanov, V.S. Khoroshkov, *Plasma Physics Reports* 28(5)(2002) 453.
- [15] S.V. Bulanov, J.J. Wilkens, T. Zh. Esirkepov, G. Korn, G. Kraft, S.D. Kraft, M. Molls, V.S. Khoroshkov, *Physics-Uspekhi* 57(12)(2014) 1149.
- [16] <http://www.qub.ac.uk/sites/LIBRA/Resources/>
- [17] <http://www.oncoray.de/?id=22>.
- [18] <http://www.munich-photonics.de/>.
- [19] W. Leemans, W. Chou, M. Uesaka, *ICF A Beam Dynamics Newsletters* 56(2011)51.
- [20] D. Margarone, G.A.P. Cirrone, G. Cuttone and G. Korn, Preface: 2nd ELIMED Workshop and Panel, *AIP Conf. Proc.* 1546 (2013) 1.
- [21] G.A.P. Cirrone et al., *Nucl. Instrum. Meth. A* 796 (2015) 99.
- [22] G.A.P. Cirrone et al., *Appl. Sci.* 5 (2015) 427.
- [23] S. Agostinelli et al., *Nuclear Instruments and Methods A* 506 (2003) 250-303.
- [24] J. Allison et al., *IEEE Transactions on Nuclear Science* 53 No. 1 (2006) 270-278.
- [25] J. Allison et al., Volume 835, 1 November 2016, Pages 186-225
<https://doi.org/10.1016/j.nima.2016.06.125>.
- [26] J. Pipek, F. Romano, G. Milluzzo et al., *Journal of Instrumentation*, Volume 12, March 2017
- [27] F. Romano et al., *IOP Conf. Series: Journal of Physics: Conf. Series* 777 (2017) 012016

- [28] D. Margarone et al, Rad Eff Def. Solids 163, 2008, 463
<http://dx.doi.org/10.1080/10420150701780540>
- [29] D. Margarone et al. J. Appl. Phys. 109, 103302 (2011); doi:10.1063/1.3585871
- [30] M. Marinelli, E. Milani, G. Prestopino, C. Verona et al. Applied Surface Science 272 (2013) 104- 108.
- [31] V. Scuderi et al., Jinst March 2017 doi:10.1088/1748-0221/12/03/C03086
- [32] G. Milluzzo et al., Jinst February 2017 doi:10.1088/1748-0221/12/02/C02025
- [33] G. Milluzzo et al., Jinst March 2017 doi:10.1088/1748-0221/12/03/C03044.
- [34] <http://simion.com>
- [35] www.comsol.it.
- [36] C.N. Danson et al., Nucl. Fusion 44 (2004) S239.
- [37] H. Baumhacker, A. Böswald, H. Haas, M. Fischer, W. Fölsner, G. Keller, U. Andiel, X. Dong, M. Dreher, K. Eidmann, E. Fill, M. Hegelich, M. Kaluza, S. Karsch, G. Pretzler, G. D. Tsakiris, and K. J. Witte, MPQ-Report 272 (2002)
- [38] H. Hora, 2010 Energy Environ. Sci. 3 479
- [39] N. Rostoker, M.W. Binderbauer, H.J. Monkhorst 1997 Science 278 1419
- [40] G.L. Kulcinski and J.F. Santarius 1998 Nature 396 725
- [41] A. Picciotto, D. Margarone et al., Phys. Rev. X 4 (2014) 031030, D. Margarone, A. Picciotto et al., Plasma Phys. Control. Fusion 57 (2015) 014030.
- [42] S. J. Gitomer, R. D. Jones, F. Begay, A.W. Ehler, J. F. Kephart, and R. Kristal, 1986, Phys. Fluids 29, 2679.

- [43] A. P. Fews, P. A. Norreys, F. N. Beg, A. R. Bell, A. E. Dangor, C. N. Danson, P. Lee, and S. J. Rose, 1994, *Phys. Rev. Lett.* **73**, 1801.
- [44] F. N. Beg, A. R. Bell, A. E. Dangor, C. N. Danson, A. P. Fews, M. E. Glinsky, B. A. Hammel, P. Lee, P. A. Norreys, and M. Tatarakis, 1997, *Phys. Plasmas* **4**, 447.
- [45] J. S. Loeffler, M. Durante, *Nat. Rev. Clin. Oncol.* advance online publication 21 May 2013; doi:10.1038/nrclinonc.2013.79
- [46] R. R. Wilson, 1946 *Radiology* **47**, 487–491.
- [47] Particle Therapy Co-Operative Group (PTCOG), <http://www.ptcog.ch/index.php/ptcog-patient-statistics>
- [48] Ken W. D. Ledingham et al., *Appl. Sci.* 2014, **4**, 402-443; doi:10.3390/app4030402
- [49] K. Krushelnick et al., 1999, *Phys. Rev. Lett.* **83**, 737.
- [50] G. S. Sarkisov, V.Y. Bychenkov, V. N. Novikov, V. T. Tikhonchuk, A. Maksimchuk, S.Y. Chen, R. Wagner, G. Mourou, and D. Umstadter, 1999, *Phys. Rev. E* **59**, 7042.
- [51] T. Ditmire, J.W. G. Tisch, E. Springate, M. B. Mason, N. Hay, R. A. Smith, J. Marangos, and M. H. R. Hutchinson, 1997, *Nature (London)* **386**, 54.
- [52] Paul M. Bellan, *Fundamentals of plasma physics*
- [53] Richard Fitzpatrick, *Plasma Physics*
- [54] Peter Mulser and Dieter Bauer. *High power laser-matter interaction*, volume 238. Springer Science Business Media, 2010.
- [55] *Short Pulse Laser Interaction with Matter*. 2005.
- [56] F. Cattani, A. Kim, D. Anderson, and M. Lisak, 2000, *Phys. Rev. E* **62**, 1234.
- [57] V.V. Goloviznin and T. J. Schep, 2000, *Phys. Plasmas* **7**, 1564.

- [58] B. Shen and Z. Xu, 2001, Phys. Rev. E 64, 056406.
- [59] S. C. Wilks, W. L. Kruer, M. Tabak, and A. B. Langdon, 1992, Phys. Rev. Lett. 69, 1383.
- [60] M. Passoni, V. T. Tikhonchuk, M. Lontano, and V.Y. Bychenkov, 2004, Phys. Rev. E 69, 026411.
- [61] A. J. Mackinnon, M. Borghesi, S. Hatchett, M. H. Key, P. K. Patel, H. Campbell, A. Schiavi, R. Snavely, S. C. Wilks, and O. Willi, 2001, Phys. Rev. Lett. 86, 1769.
- [62] M. Hegelich et al., 2002, Phys. Rev. Lett. 89, 085002.
- [63] J. Fuchs et al., 2006b, Nat. Phys. 2, 48.
- [64] K. Zeil, S. D. Kraft, S. Bock, M. Bussmann, T. E. Cowan, T. Kluge, J. Metzkes, T. Richter, R. Sauerbrey, and U. Schramm, 2010, New J. Phys. 12, 045015.
- [65] <http://static.sif.it/SIF/resources/public/files/va2011/borghesi0624.pdf>-cited 1.5.2017
- [66] M. Borghesi et al., 2008, Plasma Phys. Controlled Fusion 50, 124040.
- [67] K. Zeil et al., New Journal of Physics, 12:045015, 2010.
- [68] J. Fuchs et al., Nature Physics, 2:48, 2006.
- [69] M. Roth et al., Physical Review Special Topics-Accelerators and Beams, 5:061301, 2002.
- [70] A. J. Mackinnon, Y. Sentoku, P.K. Patel, DW. Price, S. Hatchett, M.H. Key, C. Andersen, R. Snavely and R.R. Freeman, 2002 Phys. Rev. Lett. 88 215006
- [71] S. Wilks et al, Phys. Rev. Lett, 69,1383 (1992)
- [72] Y. Sentoku, T. E. Cowan, A. Kemp, and H. Ruhl, 2003, Phys. Plasmas 10, 2009.

- [73] T. Schlegel, N. Naumova, V. T. Tikhonchuk, C. Labaune, I.V. Sokolov, and G. Mourou, 2009, Phys. Plasmas 16, 083103.
- [74] A. Macchi, F. Cattani, T.V. Liseykina, and F. Cornolti 2005, Phys. Rev. Lett. 94, 165003.
- [75] R. L Forward, 1984, J. Spacecr. Rockets 21, 187.
- [76] J. F. L Simmons and C. R. McInnes, 1993, Am. J. Phys. 61, 205.
- [77] Short Pulse Laser Interactions with Matter
- [78] ELI-Extreme Light Infrastructure Whitebook, Science and Technology with ultra-intense Lasers
- [79] <https://www.eli-beams.eu/>
- [80] F. Romano et al., Nucl. Instrum. Meth. A 829 (2016) 153.
- [81] F. Schillaci et al., MT24, October 2015, Seoul, Korea
- [82] F. Schillaci et al., 2015 JINST 10 T12001 doi:10.1088/1748-0221/10/12/T12001
- [83] K. Halbach, Nucl. Instrum. Methods 169 1 (1980)
- [84] Martin Reiser, WILEY-VCH Verlag GmbH Co. KGaA
- [85] P. Castro, Desy technical note 2003-01 (2003).
- [86] F. Schillaci et al., 2016 JINST 11 P08022 doi:10.1088/1748-0221/11/08/P08022
- [87] <http://operafea.com>
- [88] International Atomic Energy Agency, Absorbed Dose Determination in External Beam Radiotherapy: An International Code of Practice for Dosimetry Based on Standards of Absorbed Dose to Water, Pub. by IAEA, Vienna, 2000.

- [89] R. Leanza et al., 2017 JINST 12 C03046 doi:10.1088/1748-0221/12/03/C03046
- [90] R. Cambria, et al., Physics in Medicine and Biology 42 (1997) 1185.
- [91] J.W. Boag and T.Wilson “The saturation curve at high ionization intensity”
- [92] A. La Rosa et al., Nuclear instrument and Methods in Physics Research A 586 (2008)270-275
- [93] “Simulations and Measurements of Secondary Electron Emission Beam Loss for LHC”, D. Kramer, B. Dehning, E.B. Holzer, G. Ferioli, M Stockner
- [94] Daniel Kramer Thesis “Design and implementation of a Detector for High Flux Mixed Radiation Fields”
- [95] A.F. Bjelajew, “Fundamentals of the Monte Carlo method for neutral and charged particle transport” (2001)
- [96] www.geant4.cern.ch.
- [97] Quick migration guide for Geant4 version 10.0, <https://twiki.cern.ch/twiki/bin/view/Geant4/QuickMigrationGuideForGeant4V10>.
- [98] Xin Dong, Gene Cooperman, John Apostolakis, Euro-Par 2010 - Parallel Processing Lecture Notes in Computer Science Volume 6272, 2010, pp 287-303.
- [99] [Geant4 User’s Guide for Application Developers](#).
- [100] [Physics Reference Manual](#)
- [101] S. Bijan Jia et al., Nuclear Instruments and Methods in Physics Research A 806 (2016) 101–108
- [102] D. Margarone et al., PHYSICAL REVIEW SPECIAL TOPICS—ACCELERATORS AND BEAMS 18, 071304 (2015)

- [103] M. De Marco et al., J. Phys. Conf. Ser. 508 (2014) 012007.
- [104] P.R. Bolton et al., Instrumentation for diagnostics and control of laser-accelerated proton (ion) beams, Physica Medica 30 (2014) 255e270
- [105] F. Nurnberg, M. Schollmeier, E. Brambrink, A. Blazevic, D. Carroll, K. Flippo, et al., Rev Sci Instrum 2009;80:033301. 13pp.
- [106] D. S. Hey, M.H. Key, A.J. Mackinnon, A.G. MacPhee, P.K. Patel, R.R. Freeman, Rev Sci Instrum 2008;79:053501. 4pp.
- [107] E. Breschi, M. Borghesi, M. Galimberti, D. Giulietti, L.A. Gizzi, L. Romagnani, Nucl Instrum Methods Phys Res A 2004;522:190. 6pp.
- [108] D. Kirby, S. Green, F. Fiorini, D. Parker, L. Romagnani, D. Doria et al., Lasers Part Beams 2011;29:231. 9pp.
- [109] Nuclear Instruments and Methods in Physics Research B 86 (1994) 311-316 North-Holland
- [110] B. M. Hegelich et al. Nature, 439:441, 2006.
- [111] N. Sinenian et al., Review of Scientific Instruments, 82:7103303, 2011.
- [112] S. Gaillard et al., REVIEW OF SCIENTIFIC INSTRUMENTS, 78:013304, 2007.
- [113] M. Sadowski et al., Nuclear Instruments and Methods in Physics Research B 86 (1994) 311-316.
- [114] A. Malinowska et al., NUKLEONIKA 2008;53(Supplement 2):S15S19
- [115] Thomson JJ. Phil Mag 1911;21:225. 25pp.
- [116] F. Schillaci et al., Jinst 2014, doi:10.1088/1748-0221/9/10/T10003

- [117] G.A.P. Cirrone et al., proceedings of 40th European Physical Society Conference on Plasma Physics, Espoo, Finland, 1–5 July 2013, P4.207, <http://ocs.ciemat.es/EPS2013PAP/pdf/P4.207.pdf>.
- [118] M. Maggiore et al., *Nejaka Hlavicka* 123 (2010) 123.
- [119] J. Prokupek et al., *REVIEW OF SCIENTIFIC INSTRUMENTS* 85, 013302 (2014)
- [120] G. Bertuccio et al., *Appl. Surf. Sci.* 272 (2013) 128.
- [121] D. Margarone et al., *REVIEW OF SCIENTIFIC INSTRUMENTS* 83, 02B307 (2012)
- [122] F. Nava et al., *Silic, Meas. Sci. Technol.* 19 (2008) 102001 (25pp), doi:10.1088/0957-0233/19/10/102001
- [123] M. De Napoli, G. Raciti, E. Rapisarda and C. Sfienti, *Nucl. Instrum. Meth. A* 572 (2007) 831 [nucl-ex/0612018].
- [124] M. De Napoli et al., *Nucl. Instrum. Meth. A* 600 (2009) 618.
- [125] A. Re et al., *EPL*, 108 (2014) 18001 doi: 10.1209/0295-5075/108/18001
- [126] N. Randazzo et al., Nuclear Science Symposium and Medical Imaging Conference (NSS/MIC), 2012 IEEE, 10.1109/NSSMIC.2012.6551450
- [127] S. Almviva et al., *JOURNAL OF APPLIED PHYSICS* 107, 014511 2010
- [128] CIVIDEC <https://cividec.at>
- [129] <http://www.diamonddetectors.com/>
- [130] <https://www.ortec-online.com>
- [131] <http://lise.nscl.msu.edu/lise.html>

- [132] G.F. Knoll, Radiation Detection and Measurement
- [133] H.Spieler Semiconductor Detector System-Oxford Science Publications
- [134] Antonio Miotello , Roger Kelly Applied Surface Science 138-139 1999. 44-51
- [135] J. Krasa, Applied Surface Science 272 (2013) 4649
- [136] Roger KELLY and R.W. DREYFUS, Surface Science 198 (1988) 263-276
- [137] S.I. Anisimov, Soviet Phys. JETP 27 (1968) 182.
- [138] C. Cercignani, in: Rarefied Ga , Dynamics, Ed. S.S. Fisher (AIAA, New York, 1981) p. 305.
- [139] A. Lorusso, F. Belloni, D. Doria, V. Nassisi, J. Krasa, and K. Rohlena, J.Phys. D: Appl. Phys. 39, 294 (2006).
- [140] N.M. Bulgakova, A.V. Bulgakov, O.F. Bobrenok, Double layer effects in laserablation plasma plumes, Physical Review E 62 (2000) 5624–5635.
- [141] J. Krása, A. Lorusso, D. Doria, F. Belloni, V. Nassisi, K. Rohlena, Plasma Physics and Controlled Fusion 47 (2005) 1339–1349.
- [142] Margarone et al., PHYSICAL REVIEW X 6, 041030 (2016)
- [143] A. Mancic, J. Fuchs, P. Antici, S.A. Gaillard, P. Audebert Rev Sci Instrum 2008;79:073301. 6pp.
- [144] <http://www.gafchromic.com/documents/EBT3specifications.pdf>
- [145] F. Schillaci et al., March 2016, JINST doi:10.1088/1748-0221/11/07/T07005
- [146] C. Labaune, C. Baccou, V. Yahia, C. Neuville, and J. Rafelski, Scientific Reports, vol. 6, no. 1, p. , 2016.

- [147] W. M. Nevins and R. Swain, Nucl. Fusion 40, 865 (2000)
- [148] M. C. Spraker et al., Journal of Fusion Energy, vol. 31, no. 4, pp. 357-367, 2012.
- [149] D. C. Moreau, Nucl. Fusion 17, 13 (1977).
- [150] S. Stave et al., Phys. Lett. B 696, 26 (2011)
- [151] V.S. Belyaev et al 2005 Phys. Rev. E 72 026406, C. Labaune et al 2013 Nat. Commun. 4 2506
- [152] H.W. Becker, C. Rolfs, and H. P. Trautvetter, Z. Phys. A 327, 341 (1987).
- [153] V. F. Dmitriev, Phys. At. Nucl. 72, 1165 (2009).
- [154] D. -K. Yoon, J. -Y. Jung, and T. S. Suh, Applied Physics Letters, vol. 105, no. 22, p. 223507-, 2014.
- [155] D. Schardt, T. Elsässer, and D. Schulz-Ertner, Reviews of Modern Physics, vol. 82, no. 1, pp. 383-425, 2010.
- [156] C. Labaune et al 2013 Nat. Commun. 4 2506
- [157] A. Picciotto, D. Margarone, M. Crivellari, P. Bellutti, S. Colpo, L. Torrioni, J. Krasa, A. Velhyan, and J. Ullschmied, Appl. Phys. Express 4, 126401 (2011).

.. When the snows fall and the white winds blow, the lone wolf dies but the pack survives.